Studies of state-selected and spatially oriented molecules

A thesis submitted in partial fulfilment of
the requirements for the degree of

Doctor of Philosophy in Chemistry

at the University of Canterbury,
Christchurch, New Zealand.

David Alan Blunt

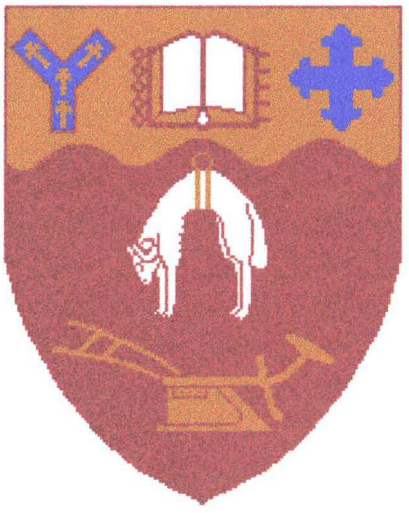

University of Canterbury
1995

Abstract

Two novel investigations of rotational quantum state-selected and of spatially oriented symmetric top molecules are reported here. In the first instance, upper Stark state relaxation cross-sections for molecular beams of CH_3Cl and for beams of 20% CCl_3H seeded in Ar are measured for a range of polar and non-polar quencher species. The variation of cross-section with quencher species is explained in terms of the strength of the long range van der Waals interaction potential between colliding species. State-specific upper Stark state relaxation cross-sections are measured for molecular beams of CH_3X (X = F, Cl and Br) species with an Ar quencher. In the case of CH_3Cl, cross-sections are also measured for N_2 as the quencher. Assignment of the cross-sections to individual $|JKM\rangle$ rotational states or a small range of $|JKM\rangle$ rotational states is facilitated by the computational simulation of hexapole filter upper Stark state transmission characteristics. In the second investigation, it is demonstrated, for the first time, that the efficiency and outcome of electron impact ionisation is influenced by molecular orientation. The ionisation efficiencies for the molecules CH_3Cl and CCl_3H are lowest for electron impact on the negative end of the dipoles. Preliminary results for CH_3Br and CF_3Br also show this orientation dependence. In addition, the mass spectrum is orientation dependent, for example, in the ionisation of CH_3Cl the ratio CH_3Cl^+:CH_3^+ depends on molecular orientation.

Acknowledgments

I would like to express heartfelt thanks to Dr. Peter Harland who has supervised me through both this Ph.D. and the Honours degree preceding it. He instils into his students a common-sense approach to science and research that aids in the ability to see around obstacles. I cannot imagine how much more difficult this research would have been without his continual support and advice.

The nature of this study demanded a large portion of time be spent designing and constructing mechanical devices. Mr. Barrie Wood of the Mechanical Workshop assisted in the design of the molecular beam machine and many of the components within. His machining skills were superb and he was always willing to demonstrate them to the author.

My colleagues, Drs. Brett Cameron and Craig Aitken and more recently Mr. Sean Harris, have been a source of ideas, advice and most importantly humour during this Ph.D. I will always remember their friendship.

I have appreciated contributions toward construction and maintenance of electrical and electronic components from Mr. Wayne MacKay and Mr. Alexander Ferguson, respectively.

I gratefully acknowledge financial support from the Chemistry Department and the University of Canterbury.

Lastly but most importantly, I thank my family for supporting me through the drought and rejoicing with me when success finally came.

Contents

List of figures

List of tables

Publications

1. Aitken, C. G., Blunt, D. A. and Harland, P. W. *J. Chem. Phys.* **101** (1994) 11074.
2. Aitken, C. G., Blunt, D. A. and Harland, P. W. *Int. J. Mass Spectrom. Ion Procs.* In press (1995).
3. Blunt, D. A. and Harland, P. W. *J. Chem. Soc. Faraday Trans.* In preparation (1995).
4. Blunt, D. A. and Harland, P. W. *J. Chem. Soc. Faraday Trans.* In preparation (1995).

Chapter 1

Introduction

The effects of molecular orientation on chemical reactivity [Harland, 1992], chemiluminescence [Ohoyama, 1993], photoionisation [Kaesdorf, 1985], Rydberg molecule formation [Kasai, 1993] and, more recently, electron scattering [Meier, 1994] have been studied. The orientation asymmetry in most systems investigated has been significant, despite the use of oriented beams characterised by a distribution of spatial orientation [Harland, 1992].

There are number of techniques available for the alignment and orientation of molecules in the gas phase. These range from facile collisional alignment in a supersonic molecular beam to electrostatic and optical state-selection methods. The orientation distributions that are prepared by many of these techniques are prone to degradation by collisions or molecular rotation prior to any asymmetry investigation. One such method of orienting molecules uses a hexapole electrostatic filter. A beam of symmetric top molecules is directed through the hexapole filter where those molecules in upper Stark states are focused onto the beam axis while those in lower states are accelerated toward the filters' rods and lost. Focused upper Stark state molecules are then exposed to a weak homogeneous electric field, providing a laboratory axis around which they orient. Orientation asymmetry effects have been found to disappear when background pressure within the hexapole filter is high [Brooks and Harland, unpublished results]. This is

interpreted as a collisional relaxation of upper Stark states leading to defocusing of these molecules from the beam. As a result, the orientation distribution within the weak homogeneous electric field and any measured asymmetry effect is degraded. Experiments reported here investigate the collisional relaxation cross-sections of upper Stark state symmetric top molecules within a hexapole device for the first time. The measurement of collisional relaxation cross-sections provides valuable information on the vacuum requirements for successful orientation asymmetry experiments.

Recent experiments involving the collision of fast potassium atoms with oriented symmetric top molecules have demonstrated that the efficiency of the initial electron transfer step in the entrance channel by the harpoon mechanism is orientation dependent [Xing, 1994]. The results beg the question, would the ionisation of a molecule by a free electron also exhibit an orientation dependence?

Elastic differential scattering cross-sections for electron impact on oriented CH_3I and CH_3Cl molecules have been measured [Volkmer, 1992; Böwering, 1994]. The deviation of cross-sections between oriented and unoriented molecules is significant. This evidence suggests that the interaction between a free electron and molecule is orientation dependent.

Experiments described here investigate the effect of molecular orientation on electron impact ionisation and fragmentation of the symmetric top molecules CH_3Cl, CCl_3H, CH_3Br and CF_3Br. Electron impact ionisation is utilised in many analytical instruments as a source of positive ions. The information gained from these experiments should be useful for interpreting fragmentation patterns in mass spectra.

This thesis is divided into four main chapters and a brief summary of the contents of each is given below. Extensive cross-referencing of information in this work necessitates the use of abbreviated chapter and section references. The symbol '§' is

used for these cross-references, for example, '§3.8.2' is a reference to chapter 3, section 8, subsection 2.

Chapter 2 provides the theoretical framework and background to the processes and components used in these experiments. A review of current methods of aligning and orienting molecules is included here with comparison to the hexapole state-selection technique.

The molecular beam machine designed and constructed for this work is detailed in Chapter 3. In the first part of this chapter the vacuum and sample handing systems are described. This is followed by a description of the components within the molecular beam machine. Computer interfacing of the experiments is outlined with the reader being directed to the Appendices for appropriate software routines.

Cross-sections for the collisional relaxation of upper Stark state symmetric top molecules within the hexapole filter are reported in Chapter 4. Results for CH_3Cl and seeded CCl_3H at fixed hexapole voltage are correlated with an attractive van der Waals interaction potential. State-specific cross-sections are determined for methyl halides CH_3X (X = F, Cl and Br) by examining the variation of relaxation cross-section with hexapole voltage. Simulation of hexapole transmission characteristics is discussed. Elastic/inelastic collision cross-sections are reported for CH_3Cl. These are a byproduct of the method used to determine relaxation cross-sections and not the object of this study. Nevertheless correlation between the elastic/inelastic collision cross-sections and appropriate van der Waals interaction potentials is obtained.

Electron impact ionisation orientation asymmetry is reported in Chapter 5 for the oriented molecules CH_3Cl, CCl_3H, CH_3Br and CF_3Br. The asymmetry effect for both molecular (where possible) and fragment ion is probed with a quadrupole mass filter. Variation of the asymmetry effect with hexapole voltage and electron energy is also

discussed. A simple Coulomb potential model is presented which qualitatively accounts for experimental observations and facilitates prediction of the possible orientation asymmetry effect for other molecules.

Chapter 2

General Principles

2.1 Introduction

The experiments reported in this thesis are performed in an ultra high vacuum apparatus, or molecular beam machine. A beam of symmetric top molecules is passed into a hexapolar electrostatic filter where those molecules in upper Stark states are focused onto the beam axis. §4 describes the collisional attenuation of upper Stark states within the filter, and an experiment that uses the focused beam to investigate the possibility of electron impact ionisation asymmetry is described in §5.

This chapter provides the theoretical background to key experimental components and processes:

- molecular beam formation;
- current methods of orienting or aligning molecules, and a comparison with the hexapole filter employed here;
- hexapole state-selection and orientation;
- collision cross-sections;
- electron impact ionisation; and
- ion detection.

The order of this chapter follows the sequence of events that occur within the molecular beam machine, from beam formation and state-selection through to collision (in the case of §4 experiments), ionisation and detection.

2.2 Molecular beams

Reagents prepared as a narrow beam of atoms or molecules travelling through an evacuated chamber form the basis of numerous physical and chemical experiments [Scoles, 1988; Anderson, 1974]. From a source, or oven, gaseous molecules are admitted into the vacuum *via* a small orifice. Two extreme cases exist, where the beam molecules either retain the properties of the source gas, ie. velocity and internal state population distributions, or are transformed (by collisions) as they exit the source so that those initial distributions are substantially altered. The distinction between *effusive* sources, where beam and source molecules have similar properties, and *supersonic* sources is described in terms of the Knudsen number

$$K_n = \frac{\lambda}{d} \qquad (2.1)$$

where λ is the mean free path between collisions in the source (proportional to particle density) and d the exit orifice diameter. For effusive sources $K_n > 1$ while $K_n < 1$ for supersonic sources. Both sources have their application in reaction dynamics and are discussed here, with emphasis on the supersonic source which is utilised for this work.

2.2.1 Effusive sources

First discovered as the result of a vacuum leak, effusive beams of atoms and molecules have been used for many decades [Scoles, 1988]. Particles leaving the source through an exit orifice are unlikely to collide with other particles (remembering that $K_n > 1$). As

a result, the velocity and the internal energy distributions of the particles remain unchanged. For a population of molecules that have exited the source, the distributions describing velocity and internal energy partitioning are very similar to those describing the source molecules.

The Maxwell-Boltzmann distribution is assumed for the velocity of source molecules

$$f_{vs}(v) = \frac{4}{\sqrt{\pi}} \frac{1}{\alpha^3} v^2 e^{-v^2/\alpha^2} \tag{2.2}$$

where $\alpha = \sqrt{2kT/m}$. Particles of higher velocity have a greater probability of exiting the source and so the velocity distribution of beam molecules is

$$f_{vb}(v) = \frac{2}{\alpha^4} v^3 e^{-v^2/\alpha^2} = \left(\frac{v}{\bar{v}}\right) f_{vs}(v) \tag{2.3}$$

where $\bar{v} = \sqrt{8kT/\pi m}$ is the mean particle velocity in the source [Scoles, 1988]. For CH_3Cl at 298 K the mean velocity is 355 m s^{-1} and the width of the distribution at half maximum is 365 m s^{-1}.

The molecular rotational state population is described by a Boltzmann distribution. The contribution of a state $|JK\rangle$ to the total population is given by the fraction

$$f_{JK} = \frac{S(I,K) e^{-W/kT_{rot}}}{\sum_{J=0}^{\infty} \sum_{K=-J}^{J} S(I,K) e^{-W/kT_{rot}}} \tag{2.4}$$

where J and K are the rotational quantum numbers for a symmetric top, S(I, K) is described in §2.4.5, and $W = BhcJ(J+1) + (A-B)hcK^2$ is the rotational energy in terms of rotational constants A and B. Again using CH_3Cl at 298 K as an example, the most probable J state is 84.

While both velocity and rotational population distributions are well characterised, the broad distributions characteristic of effusive sources are undesirable for use with the hexapole state-selection device employed here (refer to §2.4.5).

For later comparison with a supersonic source, the effusive beam flux is

$$Q = \frac{n\bar{v}A}{4} \tag{2.5}$$

where n is the source particle density, $\bar{v}$ the mean velocity and A the exit orifice area. This flux is distributed over all angles about the beam axis (a cosine distribution about any perpendicular axis) and as a function of distance, z, falls off as $1/z^2$ per unit area. For 1 atm CH_3Cl at 298 K forming an effusive beam through an exit orifice of 1 μm diameter, $Q = 7\text{x}10^{15}$ s^{-1} and the axial particle density one metre away would be 10^9 cm^{-3}.

2.2.2 Supersonic sources

The beam characteristics for a supersonic source (where $K_n < 1$) are substantially different from the effusive source. Particles entering the vacuum through the exit orifice are subject to many collisions giving rise to *hydrodynamic* flow in the exit region with a marked change in the velocity and internal energy population distributions. The process of supersonic expansion can be separated into three distinct regions. The first is the region of hydrodynamic flow through the nozzle orifice where a large number of collisions occur. Random thermal motion is rapidly converted to directed flow along the beam axis. Internal degrees of freedom are also *cooled* with a corresponding increase in directed flow velocity [Pauly and Toennies, 1968]. The term *supersonic* refers to the resulting directed flow velocity being larger than the local speed of sound, or

$$M = \frac{u}{a} > 1 \text{ (Mach number)} \qquad (2.6)$$

where u is the directed flow velocity and $a = \sqrt{\gamma kT / m}$ the local speed of sound, where $\lambda = C_p / C_v$. The second region is downstream of the nozzle orifice but close to it where the collision frequency falls off due to the decrease in random thermal motion. Conversion of internal and random kinetic energies to directed flow decreases rapidly with distance from the orifice as a result [Cameron and Harland, 1991]. Finally, there is a third region where collision frequency is approximately zero, for typical background pressure and vacuum system dimensions.

Velocity of the beam particles following expansion is well described by the function

$$f_{vb}(v) = Av^2 \, e^{-m(v-u)^2 / 2kT_{\parallel}} \qquad (2.7)$$

where u is the directed flow velocity, $T_{\parallel}$ the translational temperature and A a normalisation constant. The values of u and $T_{\parallel}$ are found by fitting the distribution to experimental data. For CH_3Cl with typical operating conditions, u = 543 m s^{-1} and $T_{\parallel}$ = 31 K (§4.3.2.2) [Cameron and Harland, 1994]. The thermodynamic limiting flow velocity, u_∞, where all internal and thermal kinetic energy is transferred to velocity along z, is calculated according to

$$u_\infty = \left(\frac{\gamma}{\gamma - 1}\right)^{1/2} \left(\frac{2kT}{m}\right)^{1/2} \qquad (2.8)$$

and reproduces experimental flow velocities of inert gases but fails for polyatomics. This is a result of using a statistical model to describe an inherently non-statistical process. Figure 2.1 illustrates the differences between effusive and supersonic velocity distributions.

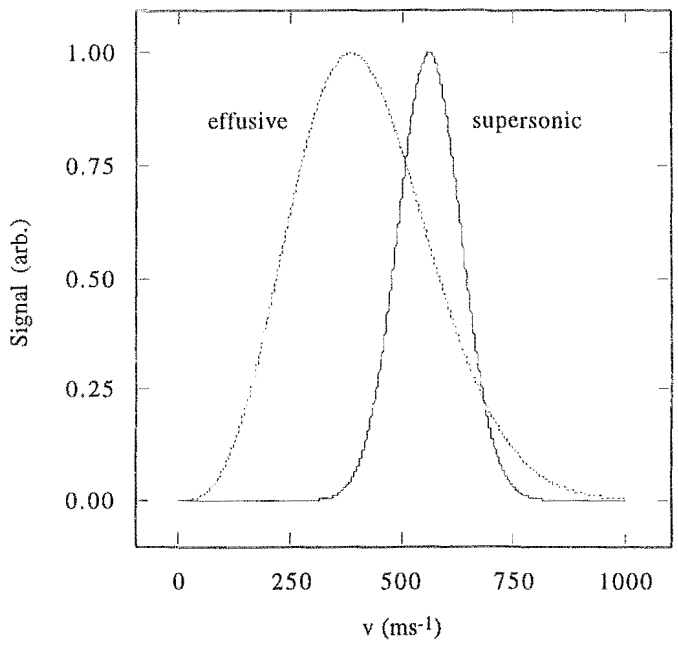

Figure 2.1 Comparison of supersonic and effusive velocity distributions.

Following the supersonic expansion rotational temperature is lowered typically to a few Kelvin due to rotational cooling that occurs in the supersonic expansion process [Cameron and Harland, 1993]. Calculation of the rotational temperature for CH_3Cl shows it to be ~10 K. The most probable J state at this temperature is 15 (eqn. 2.4).

The intensity of a supersonic beam is typically several orders of magnitude greater than that obtainable from an effusive source [Scoles, 1988]. The thermal conduction model predicts beam density to be

$$n(z) = n_o \left(\frac{z}{z_o} \right)^{-2} \tag{2.9}$$

assuming that the thermodynamic limiting flow velocity is reached, where n_o is the source particle density, z is distance from the source, and z_o is defined as

$$z_o^2 = r_o^2 K \left[\left(\frac{\gamma - 1}{\gamma + 1} \right)^{1/2} \left(\frac{2}{\gamma + 1} \right)^{1/(\gamma - 1)} \right] \tag{2.10}$$

where r_o is the source exit orifice radius and κ is the source peaking factor, a complicated function of γ [Cameron and Harland, 1993b]. For 1 atm CH_3Cl at 298 K through an orifice of 35 μm radius, particle density one metre from the source would be $3x10^{10}$ cm^{-3}.

Beam density for a particular gas and nozzle is limited by the source or stagnation pressure. An increase in this pressure requires a corresponding increase in the pumping speed around the expansion region. Much higher stagnation pressures are feasible, however, if the exit orifice is pulsed open for only a short period of time. In this work the orifice is open for 1-2 ms at a rate of 10 Hz. Gas load is reduced 50-fold as a result. Modest pumping allows source pressures of 2000 torr to be maintained with the result being a higher beam density, calculated to be $8x10^{10}$ cm^{-3} at a distance of one metre from the nozzle orifice.

Improved beam intensity over an effusive source coupled with the narrow velocity and low peaking rotational state distributions make the supersonic source an ideal beam source for the hexapole state selector used in this work.

2.3 Orientation and alignment

Experiments in §5 probe the interaction between a symmetric top molecule and an electron leading to ionisation in terms of electron approach geometry. The angle made between the incident electron and the symmetric top molecular axis is experimentally tuneable. Methods of orienting or aligning reactants and their effectiveness are the subject of this section.

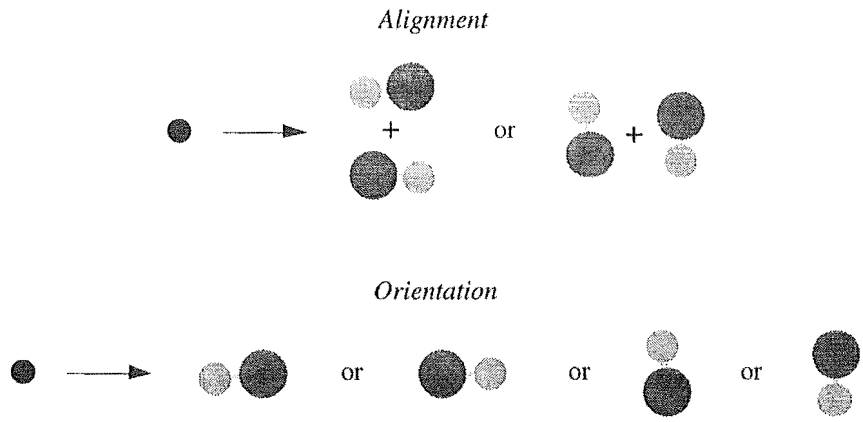

Figure 2.2 Alignment versus orientation.

The terms *orientation* and *alignment* must be defined. Consider a molecule, not necessarily a diatomic, with two distinguishable ends. An atom travelling toward a collection of these molecules which are perfectly aligned will encounter them end-on (*parallel*) or side-on (*perpendicular*), as shown in Figure 2.2. The separation of *parallel* from *antiparallel* (Figure 2.2) is the key difference between orientation and alignment.

Of course the axis around which the molecules are aligned or oriented does not have to be parallel to the incoming atom. It is commonly chosen to coincide with the system's centre-of-mass velocity vector.

Control over the alignment of molecules in liquids was studied late last century by Maxwell and in the gas phase by Senftleben in 1930 [Maxwell, 1867; Senftleben, 1930]. Since that time vacuum technology has evolved to the point where routine use of molecular beams and high strength electric fields in experimental chemistry has made possible the development of orientation and alignment methods for molecules in the gas phase. In the fifties a theoretical paper by Bennewitz, *et al.* paved the way for the use of strong inhomogeneous electric fields in alignment and orientation studies [Bennewitz, 1955]. With the development of high power lasers it has become possible

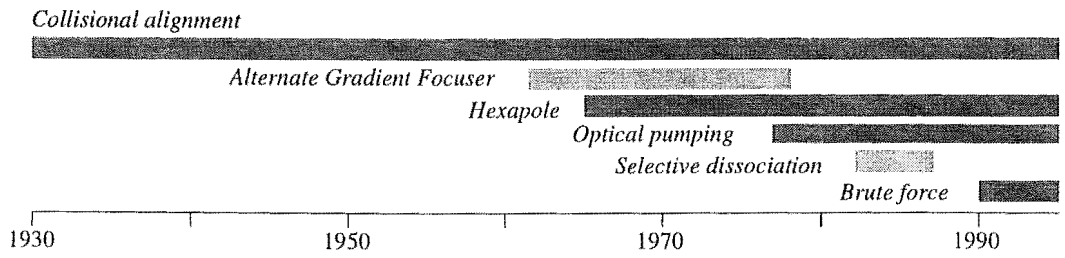

Figure 2.3 Development of alignment and orientation methods.

to probe the electronic, vibrational and rotational transitions of species in molecular beams, and this leads to the possibility of producing populations of aligned or even oriented molecules. Figure 2.3 illustrates the historical development of alignment and orientation techniques from collisional alignment to the brute force method.

The following subsections describe those methods used presently and comparison is made with the hexapole state-selection technique employed in this work. Literature examples are detailed to illustrate the effectiveness of each method.

2.3.1 Collisional alignment

Intuition suggests that an object carried along in some direction will arrange itself (if possible) in such a way as to minimise the resistance to movement in that direction. Everyday examples abound such as a canoe floating down a river or a javelin cutting through the air. Non-spherical molecules moving under flow conditions behave in a similar manner. Molecular collisions often result in an exchange of energy that leads to a change in direction, specifically, of the molecule's angular momentum vector, and this is fixed in relation to the molecule's principal axis. With this change of direction the collision *cross-section* may be altered with respect to the other entities. In light of the physical picture presented above it is obvious that a molecule under flow conditions is least perturbed when the collision cross-section is at its smallest. Further, collisions

leading to changes in this cross-section will fall off in number as the smallest value is reached. Collisional alignment then is the realignment of a molecule's principal axis by energy transfer collisions and the alignment is maintained due to non-uniformity of the molecule's collision cross-section. This phenomenon is observed for liquids and for paramagnetic gases [Maxwell, 1867; Senftleben, 1930; Beenakker, 1962]. Thermal conductivity and viscosity are found to vary as a magnetic field is applied across a flow of molecules. As the field strength is increased both bulk properties decrease to a limiting value. Molecules possessing a magnetic dipole will precess around the direction of an applied field so alignment of these molecules is disrupted by this precession. Raising the field strength increases the rate of precession to the point where the collision cross-section tends to a constant and larger value. Both thermal conductivity and viscosity depend inversely on the collision cross-section so any increase in the cross-section is observed as a decrease in those bulk properties.

To study a reaction where one reagent has been aligned ideally there must not be any interfering collisions before interaction with the other reaction species. Such a condition is easily met with today's high vacuum technology. A supersonic molecular beam is suitable for producing collisionally aligned molecules since there is a considerable velocity gradient along which molecules will flow and a large number of collisions during the expansion. Once expansion is complete the molecules travel essentially collision-free and the beam can be crossed with another containing the second reactant.

A preliminary step toward use of collisional alignment in reactive studies is the characterisation of the degree of alignment obtained in supersonic molecular beams. Sinha, *et al.* have measured this for Na_2 in a sodium beam and more recently Pullman, *et al.* have investigated alignment of I_2 molecules seeded in a range of carrier gases [Sinha, 1974; Pullman, 1990]. The paragraphs below outline the relationships between

angular momentum, principal axis and collision cross-section for a diatomic molecule along with a description of alignment mechanisms.

Consider a diatomic molecule with angular momentum vector **J**. The direction of this vector is perpendicular to the molecule's principal axis and rotation of the molecule occurs in a plane perpendicular to **J**. If this molecule travels along in a molecular beam having an axis z then we can describe two extreme orientations of the molecule with respect to this axis and they are illustrated in Figure 2.4. The collision cross-section between our diatomic and any species also travelling in the z direction will be smaller in the first case, that is when **J** lies perpendicular to the beam axis.

Diatomic molecules oriented with **J** perpendicular to z will dominate as more collisions occur. Alignment dependence on the number of collisions is termed *bulk alignment* and is enhanced by both beam pressure and slip velocity [Friedrich, 1991; Pullman, 1990]. Slip velocity is important where the diatomic is only a small fraction of the beam population. If the diatomic molecule is seeded in a light carrier gas then during the supersonic expansion there is a substantial velocity difference between seed and carrier species leading to more collisions before expansion is complete. This parameter is exploited in the seeding of iodine molecules with various carrier gases and will be discussed further.

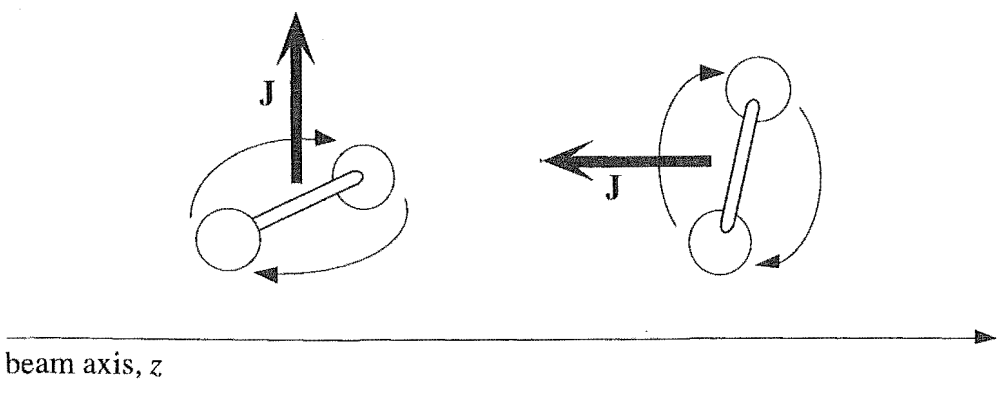

Figure 2.4 Two extreme cases of **J** alignment.

As beam pressure is increased beyond a certain point the degree of alignment decreases and in some extreme cases reverses its sense, that is, there are more molecules present with **J** parallel to the beam axis. This effect arises due to the extreme rotational cooling characteristic of supersonic expansions [Pauly and Toennies, 1968]. The cross-section for rotational relaxation is larger when **J** is perpendicular to the colliding species and so the terminal rotational temperature will be lower for these orientations. For a population of molecules, the contribution of one rotational state to the total population at a given temperature is described by a Boltzmann distribution as shown in Figure 2.5 and described by eqn. 2.4. Below some critical rotational temperature the Boltzmann weight factor for molecules with **J** perpendicular to the beam axis is much lower than those molecules whose **J** is parallel (remembering that T_r is lower for the former).

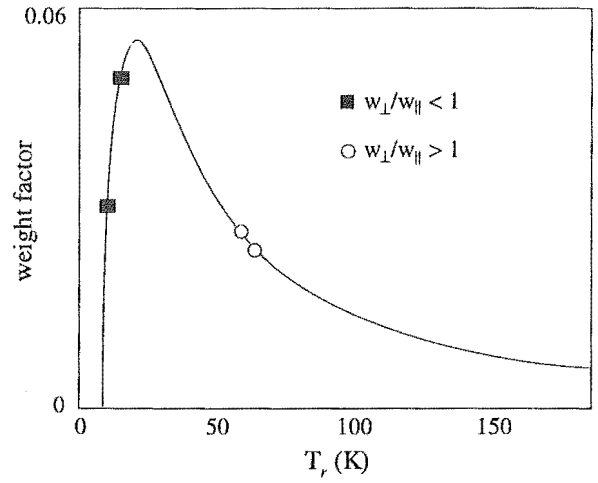

Figure 2.5 Boltzmann weight function for J=15.

In the peculiar case of alkali metal dimers a further mechanism for alignment exists [Sinha, 1974]. The rate of dimer destruction and reformation occurring during the expansion process is dependent on the torque exerted on the dimer bond.

$$M' + M_2 \rightarrow MM' + M \qquad (2.11)$$

This torque is larger when the angular momentum vector is parallel to the beam axis, ie. the reactive cross-section is larger, and following previous reasoning these orientations will be depleted as more reactive collisions occur.

2.3.1.1 Na_2 dimer alignment

A supersonic beam of sodium is expanded into high vacuum [Sinha, 1974]. The Na_2 dimer forms during the expansion and is rovibronically excited with a linearly polarised laser light. Fluorescence from the excited state is detected by two photomultipliers placed at right angles to both the molecular and laser beams. The fluorescence intensity is measured as components parallel and perpendicular to the electric field vector of the incident laser radiation, $I_{\parallel}$ and $I_{\perp}$, respectively. Polarisation of the fluorescence is then defined as

$$P = \frac{I_{\parallel} - I_{\perp}}{I_{\parallel} + I_{\perp}}. \qquad (2.12)$$

For an isotropic distribution of **J** around the molecular beam axis P will be 0.5. Experimentally this decreases linearly with the logarithm of beam pressure to 0.44 at the maximum vapour pressure obtainable. In terms of Na_2 alignment the increase in pressure causes more collisions during expansion which leads to an increase in the number of molecules with **J** perpendicular to the beam axis. The angle which the electric field vector makes with the molecular beam axis is rotated and polarisation values are repeatedly measured. Using pairs of these measurements the distribution of angular momentum about z is determined. At the maximum beam pressure this shows **J** to be preferentially aligned perpendicular to the molecular beam axis with a ratio of 3:2.

2.3.1.2 Alignment of seeded I_2

Unlike the sodium dimer, iodine may be seeded in a variety of carrier gases for use in supersonic beams. Fluorescence intensity following rovibronic excitation by linearly polarised light is measured [Pullman, 1990; Friedrich, 1991]. Instead of measuring the degree of fluorescence polarisation another technique is employed. Passing the molecular beam transversely through a magnetic field prior to the laser beam causes the magnetic moment of iodine to precess about the field through an angle, β. The magnetic moment is fixed in relation to the total angular momentum vector **F** which, to a good approximation for iodine, lies in the same direction as **J**. When the magnetic field is switched on, the average direction of the transition dipole moment relative to **E** will change with a corresponding variation in fluorescence intensity. This change can be expressed

$$\frac{I(H)-I(0)}{I(0)} = \frac{Aa_2 \sin^2 \beta}{1.0 + Ba_2} \qquad (2.13)$$

where A and B are known and dependant on the angle between **E** and z, and the distribution of angular momenta is of the form $n(\theta) = 1 + a_2 P_2(\cos\theta)$, where $P_2(\cos\theta)$ is a Legendre polynomial (described in §2.4.3).

At low backing pressures the alignment ratio increases with velocity gradient, when I_2 is seeded in H_2 an alignment ratio of up to 2.2 is obtained. For iodine-argon a peak of 1.2 is observed, consistent with the difference in velocities of H_2 and Ar. An increase in the number of collisions during expansion (by raising the backing pressure) results in increasing alignment. All of these observations can be ascribed to the bulk alignment mechanism that is described above. As backing pressure is increased even further, reducing T_r, the alignment ratio starts to drop as predicted by the *anisotropic rotational cooling* mechanism, for neon this can become less than one, ie. **J** preferentially directed parallel to the beam axis.

There are several important conclusions to be drawn from the above discussion and examples:

- All non-spherical molecules suitable for use in supersonic beams could be collisionally aligned to some degree.
- The alignment process is statistical and state-selective in only the broadest sense.
- Calculation of the alignment ratio is not possible at present and expensive experimental techniques tailored to each molecule must be employed.

2.3.3 Optical methods

Passing light from an incandescent bulb through polaroid sheet filters out some but not all of the incident light. Rotation of a second polaroid sheet positioned in the transmitted light results in a modulation of the intensity from close to 100% to close to 0%. These two observations demonstrate that photons have a directional property and that this property can be used to separate a collection of photons. Of course, this property is the photon's electric vector. With the advent of laser devices preparation of intense beams of linearly polarised photons (in reference to the electric vector direction) is straightforward. Rotating the plane of polarisation provides a means for controlling the polarisation direction with respect to some laboratory axis, eg. a molecular beam or the relative velocity vector of two interacting species.

Excitation of molecules or atoms by absorption of light is well understood. The probability of excitation occurring is proportional to the angle with which the photon's electric vector makes with the transition dipole moment of interest. This transition dipole moment is fixed with respect to the species' principal axis. This will be

explained further but the important conclusion to be drawn is that preparation of aligned excited molecules is possible.

Two different approaches to the alignment of molecules with laser light have been exploited. Where the excited species is reacted then the method of alignment is termed *optical pumping* while for ground state species the method is termed *selective dissociation* [Drullinger and Zare, 1969]. Only optical pumping is considered here though both methods are conceptually and experimentally similar. Of key importance to the use of optical methods in orientation studies is an understanding of the alignment distribution and how it evolves over time. Collisions and the molecules' own rotation smear out the initial alignment distribution and because of this experimental configurations are designed to minimise the time delay between excitation and reaction [Drullinger and Zare, 1973].

For a molecule with transition dipole moment, μ, and a photon with electric field vector, $\mathbf{E}$, the probability of excitation occurring is proportional to the vector product $\mathbf{E}\mu$.

$$P \propto |\mu|^2 |\mathbf{E}|^2 \cos^2 \theta \qquad (2.14)$$

where θ is the angle between the transition dipole moment and light vector $\mathbf{E}$. This fact is exploited in the characterisation of collisional alignment described previously. At this point it should be noted that μ is defined to point toward the positive end of the transition dipole while $\mathbf{E}$ points in the negative field direction. Figure 2.6a depicts a molecule whose transition dipole moment lies parallel to its internuclear axis. In Figure 2.6b the molecules travel along in the molecular beam direction, z, and interact with linearly polarised photons. The excitation that occurs produces an anisotropy in the spatial distribution of the excited molecules. In the present example excited species will rotate in a plane parallel with the beam axis, z. An atom (or molecule) which is known to react with the excited state intersects the molecular beam in Figure 2.6c. The

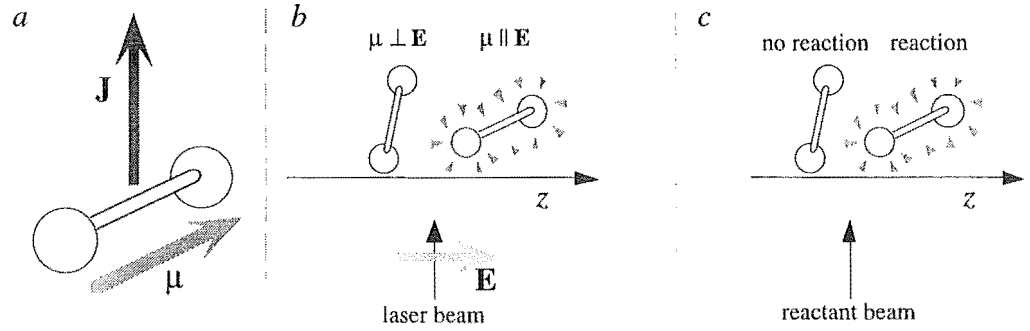

Figure 2.6 Laser alignment.

atom (or molecule) approaches its reaction partner in a *broadside* manner. By rotating the direction of **E** relative to the beam axis this approach geometry may be varied between *broadside* and *end-on*.

After laser excitation the molecule continues to rotate and this *smears out* any alignment, however if careful attention is paid to experiment design the degree of alignment remains significant.

2.3.3.1 Reaction of I_2^* with Tl and In

An effusive molecular beam of Tl or In is passed into a chamber containing I_2 vapour [Estler and Zare, 1978]. The I_2 is excited at a point along the molecular beam by linearly polarised light to $v' = 43$, $J' = 12,16$ of the $B^3\Pi$ state. Reaction proceeds in the following manner:

$$I_2^* + M \rightarrow MI^* + I \quad M = Tl, In \tag{2.15}$$

Chemiluminescence intensity of the relaxing MI^* is measured as a function of the angle between **E** and z, defined previously in this discussion. Alignment is calculated as

$$A = \frac{I_0 - I_{90}}{I_0 + I_{90}} \tag{2.16}$$

where I_0 is the intensity for **E** parallel to z. For both metals A is found to be 0.13 ± 0.02. This corresponds to a ratio of 1.3:1 in favour of *collinear* reaction since the transition dipole moment lies parallel with the internuclear axis of I_2.

2.3.3.2 Reaction of HF* with Sr, K and Li

Several alignment studies have been carried out using HF. Firstly, after determining the thermodynamics of ground and excited state HF reactivity with Ba, Ca and Sr, Karny, *et al.* examined the reaction [Karny, 1978]:

$$HF^*(v'=1,J') + Sr \rightarrow SrF(v'',J'') + H \qquad (2.17)$$

A similar experimental arrangement to the I_2^* + M study is used. Vibrational excitation of the product is probed by laser-induced fluorescence techniques. Initial results suggested increased product vibrational excitation for a *broadside* approach geometry. However, subsequent publications revealed the observation to be an artefact [Altkorn and Zare, 1985]. The nuclear spins of H and F couple to the rotational angular momentum of the molecule and cause a depolarisation of the anisotropic distribution. As a consequence, validity of the results for reaction with potassium atoms investigated by Hoffmeister, *et al.* must also be called into question [Hoffmeister, 1987].

The reaction of Sr and Li with excited HF has been investigated by Loesch, *et al.* using a different experimental arrangement [Loesch and Stienkemeier, 1994 and 1993b]. Supersonic beams of metal and HF are intersected in a region of high electric field strength. The uniform electric field provides a quantisation axis for HF rotational angular momentum, and is a step toward the technique of brute force orientation discussed in §2.3.4. *End-on* or *side-on* attack of the metal atom is selected by varying the field direction. In the HF* + Sr experiment internal vibrational state population of

SrF is measured by laser-induced fluorescence. Population of the vibrational levels 0-3 is found to be dependent on the initial angle of attack. As translational energy is increased the steric effect disappears. Magnitude of the effect is a 10% difference in fluorescence intensity. In the case of HF^* + Li differential reaction cross-sections are measured. Angular distributions, the internal partitioning of available energy and the total reaction cross-sections for product LiF are found to vary markedly with approach geometry. A ratio of 1.76 in favour of *broadside* collision for the total reaction cross-section is observed. Product is backward scattered for all three approach geometries consistent with small impact parameters and it is shown that the steric effect will only be evident for these close range interactions.

In summary, the optical pumping of molecules to investigate reactive asymmetry is elegant yet restricted. Individual states may be populated but the process by which this is achieved is inefficient. Saturated pumping techniques to increase the efficiency of alignment are available but expensive. The method is limited to molecules with known and suitable spectroscopic properties, to date only Na_2 dimer, I_2, CS_2, HF and IBr have been studied. However, providing a Stark field to maintain the alignment distribution seems likely to allow further investigation of reactive asymmetry by this technique.

2.3.4 Brute force

Exerting a force sufficient to orient the dipole of a freely rotating molecule has been considered impractical [Brooks, 1976]. Until the use of supersonic beam technology this may have been the case yet the rotationally relaxed molecules produced in a supersonic expansion have now been oriented by a homogeneous electric field [Loesch and Remscheid, 1990 and 1991]. Free rotation of molecules in a strong electric field may be restricted especially if they are in low lying rotational states. As the dipole μ of a linear molecule rotates past $\mathbf{E}$ a torque is exerted which slows rotation down and may eventually reverse its direction. Swinging back past $\mathbf{E}$ again another turning point

results. These molecules are described as existing in *pendular* states. The technique is not limited to linear molecules but is applicable to all species with permanent electric dipole moments [Friedrich, 1991]. Success of the brute force method is dependent on the degree to which the dipole-electric field interaction can overcome the rotational energy of the molecule [Friedrich, 1991b]. Those molecules which are constrained by the field to librate between two angular limits are termed as *bound* pendular states. Ideally the limits of libration would restrict the dipole to the negative energy region, ie. with the positive end of the dipole directed toward the negative field, however this is not necessarily the case. For weakly bound states the dipole will enter the repulsive region of the field. When the plane of the rotating dipole lies close to the field direction the dipole speeds up as it swings through the attractive region of the field and slows down as it approaches the repulsive region. On average the dipole spends more time in the repulsive region and therefore points the *wrong* way. Unbound pendular states are also subject to this argument. Since the technique is statistical in nature, it is critical to have efficiently cooled molecules and high field strengths.

2.3.4.1 Reaction of K with CH_3I

Steric asymmetry of the reaction

$$K + CH_3I \rightarrow KI + CH_3 \qquad (2.18)$$

has been studied at length by many researchers [Marcelin and Brooks, 1975]. It is therefore an ideal reaction to evaluate the effectiveness of the brute force method.

Both reactants are seeded into supersonic expansions allowing the experiment to be performed at two different translational energies, 0.79 and 1.24 eV. Surrounding the collision region is a set of four plates biased in a quadrupolar sense to give a homogeneous electric field of up to 32 kV cm^{-1} [Loesch and Remscheid, 1991]. This

electrode assembly is rotated manually to make an angle β_L between the alkali beam axis and E. Scattered K and KI are detected by an electron multiplier in conjunction with a hot Re ribbon at an angle Θ to the alkali beam axis. A *steric effect* defined as

$$S(\Theta, E, \beta_L) = \frac{I_{LAB}(\Theta, \beta_L) - I_{LAB}(\Theta, \beta_L + 180°)}{I_{LAB}(\Theta, \beta_L) + I_{LAB}(\Theta, \beta_L + 180°)} \qquad (2.19)$$

is determined by reversing the plate polarity. Angle β_L corresponds to a *head-on* (I-end) approach by K whereas $\beta_L + 180°$ is predominantly tails-on (CH_3-end). The estimated extent of orientation is a 2% excess of dipoles pointing parallel with the field (as opposed to antiparallel).

Angles at which product flux is attributed to backward scattering give rise to a positive steric effect consistent with previous results in which the alkali metal approaches the iodine-end of CH_3I. At shallow angles where forward scattering is dominant a negative steric effect is observed which differs from the other studies where the steric effect remains positive at all scattering angles [Parker, 1981].

Interpretation of these results follows arguments found in other studies where forward scattering results from grazing trajectories while backward scattering occurs for smaller impact parameters. The negative steric factor observed at forward scattering angles suggests grazing trajectories must lead more favourably to product formation if the approach of K is toward the CH_3-end rather than the I-end of methyl iodide. Backward scattering is dominant when K approaches the iodine-end of CH_3I and the observed intensity is larger than that for forward scattering consistent with the calculated reaction cross section for each process.

2.3.4.2 Reaction of K with ICl

More recently the reaction

$$K + ICl \rightarrow KI + Cl,\ KCl + I \qquad (2.20)$$

was studied as a function of ICl orientation. Similar experimental conditions to the $K + CH_3I$ study allowed the use of two translational energies, 1.64 and 3.03 eV [Loesch and Möller, 1992 and 1993]. At both energies forward scattering is observed and KCl formation is favoured (4:1 at 1.64 eV and 10:1 at 3.03 eV). Fast and slow velocity components are observed for KCl and KI fluxes. A negative steric effect (as defined in the $K + CH_3I$ experiment, eqn. 2.19) is found for the fast component of KCl and a positive effect for the slow component of KI. These findings are entirely consistent with the Harpoon mechanism (described in §1) and a sudden explosion of the molecular ion. Potassium atoms approaching the I-end favour formation of fast KCl and vice versa for KI.

The brute force method is simple and inexpensive. Provided the condition of efficient rotational cooling is met, a large number of species may be oriented in this way. Experimental determination of the orientation distribution is possible through the use of laser-induced fluorescence techniques. The technique is not state-selecting and is most likely limited to the investigation of neutral-neutral interactions.

2.4 Hexapole state-selection and orientation

2.4.1 Stark effect

An electric dipole placed in an external electric field has potential energy

$$W = -\mu\mathbf{E} = -\mu\varepsilon\cos\theta \qquad (2.21)$$

where μ is the electric dipole vector, $\mathbf{E}$ is the electric field vector, and θ the angle between them [Goldstein, 1950]. This energy is termed the Stark energy and is at a minimum when the dipole is oriented parallel to the field. If not for rotation, a polar molecule might be expected to reorient its dipole moment parallel to the field. The method of brute force orientation in which this occurs to some extent is described in §2.3.4 but the general features should be summarised again here.

Consider a polar diatomic rotating in an external field. Because the dipole moment lies in the plane of rotation, the average moment is zero to a first-order approximation. However, to a second-order, that is when a torque is exerted on the angular momentum vector by the field, a dipole may be induced. Two extreme cases of rotation exist. Where the molecules angular momentum vector is perpendicular to the field direction, the field causes the molecule to rotate faster when the dipole is aligned with the field and slower when aligned against it. On average the dipole spends more time aligned against the field and the Stark energy is positive (an *upper* Stark state). The second case to be considered is where the angular momentum vector lies parallel or antiparallel to the field. In this case the dipole *droops* toward the field direction and on average $\theta < 90°$ so that the molecule has a negative Stark energy (a *lower* Stark state). As noted previously use of the second-order Stark effect requires a strong electric field to overcome the rotational force of the molecule.

The first-order Stark effect is significant, however, for a certain class of molecules. Unlike polar diatomic molecules the rotational angular momentum vector of *symmetric top* molecules does not always lie perpendicular to the dipole moment. In these cases there is a component of the dipole moment lying parallel to the angular momentum vector and this is not averaged to zero with rotation. Each molecule possessing a non-zero average dipole moment may be oriented in the field while still rotating. Placed in an inhomogeneous electric field, that is where the field strength is variable, a force is exerted on the dipole causing the molecule to move to where its energy is lower

$$\mathbf{F} = -\nabla W = -\frac{\partial W}{\partial \varepsilon}\nabla\varepsilon = \mu_{eff}\nabla\varepsilon \qquad (2.22)$$

where ∇ is the force gradient vector and μ_{eff} the effective dipole moment which depends on the Stark energy and in turn on the average dipole orientation in the field [Bennewitz, 1955]. Molecules with different orientations are subject to different forces and follow different trajectories in the field. Separation of these trajectories is the basis for hexapole state-selection and will be discussed further. For now, the motion of symmetric top molecules is considered. An expression for the Stark energy in terms of the appropriate rotational parameters is derived.

2.4.2 Symmetric top rotation (classical)

The classical rotational kinetic energy of a rigid rotor is given by

$$T = \frac{P_a^2}{2I_a} + \frac{P_b^2}{2I_b} + \frac{P_c^2}{2I_c}, \qquad (2.23)$$

where a, b and c refer to the principle axes of inertia, I_i is the moment of inertia about axis i and P_i is the angular momentum component along axis i [Atkins, 1994]. By convention the axes are chosen so that $I_a \leq I_b \leq I_c$. For symmetric tops, two of these moments are equal and the third, lying about the molecules symmetry axis is unique.

Obviously there are two classes of top, distinguished by the relative size of the moments of inertia:

- *prolate*, eg. CH_3I, where $I_a < I_b = I_c$. and a is the symmetry axis; and
- *oblate*, eg. CHI_3, where $I_a = I_b < I_c$. and c is the symmetry axis.

The following discussion continues assuming prolate symmetry. With appropriate changes in symmetry axis notation the oblate results are shown to be identical.

Rotational kinetic energy for a prolate top is then

$$T = \frac{P^2}{2I_b} + P_a^2\left[\frac{1}{2I_a} - \frac{1}{2I_b}\right] \tag{2.24}$$

where $P = \sqrt{P_a^2 + P_b^2 + P_c^2}$ is the magnitude of the total angular momentum.

When placed in an external electric field a space fixed coordinate system may be defined. The field direction is the z-axis and the molecules orientation with respect to z is specified by Euler's angles, θ, ϕ and χ [Goldstein, 1950]. Figure 2.7 illustrates the coordinate system. θ is the angle made between z and the molecular symmetry axis a (and hence between μ and $\mathbf{E}$), ϕ is the azimuthal angle about z, and χ is the angle of the molecules revolution about a.

Energy and momentum are conserved so the following expression holds

$$E = T + W = \frac{I_a}{2}(\dot{\chi} + \dot{\phi}\cos\theta)^2 + \frac{I_b}{2}(\dot{\theta}^2 + \dot{\phi}^2\sin^2\theta) - \mu\varepsilon\cos\theta. \tag{2.25}$$

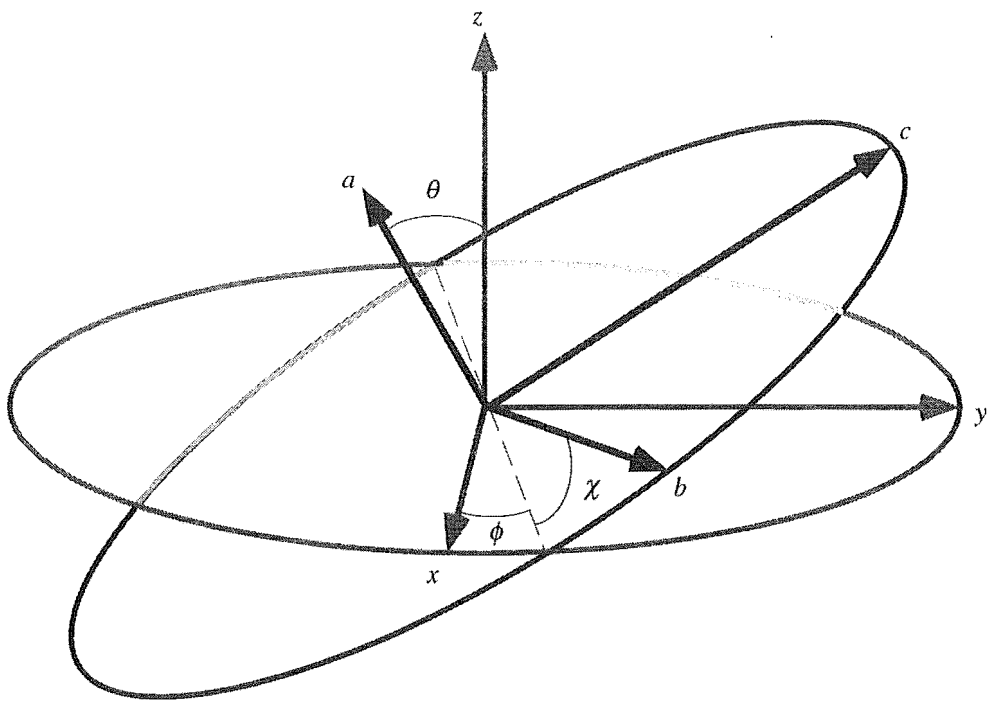

Figure 2.7 Space-fixed coordinate system.

The Eulerian angles χ and ϕ are cyclic and therefore do not appear explicitly in the above. To solve the equations of motion, the Lagrangian is defined

$$L = T - W = \frac{I_a}{2}(\dot{\chi} + \dot{\phi}\cos\theta)^2 + \frac{I_b}{2}(\dot{\theta}^2 + \dot{\phi}^2\sin^2\theta) + \mu\varepsilon\cos\theta. \quad (2.26)$$

While beyond the scope of this dissertation, solving of the equations of motion yields several important facts, illustrated in Figure 2.8 and summarised here:

- P_z, the component of angular momentum along the field direction is constant, given by $P_z = \mathbf{P}\cos\alpha$ where α is the angle between **P** and **E**.
- P_a, the component of angular momentum along symmetry axis a is also constant, given by $P_a = \mathbf{P}\cos\beta$ where β is the angle between **P** and μ.

- P_a precesses about **P**. Since μ lies along P_a, θ changes with time between two limits $\theta_1 = \alpha - \beta$ and $\theta_2 = \alpha + \beta$.
- the field exerts a torque on the dipole, causing μ and therefore **P** to precess about the field direction [Zare, 1988].

In order to determine the average value of angle θ a quantum mechanical approach to the rotating top follows.

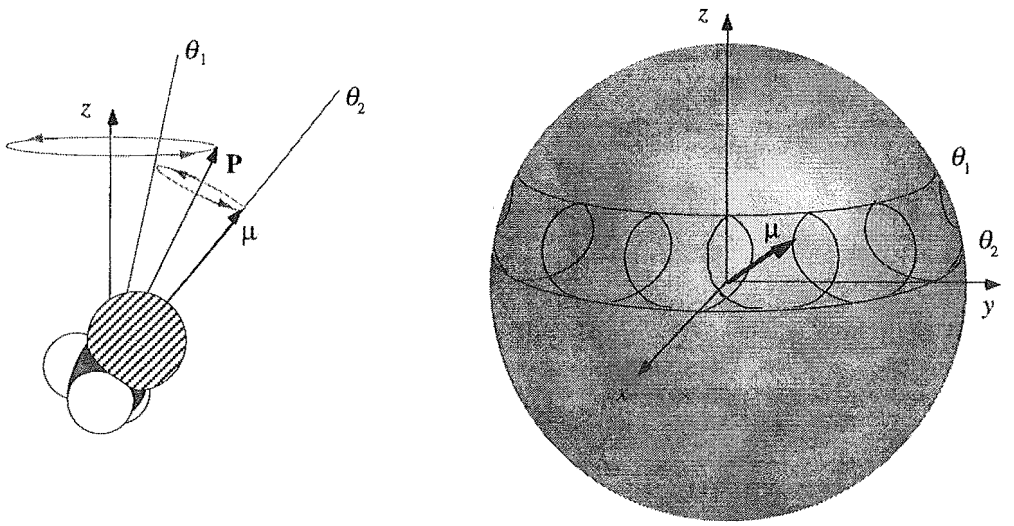

Figure 2.8 Classical precession of a symmetric top molecule.

2.4.3 Symmetric top rotation (quantum mechanical)

Solving the Schrödinger wave equation starts with defining the Hamiltonian

$$\hat{H} = \frac{-\hbar^2}{2I_b}\left[\frac{1}{\sin\theta}\frac{\partial}{\partial\theta}\left(\sin\theta\frac{\partial}{\partial\theta}\right)+\frac{1}{\sin^2\theta}\frac{\partial^2}{\partial\phi^2} + \left(\frac{\cos^2\theta}{\sin^2\theta}+\frac{I_b}{I_a}\right)\frac{\partial^2}{\partial\chi^2}-\frac{2\cos\theta}{\sin^2\theta}\frac{\partial^2}{\partial\chi\partial\phi}\right]-\mu\varepsilon\cos\theta \qquad (2.27)$$

where the same Eulerian coordinate system described in §2.4.2 is used [Townes and Schawlow, 1955]. The Hamiltonian is derived from the classical Lagrangian to which the principle of operator correspondence is applied. The wave equation $\hat{H}\Psi = W\Psi$ is then solved by a separation of variables and solutions are of the form

$$\Psi = \Theta(\theta)\mathrm{e}^{iM\phi}\mathrm{e}^{iK\chi} \tag{2.28}$$

where M and K are integers 0, ±1, ±2, ... so that the wave function Ψ remains single valued [Townes and Schawlow, 1955].

An equation for $\Theta(\theta)$ in the case of no external field is found from solutions of the hypergeometric equation [Shirley, 1963]. These solutions are a terminating power series requiring that the eigenvalues be

$$W_o = B\mathrm{J}(\mathrm{J}+1)+(A-B)\mathrm{K}^2 \tag{2.29}$$

with J a positive integer greater than or equal to |K| and |M|, and A and B the rotational constants, $A = \hbar^2 / 2I_a$ and $B = \hbar^2 / 2I_b$. Comparison with eqn. 2.24 shows $\hbar^2\mathrm{J}(\mathrm{J}+1)$ to be equivalent to total angular momentum **P** squared, and $\hbar^2\mathrm{K}$ the projection of **P** onto the symmetry axis a. $\hbar^2\mathrm{M}$ is shown to be the projection of **P** along the electric field direction [Townes and Schawlow, 1955]. In the absence of a field M states and ±K states are degenerate.

With the zero-field wave functions as a basis, the wave equation with an external field Hamiltonian term may be solved. The Hamiltonian is represented by an infinite matrix with elements in Dirac notation

$$\left\langle \mathrm{J'\ K'\ M'}\left|\hat{H}\right|\mathrm{JKM}\right\rangle = \frac{\hbar^2}{2I_b}W_o\delta_{\mathrm{JJ'}}\delta_{\mathrm{KK'}}\delta_{\mathrm{MM'}} - \mu\varepsilon\left\langle \mathrm{J'\ K'\ M'}\left|\cos\theta\right|\mathrm{JKM}\right\rangle . \tag{2.30}$$

Eigenvalues for this matrix give the possible Stark energies of the molecule [Shirley, 1963]. Calculation of the energies is slow and an approximation is made in the case of a weak field, where the Stark energy is a small correction to the total energy ($\mu\varepsilon/hB << 1$). Solutions for a weak field are then found using perturbation theory [Townes and Schawlow, 1955].

The first-order Stark energy is found by averaging the field perturbation over the appropriate field-free wavefunctions.

$$W_1 = -\varepsilon \int \Psi^* (\mu \cos\theta) \Psi d\tau. \qquad (2.31)$$

Evaluating the integral gives

$$W_1 = -\mu\varepsilon \frac{MK}{J(J+1)} = -\mu\varepsilon < \cos\theta >= -\mu_{eff}\varepsilon, \qquad (2.32)$$

where $<\cos\theta>$ is the average value of $\cos\theta$ [Townes and Schawlow, 1955].

Comparing W_1 with the zero-field energy, it is obvious that the M and ±K state degeneracies no longer exist. States with MK<0 increase in energy with increasing field strength while for states with MK>0 the opposite is true. The next section describes the hexapole field and calculation of the gradient field vector necessary to determine the trajectories of symmetric top molecules in rotational states $|JKM\rangle$.

However, a comparison of the classical and quantum mechanical limits placed on θ for a given rotational state $|JKM\rangle$ should be made. Recall that $\theta_1 = \alpha - \beta$ and $\theta_2 = \alpha + \beta$ are the classical limits for θ where α is the angle between **P** and **E** and β is the angle between **P** and the symmetry axis a. For state $|111\rangle$ the limiting values for θ are 0° and 90°. Outside these limits, the probability is undefined. Quantum mechanically it has been shown that there is finite probability of a given $|JKM\rangle$ state being oriented with an

angle θ anywhere between 0° and 180° [Choi and Bernstein, 1986]. The probability distribution is given by

$$P_{\mathrm{JKM}}(\rho) = \frac{(2\mathrm{J}+1)}{2} \sum_{n=0}^{2\mathrm{J}} C_n(\mathrm{JKM}) P_n(\rho), \tag{2.33}$$

where $\rho \equiv \cos\theta$, C_n(JKM) are tabulated expansion coefficients and $P_n(\rho)$ are Legendre polynomials.

Calculation of orientation distributions is important in the analysis of any asymmetry experiment and as a result will be explored in §5. The reader should refer also to discussion of transmission probability and orientation distributions in §2.4.5 and §2.4.6 respectively.

2.4.4 Hexapolar inhomogeneous electric field

In general the electric field potential U for $2n$-fold hyperbolic electrodes can be written

$$U_n(r,\phi) = U_o \left(\frac{r}{r_o}\right)^n \cos n\phi, \text{ or} \tag{2.34}$$

$$U(r,\phi) = U_o \left(\frac{r}{r_o}\right)^3 \cos 3\phi \text{ for the } 2n = 6 \text{ case,} \tag{2.35}$$

where r, ϕ and r_o are given in Figure 2.9 and U_o is the electrode potential. In practice, due to the difficulty of machining hyperbolic surfaces, electrodes or rods of circular cross-section are used. The approximation is good provided the rod curvature at r_o is identical to the equivalent hyperbolic electrode.

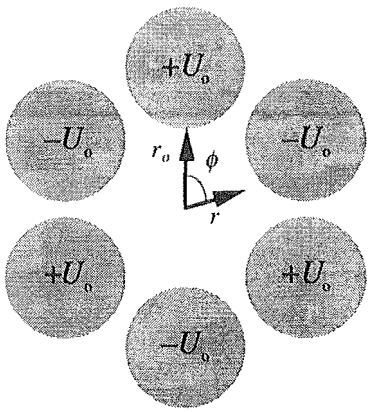

Figure 2.9 Hexapole transverse cross-section.

The electric field vector is given by

$$\mathbf{E} = -\nabla U(r, \phi), \tag{2.36}$$

where the gradient vector is the sum of unit vector partial derivatives

$$\nabla = \frac{\partial}{\partial r}\mathbf{e}_r + \frac{\partial}{\partial \phi}\mathbf{e}_\phi + \frac{\partial}{\partial z}\mathbf{e}_z. \tag{2.37}$$

Away from the ends of the electrode assembly the field vector is

$$\mathbf{E} = 3U_o\left(\frac{r^2}{r_o^3}\right)\cos(3\phi)\mathbf{e}_r - 3U_o\left(\frac{r^2}{r_o^3}\right)\sin(3\phi)\mathbf{e}_\phi \tag{2.38}$$

and electric field strength

$$\varepsilon = (\mathbf{E}\cdot\mathbf{E})^{1/2} = 3U_o\frac{r^2}{r_o^3}. \tag{2.39}$$

Referring back to eqn. 2.22 and subsequent derivations, the force exerted by the field on the dipole is given by

$$\begin{aligned}\mathbf{F} = -\nabla W &= -\frac{\partial W}{\partial \varepsilon}\nabla\varepsilon = \mu_{eff}\frac{\partial \varepsilon}{\partial r} \\ &= \frac{6U_o\mu_{eff}}{r_o^3}r\end{aligned} \tag{2.40}$$

and substituting eqn. 2.32 the radial force is

$$\mathbf{F}_r = \frac{6U_o\mu}{r_o^3}\frac{\mathrm{MK}}{\mathrm{J(J+1)}}r = m\ddot{r} \tag{2.41}$$

where it is assumed that molecules enter the field on axis so that the centrifugal component of the radial force is zero. Expressing the radial force as

$$\ddot{r} = \frac{6U_o\mu}{mr_o^3}\frac{\mathrm{MK}}{\mathrm{J(J+1)}}r = \omega^2 r \tag{2.42}$$

where

$$\omega^2 = \frac{6U_o\mu}{mr_o^3}\frac{\mathrm{MK}}{\mathrm{J(J+1)}}, \tag{2.42a}$$

three types of trajectories may be described:

- MK > 0, where solution for r is $r(t) = A\mathrm{e}^{\omega t} + B\mathrm{e}^{-\omega t}$ leading to divergence from the field axis;
- MK < 0, where solution for r is $r(t) = A\cos(\omega t) + B\sin(\omega t)$ leading to sinusoidal motion about the field axis; and
- MK = 0, where no force is exerted.

2.4.5 Hexapole transmission of $|JKM\rangle$ states

The following discussion applies to states where $MK < 0$. Molecules entering the hexapole with $MK > 0$ diverge rapidly from the axis and are lost, and normally a beam stop is placed on axis to remove $MK = 0$ states that cannot be deflected. The beam stop is described in §3 and §4.

Transmission of an individual symmetric top molecule in rotational state $|JKM\rangle$ with velocity v is contingent on three conditions. These conditions are defined in terms of the hexapole geometry, collimating apertures and beam stop illustrated in Figure 2.10.

1 the molecule must pass into the hexapole field;

2 the molecule must remain within a distance r_o of the field axis z ; and

3 the molecule must leave the field through an exit aperture of radius, r_{ex}.

Each condition is derived below, however at this point it is worth noting that total upper Stark state transmission through the hexapole is found by integrating over a *distribution* of velocities and rotational states.

The equations of motion are given again as

$$r(t) = A\cos(\omega t) + B\sin(\omega t). \tag{2.43}$$

It is assumed for the following derivations that the nozzle is a point source. A is found at $t = 0$ to be the radial distance $d_1 \tan\alpha \approx d_1\alpha$ since $\alpha << 1$. Finding $\dot{r}(t)$ identifies B as $\frac{v}{\omega}\sin\alpha \approx \frac{v\alpha}{\omega}$ since $\alpha << 1$. The explicit equation of motion is then

$$r(t) = d_1\alpha\cos(\omega t) + \frac{v\alpha}{\omega}\sin(\omega t). \tag{2.44}$$

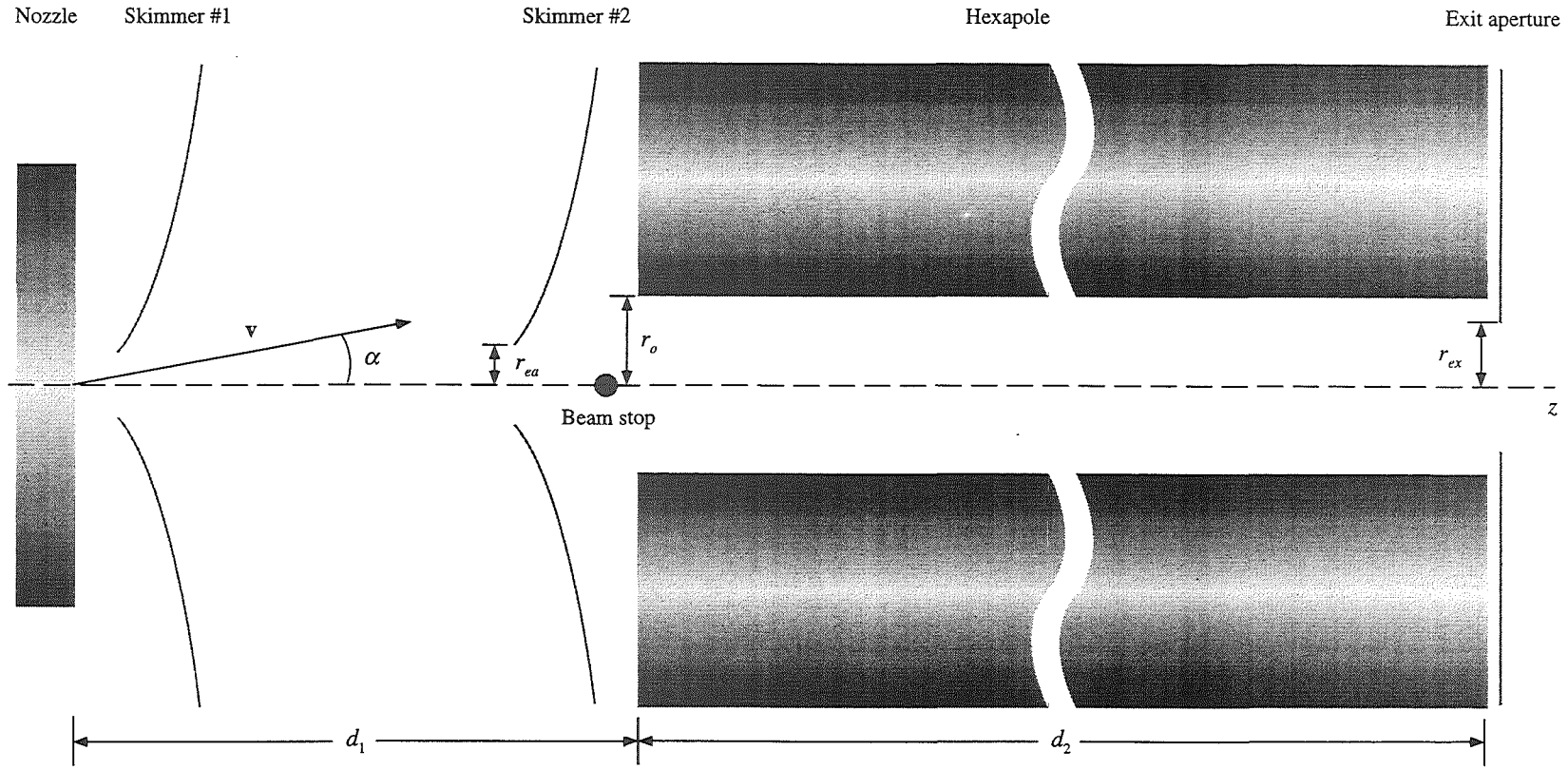

Figure 2.10 Hexapole transmission geometry (scale distorted).

2.4.5.1 Transmission entrance condition

The angle α made between the molecules velocity vector and the hexapole axis must lie between the angles made by the beam stop, α_{bs}, and the entrance aperture, α_{ea} (in this case skimmer #2).

$$\alpha_{bs} < \alpha < \alpha_{ea}. \tag{2.45}$$

2.4.5.2 Transmission field condition

The maximum radial displacement, r_{max}, from the hexapole axis must be less than r_o. r_{max} is achieved when

$$\dot{r}(t_{max}) = -\omega d_1 \alpha \sin(\omega t_{max}) + v\alpha \cos(\omega t_{max}) = 0 \tag{2.46}$$

$$\frac{v}{\omega d_1} = \frac{\sin(\omega t_{max})}{\cos(\omega t_{max})} = \tan(\omega t_{max})$$

$$\omega t_{max} = \tan^{-1}\left(\frac{v}{\omega d_1}\right). \tag{2.47}$$

Hence r_{max} is found

$$\begin{aligned} r_{max} &= d_1 \alpha \cos(\omega t_{max}) + \frac{v\alpha}{\omega}\sin(\omega t_{max}) \qquad (2.48)\\ &= d_1 \alpha \left(\frac{\omega d_1}{\sqrt{v^2 + \omega^2 d_1^2}}\right) + \frac{v\alpha}{\omega}\left(\frac{v}{\sqrt{v^2 + \omega^2 d_1^2}}\right) \\ &= \frac{d_1^2 \alpha \omega^2 + v^2 \alpha}{\omega\sqrt{v^2 + \omega^2 d_1^2}} \\ &= \frac{v\alpha}{\omega}\sqrt{1 + \frac{\omega^2 d_1^2}{v^2}} \\ r_{max} &= \frac{v\alpha}{\omega}\sqrt{1 + \beta_1^2} \qquad (2.49) \end{aligned}$$

where $\beta_1 = \frac{\omega d_1}{v}$. For transmission $r_{max} < r_o$ so

$$\frac{v\alpha}{\omega}\sqrt{1+\beta_1^2} < r_o$$

$$\alpha_{tr}^2 < \frac{r_o^2\omega^2}{v^2(1+\beta_1^2)}. \qquad (2.50)$$

2.4.5.3 Transmission exit condition

The radial displacement of a molecule must be less than the exit aperture radius, r_{ex}. Since the molecule reaches the aperture at time, $t_{ex} = d_2 / v$, α is found

$$r(t_{ex}) = d_1\alpha\cos\left(\frac{\omega d_2}{v}\right) + \frac{v\alpha}{\omega}\sin\left(\frac{\omega d_2}{v}\right) < r_{ex} \qquad (2.51)$$

$$\cos\beta_2 + \frac{1}{\beta_1}\sin\beta_2 < \frac{r_{ex}}{d_1\alpha}$$

where $\beta_2 = \frac{\omega d_2}{v}$. Multiplying by β_1 and squaring gives

$$\alpha_{ex}^2 < \frac{r_{ex}^2\omega^2}{v^2\left(\beta_1\cos\beta_2 + \sin\beta_2\right)^2}. \qquad (2.52)$$

To summarise, the angle of incidence α must be greater than α_{bs} and less than α_{ea}. Also, α^2 must be less than α_{tr}^2 and α_{ex}^2.

Assuming that the initial angular distribution of beam molecules near the hexapole axis is uniform, the fraction of molecules transmitted is

$$A(U_o, v, \rho) = \frac{\alpha_o^2}{\alpha_{ea}^2} \tag{2.53}$$

where $\rho \equiv \cos\theta$ and α_o^2 is the smaller of α_{tr}^2 and α_{ex}^2. The probability of transmitting a given $|\mathrm{JKM}\rangle$ state is then

$$F_{\mathrm{JKM}}(U_o) = \int_o^\infty A(U_o, v, \rho) f_v(v) dv \tag{2.54}$$

where $f_v(v)$ is the beam velocity distribution. At a given hexapole voltage, the total transmission is

$$T(U_o) = \sum_{\mathrm{JKM}} F_{\mathrm{JKM}}(U_o) f_{\mathrm{JK}} \tag{2.55}$$

where f_{JK} is the rotational partition function for state $|\mathrm{JK}\rangle$ [Atkins, 1994]:

$$f_{\mathrm{JK}} = \frac{S(\mathrm{I},\mathrm{K})\, e^{-W_o/kT_{rot}}}{\sum_{\mathrm{J}=0}^{\infty} \sum_{\mathrm{K}=-\mathrm{J}}^{\mathrm{J}} S(\mathrm{I},\mathrm{K})\, e^{-W_o/kT_{rot}}} \tag{2.56}$$

for which W_o is the zero-field rotational energy and $S(\mathrm{I}, \mathrm{K})$ the statistical weighting factor due to nuclear spin, I [Townes and Schawlow, 1955]:

$$S(\mathrm{I},\mathrm{K}) = \begin{Bmatrix} 2(4\mathrm{I}^2 + 4\mathrm{I} + 3) & \mathrm{K} = 3n \\ 2(4\mathrm{I}^2 + 4\mathrm{I}) & \mathrm{K} \neq 3n \\ 4\mathrm{I}^2 + 4\mathrm{I} + 3 & \mathrm{K} = 0 \end{Bmatrix}. \tag{2.57}$$

A calculated and experimental total transmission curve for CH_3Cl is shown in Figure 2.11.

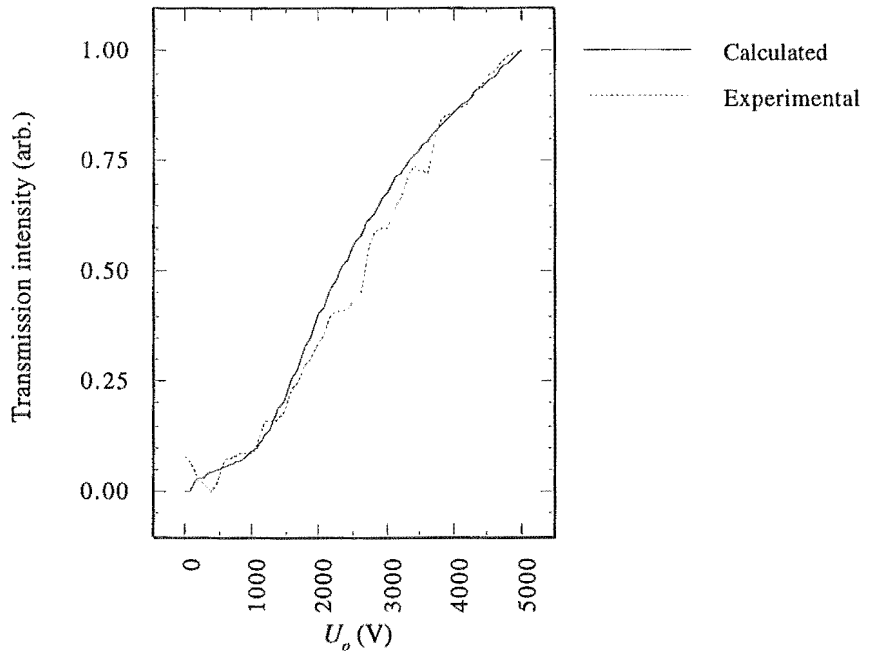

Figure 2.11 Calculated and experimental transmission curves for CH_3Cl.

2.4.6 Homogeneous orienting electric field

Molecules transmitted by the hexapole are state-selected but not oriented about any single laboratory axis. For steric asymmetry experiments described here and in other similar studies, a weak homogeneous electric field (10-20 V cm^{-1}) is placed after the hexapole. The field defines a space-fixed axis around which the MK < 0 Stark state molecules orient, remembering that the orientation is not necessarily perfect, but described by the angle θ such that the average value of $\cos\theta$ is

$$<\cos\theta>=\frac{MK}{J(J+1)}. \qquad (2.58)$$

The distribution of $\cos\theta$ or ρ for a given hexapole voltage is

$$P(\rho,U_o)=\sum_{J=0}^{\infty}\sum_{K=1}^{J}\sum_{M=1}^{J}P_{JKM}(\rho)F_{JKM}(U_o)f_{JK} \qquad (2.59)$$

where each term is defined previously in eqns. 2.33, 2.54 and 2.56. Figure 2.12 shows a calculated orientation distribution for CH_3Cl at 5.5 kV with experimental beam velocity and population distributions.

Average orientation $<\rho>$ for a hexapole voltage U_o is given by

$$<\rho>=\frac{1}{T(U_o)}\sum_{JKM}\frac{MK}{J(J+1)}F_{JKM}(U_o)f_{JK}\,, \qquad (2.60)$$

and for the distribution in Figure 2.12 the average value of $\cos\theta$ is 0.33.

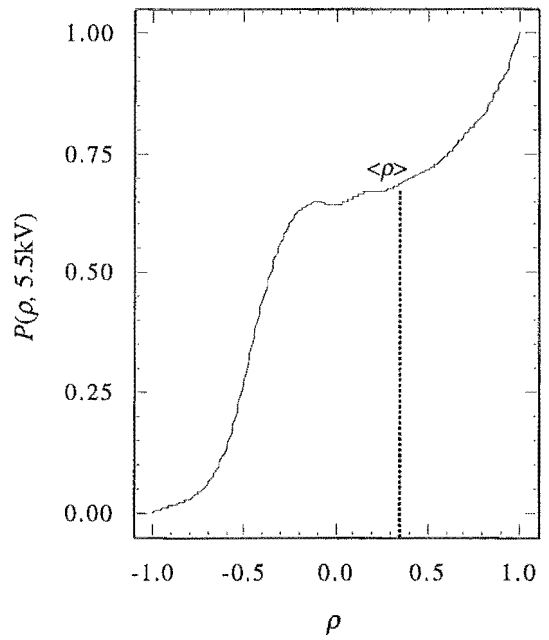

Figure 2.12 Calculated orientation distribution for CH_3Cl.

The focused upper Stark state molecules have a distribution of cos θ within the inhomogeneous field that is projected onto the space-fixed axis of the weak homogeneous field when they enter it. The success of this reprojection depends on two criteria being met. Firstly, a molecules passage from inhomogeneous to homogeneous

fields must be adiabatic, ie. the quantum numbers J, K and M remain constant. The extent to which $|JKM\rangle$ state *scrambling* occurs and the parameters which control it have been investigated by a number of researchers [Loesch and Remscheid, 1990]. Often, placing a field of intermediate strength, or guiding field, between the hexapole and weak homogeneous field has been deemed necessary and sufficient to maintain $|JKM\rangle$ state integrity. From a field strength of ~60 kV cm^{-1} through an intermediate 200 to 20 V cm^{-1} is however not significantly different than a transition straight from high to low field strength. The critical condition to be met is that $\omega_E << \omega_{\Delta M}$, where ω_E is the angular frequency of rotation of the electric field and $\omega_{\Delta M}$ the angular frequency of the transition between M-levels [Maltz, 1972]. Qualitatively, the projection of **J** onto the field axis must be able to follow the changing direction of that axis.

The second assumption is that rotational angular momentum, **J**, and nuclear spin, **I**, remain uncoupled in the weak field. The extent of coupling depends on the relative magnitudes of the rotational magnetic vector $\mathbf{M_J}$ and nuclear spin vector **I**. In high strength fields $\mathbf{M_J^2} >> \mathbf{I}^2$ and coupling is weak while in low fields the magnitudes may be similar and coupling significant [Walker and Straw, 1967]. If coupling does occur then the Clebsch-Gordan series gives a new quantum number,

$$F = J+I,\ J+I-1,\ J+I-2,\ \ldots,\ J-I \qquad (2.61)$$

and this projects onto the field axis as M_F. For molecules in higher rotational states where J >> I, the effect of coupling is negligible. However for low lying rotational states where J > I this may not be the case.

It is assumed that for this work any hexapole state-selected distribution of $\cos\theta$ is oriented about the space-fixed homogeneous electric field without significant degradation of that distribution. Successful orientation asymmetry experiments using a field strength of just 0.3 V cm^{-1} suggest that reprojection is faithful [Kaesdorf, 1985].

2.5 Collision cross-sections

Collisions between atomic or molecular species can result in a number of outcomes. Restricting this discussion to molecular species, there is the possibility of either an elastic collision where energy transfer occurs only between translational degrees of freedom or an inelastic collision where energy transfer to and from the internal modes of motion occurs. For the range of collision energies available with the molecular beam described here, inelastic collisions are limited to excitation or relaxation of vibrational or rotational modes.

At large separations r there is an attractive interaction between two species,

$$V(r) = -\frac{C}{r^6}, \tag{2.62}$$

known as the van der Waals interaction [Massey, 1969]. This arises from a dynamic polarisation of one molecule by the other, such that the electrons of both species are on average separated by the largest distance possible. For small separations there is a dominating repulsive interaction due to the Coulomb forces between nuclear particles and electrons. However, this repulsive or chemical force falls off exponentially with separation.

Transfer of energy between the two colliding species is governed by the interaction potential. A combined wavefunction may be described as the sum of sinusoidal frequency components. As collision species approach, the interaction potential is stronger and the wavefunction contains more frequency components which span a wider range of energies. It is the resonance between these frequency components and the energy level separations in either collision entity that facilitate energy transfer [Massey, 1969]. In general, the probability for energy transfer increases with decreasing separation r.

The largest separation at which energy transfer may occur, r_{max}, leads to the definition of a cross-section for the process:

$$\sigma = \pi r_{max}^2. \tag{2.63}$$

Measurement of cross-section and the subsequent determination of r_{max} is the subject of experiments in §4. Where there is a change in the velocity of at least one of the collision species as a result of energy transfer, cross-sections may be measured using a beam-scattering cell apparatus. A beam of molecules is directed through a scattering cell of length L pressurised with the other collision species to a particle density n. Incident beam intensity, I_o, is attenuated by the scattering species an amount described by the Beer-Lambert equation

$$\frac{I}{I_o} = \mathrm{e}^{-nL\sigma}, \tag{2.64}$$

where I is the attenuated beam intensity and σ the cross-section for the process [Atkins, 1994]. Beam intensity is recorded at a number of scattering cell pressures and cross-section is then determined from

$$\ln I = -nL\sigma + \ln I_o \text{ (§4.2.3).} \tag{2.65}$$

The amount of energy transferred to or from the beam molecule is quantised and there will be a minimum non-zero deflection possible. Resolution of the beam-scattering cell apparatus will determine whether this minimum deflection is observed. This resolution is described in terms of the angle made between the beam axis and the circumference of the detector entrance aperture (§4.2). For typical cross-section experiments the apparatus is constructed so that this angle is less than 10'. The investigation of heavier

species for which the minimum deflection will, in general, be less requires higher resolution (smaller angle) to observe the total cross-section.

The beam-scattering cell method is not suitable for the measurement of cross-sections where there is energy transfer between internal degrees of freedom without a change in translational energy. The technique employed here overcomes this limitation. Symmetric top molecules experience a radial force within the hexapolar electrostatic filter dependent on the quantum numbers J, K and M (§2.4.1). This force results in trajectories through the filter that are directed toward the beam axis for $MK < 0$ and divergent for $MK > 0$. A collision process involving change in one or more of the rotational numbers will result in a different trajectory, possibly leading to loss from the transmitted beam. Beam intensity is recorded as a function of pressure for each quencher, and cross-sections determined by the Beer-Lambert equation (§4.2).

Interpretation of the measured cross-sections requires a knowledge of the energy transfer processes involved. The contribution of elastic and inelastic collisions, excluding those where energy transfer results in defocusing, is determined first and subtracted in the following manner. With the hexapole switched off beam attenuation is the result of elastic and inelastic collisions. Subtracting the 'hexapole off' intensity from the 'hexapole on' intensity leaves the intensity of molecules focused by the hexapole filter. Attenuation of these molecules is the result of collisions involving rotational energy transfer.

Characterisation of the rotational energy transfer in terms of a change in J, K or M quantum numbers is more difficult. A comparison of the energy available from the interaction potential with the energy levels of a symmetric top molecule and a knowledge of the appropriate transition selection rules provides an indication of the likely transitions.

In the absence of an electric field the rotational term of a symmetric top molecule is

$$F(\mathrm{JKM}) = BJ(J+1)+(A-B)K^2 \text{ in cm}^{-1} \qquad (2.66)$$

where A and B are the rotational constants in wavenumbers. Each $|JK\rangle$ state is split into 2J + 1 Stark states when the molecule is subjected to an electric field. The energy of these states is given by

$$W = \mu\varepsilon\frac{MK}{J(J+1)}. \qquad (2.67)$$

Figure 2.13 shows the low lying rotational states of a prolate symmetric top molecule. The selection rules for rotational transitions are: $\Delta J = 0, \pm 1$; $\Delta K = 0$; and $\Delta M = 0, \pm 1$ [Townes and Schawlow, 1955]. A transition where there is no change in the quantum numbers J and K results from the inversion properties of symmetric top wavefunctions. This type of transition is not measurable with the apparatus described here. Symmetric top molecules are deflected within the hexapole filter only when the three rotational quantum numbers are non-zero. This further restricts transitions to those where $K \neq 0$, and because the technique probes upper Stark states the initial state must have $MK < 0$, leaving the following possibilities:

- $\Delta J = 0$, $\Delta M = \pm 1$ where $|K| > 0$, $J > 0$ and $MK < 0$.
- $\Delta J = \pm 1$, $\Delta M = 0, \pm 1$ where $|K| > 0$ and $MK < 0$.

It should be noted that the convention of expressing both K and M quantum numbers as positive integers in Dirac notations is used throughout this thesis, but in fact for upper Stark states either M or K must be negative. The minimum energy separation of a $\Delta J = \pm 1$ transition where K = 1 is 21.2 J mol^{-1} (4B) for the molecule CH_3Cl. Energy differences between Stark states decrease with increasing J. Within the hexapole filter described here (§3.6) the energy separation between $|111\rangle$ and $|110\rangle$ states for a CH_3Cl

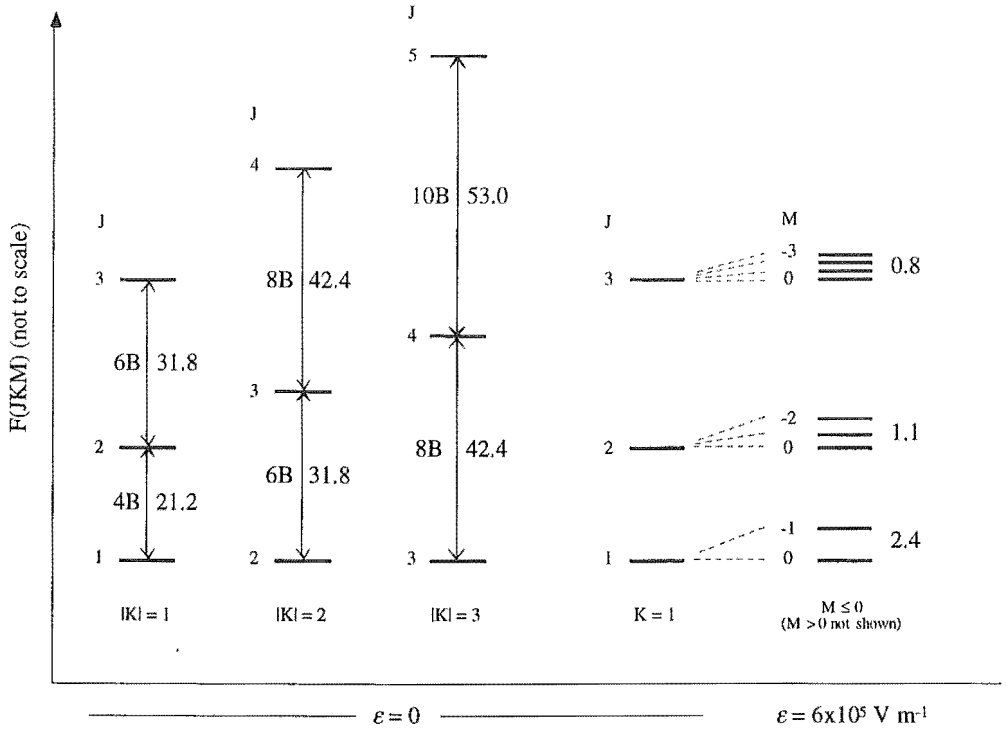

Figure 2.13 Low-lying rotational energy levels of a prolate symmetric top. Energies between adjacent states are for CH_3Cl in J mol^{-1}.

molecule displaced a radial distance r_o from the beam axis is 9.6 J mol^{-1}. However, the average displacement of molecules that are focused will be less than r_o. A better estimate for the average displacement might be $r_o / 2$. At this distance the field strength is reduced to 1/4 of the previous value and energy separation between the states noted above is 2.4 J mol^{-1}.

The energy available from a van der Waals interaction depends on the charge distribution properties (polarisability and dipole moment) of both beam and quencher species. Recalling the expression for the interaction (eqn. 2.62), it is the van der Waals constant, C, that contains this information. The constant may be expressed as the sum

$$C = C_{disp} + C_{d-ind} + C_{d-d} \qquad (2.68)$$

where the three terms (from left to right) are for dispersion (London), dipole-induced dipole, and dipole-dipole interactions [Massey, 1969]. Expressions for the interaction terms are:

$$C_{disp} = \frac{2}{3}\alpha_1'\alpha_2'\frac{I_1 I_2}{I_1 + I_2}; \tag{2.69}$$

$$C_{d-ind} = \frac{\mu_1^2 \alpha_2'}{4\pi\varepsilon_o}; \text{ and} \tag{2.70}$$

$$C_{d-d} = \frac{2\mu_1^2\mu_2^2}{3(4\pi\varepsilon_o)^2 k\overline{T}_r}, \tag{2.71}$$

where the subscripts 1 and 2 refer to the individual collision species, α' are polarisability volumes in 10^{-30} m^3, I are ionisation potentials in volts, μ are dipole moments in C m, and $\overline{T}_r$ is the average rotational temperature of the two dipoles

$$\overline{T}_r = \frac{2T_{r,1}T_{r,2}}{T_{r,1} + T_{r,2}}. \tag{2.72}$$

Using a CH_3Cl-Ar beam-quencher combination as an example, $C_{d\text{-}d}$ is zero and the remaining terms are approximately $5.8\text{x}10^{-78}$ J m^6. Transitions of ΔJ or $\Delta M = \pm 1$ as calculated above would require beam-quencher separations of 7.4 and 10.6 Å, respectively, or less.

Experimental cross-sections of higher than 150 Å^2 suggest that interaction occurs at a separation of at least 7 Å. For CH_3Cl-Ar the measured cross-section of 224 Å^2 corresponds to a separation of 8.4 Å. The values of 7.4 and 10.6Å calculated above are only the maximum separations at which there is sufficient energy from the interaction to permit a transition. The probability of transition is dependent not only on the distance but the transition dipole moment. A theoretical treatise would be required to consider the relationship between r_{max} and the observed value of r obtained from cross-section

data. However, calculated values of r_{max} do suggest that both $\Delta J = \pm 1$ (for low J) and $\Delta M = \pm 1$ transitions are responsible for the observed defocusing of upper Stark state molecules from the hexapole filter.

2.6 Electron impact ionisation

The process of electron impact ionisation forms an integral part of many analytical instruments and devices, such as mass spectrometers, ionisation gauges and manometers, and ion sources. Despite such wide use a definitive theoretical model accounting for the experimentally observed energy dependence and ion fragmentation patterns is lacking.

Total ionisation cross-sections have been reported for decades though the accuracy of methods used and assumptions made are called into question [Harris and Harland, unpublished results]. Otvos and Stevenson proposed that total ionisation cross-sections for molecules are the sum of constituent atoms' ionisation cross-sections which in turn are given by the sum of the valence electrons weighted by the mean square radii of those electrons [Otvos and Stevenson, 1956]. Subsequently this was shown to be false [Lampe, 1957]. Lampe, *et al.* reported cross-sections for 35 compounds at 75 eV and these values have remained the accepted *true* values at that energy until the present day [Lampe, 1957]. In the same paper, a linear relationship between total ionisation cross-section and polarisability was shown.

The energy dependence of electron impaction ionisation is characterised by three distinct regions, explained qualitatively in relation to the following direction ionisation process

$$A + e^- \rightarrow A^+ + e^-_{fast} + e^-_{slow}. \qquad (2.73)$$

At the appearance potential ionisation occurs only if all the energy of the approaching electron is transferred to A. Increasing electron energy requires less than total energy transfer and so the interaction distance need not be as close. As energy is increased farther, above about 70 to 80 eV the cross-section peaks and then falls gradually. The general decrease with electron energy is predicted by the Born approximation, where A remains stationary during any interaction and the electron behaves most like a particle [Massey, 1969]. It is then simply a hard sphere calculation in which the excitation probability is inversely proportional to the electron's velocity. A more elegant explanation for the observed cross-section decrease at higher energies is given by Hagstrum [Hagstrum, 1953]. Transition probability is proportional to the amplitude and width of the Fourier frequency envelope centred about the transition energy. As electron velocity increases the interaction time decreases and the corresponding frequency envelope narrows.

More detailed information of the impact and ionisation processes is available from electron-molecule scattering experiments. The momenta of all ingoing and outgoing particles are determined to give a differential cross-section. Both electron impact ionisation and elastic electron scattering processes have been investigated by this dynamical approach [Ehrhardt, 1986; Brauner, 1989].

Differential elastic electron scattering cross-sections from both oriented (CH_3Cl, CH_3I) and randomly directed fluoro-methyl halides indicates that there is a dependence on the charge distribution within the molecule [Meier, 1994]. Electron impact ionisation differential cross-sections have only been reported for randomly directed species, a majority being for H and He [Brauner, 1989; Srivastava and Sharma, 1988].

Experiments reported in §5 were undertaken to futter advance our knowledge of entrance channel effects for alkali metal-alkyl halide reactions, as outlined in §1. The

initial interaction is considered and modelled, along with an examination of molecular ion fragmentation which gives some information on the potential energy surface exit channel.

To summarise, the success of ionisation by electron impact at moderate to high electron energies is shown to be dependent on molecular polarisabilities. These polarisabilities reflect the degree to which nuclear charges control electron distribution and prevent distortion of that distribution in an electric field [Atkins, 1994]. Crucial to any explanation of the results in §5 is the assertion that molecular polarisability is constructed from atomic polarisabilities and is therefore non-uniform or variable about the molecule.

2.7 Ion detection

Detection of charged particles is most simply achieved by collecting them on a metal plate. The current which results when the plate is connected to an electrometer is recorded. While simple, this method has numerous limitations.

Typically ionisation of background gas by the electron beam used here results in the formation of approximately 5×10^4 ions per second. Assuming that all ions are collected on the metal surface, this corresponds to a current of 8×10^{-15} coulombs per second, or approximately 10 femtoamperes. Measurement of such a current is possible but very difficult. Short time-scale changes in ion intensity, say from a pulse of ionised molecular beam, are lost due to the large time constant inherent in the amplification required. Negative biasing of the surface to improve collection efficiency and reject electrons would be necessary. However electronic and electrical noise from power supplies and other proximate devices would be picked up by the electrometer and hamper precise measurements.

Ions formed in this work are instead collected by a Channeltron electron multiplier (Galileo Electro-Optics), or particle multiplier [Kurz, 1979]. The Channeltron (Figure 2.14) is constructed of a special glass, heavily lead-doped. Internally coated with a semiconductive layer, resistance between the cone and channel output is typically 10^8 to 10^9 ohms. Chrome deposited on the outside of the multiplier provides a means of electrical contact. High negative voltage (1-2 kV DC) is applied to the Channeltron cone while the output end is usually set to ground potential. An ion of sufficient energy (see below) striking the inside cone surface will cause the emission of at least one secondary electron. This electron is accelerated by the field present within the channel until it strikes the channel surface. If the electron has gained enough energy from the field, more than one secondary electron will be emitted. This process is repeated 10 to 20 times along the channel depending on the field strength and multiplier dimensions. Electrons exiting the output are collected by a metal cup and measured.

Channeltrons are curved to prevent a process called *ion feedback* [Kurz, 1979]. At the output there are a large number of electrons which results in a high probability of ionising residual gas within the channel. Some of these ions strike the channel surface emitting electrons which are then multiplied in the usual manner. Curvature of the

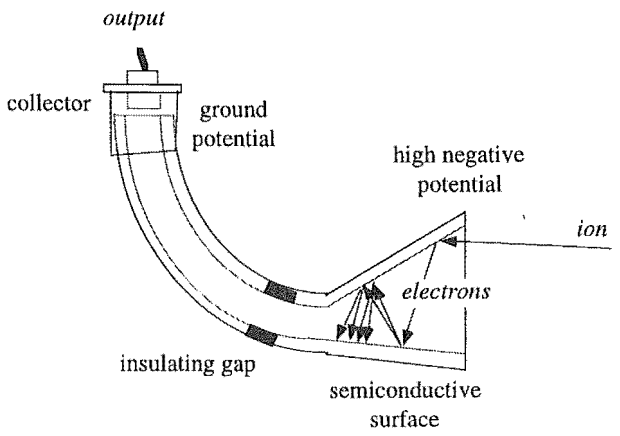

Figure 2.14 Channeltron electron multiplier (section view).

channel reduces the distance ions are able to travel back toward the cone and hence the magnitude of any resulting electron emissions. A gain of 10^8 from the single input ion is possible, from the previous example a current of 10 fA becomes 1 μA, and this is easily measured.

Emission of a secondary electron by ion impact is analogous to the photoelectric effect. Energy gained by the ejected electron is the difference between kinetic energy of the ion and the channel surface work function,

$$E_{e^-} = E_{i^+} - \phi. \qquad (2.74)$$

When the ion velocity is below some threshold emission does not occur. The semiconductive layer on the Channeltron has a very low work function to promote secondary emission. Increasing the cone potential raises impact ion energy and the probability of emission and subsequent electron multiplication.

Signal from the multiplier is processed and recorded in one of two ways. Each packet of electrons exiting the channel has a duration of approximately 10^{-8} seconds. When ions strike the multiplier cone at a rate of less than 100 MHz (in practice the dynamic range is 1 MHz) individual packets may be *counted.* The cup is connected to a special amplifier that transforms the electron pulses into voltage pulses. These are amplified to 5 V and broadened to approximately 200-300 ns. A ratemeter or more complex pulse counting device measures the impact of *each* successfully impacting ion. Noise from sources such as ion feedback are discriminated against with a variable current threshold in the amplifier unit. A 'dark count' level of between 10^{-2} and 1 counts per second is typical for Channeltron devices [Kurz, 1979].

Where higher ion intensities exist and pulses of electrons overlap analogue amplification is necessary. The amplified signal (say 10^{-1} V amplitude) may be

accumulated by a digital storage adaptor or similar device. Time constants for this processing are approximately 50 μs. Events on a millisecond time-scale such as the arrival of a molecular beam pulse are separable from the background DC signal level.

While providing excellent amplification of ion signals, particle multipliers are prone to degradation and even failure. The lifetime of a Channeltron is normally several years when used daily - gain is shown to decrease as the number of accumulated counts approaches 10^{11} [Kurz, 1979]. However, exposure of the device to organic materials, such as mechanical pump oil vapour, coats the secondary emissive surface and lowers gain. Cleaning the glass surface with solvents is only partially effective in halting the damage.

At pressures $\geq 10^{-4}$ torr, operation of the multiplier can result in an electrical discharge along the channel surface. The discharge ablates the semiconductive layer and renders the Channeltron useless.

Chapter 3

Molecular Beam Machine

3.1 Introduction

The experiments to measure electron impact on oriented molecules and to determine upper Stark state relaxation cross-sections, reported in §5 and §4, respectively, required the design, construction and subsequent characterisation of a molecular beam apparatus or machine. Components of the molecular beam machine are described in an order based on the chronological sequence of events that occur during experiments:

- the vacuum system
- sample handling
- supersonic beam source
- supersonic beam alignment
- hexapole state selector
- electron beam source
- detectors
- homogeneous field plates
- computer interfacing

Sections detailing the electron beam source and homogeneous field plates are applicable to §5 only, while the section for the Channeltron electron multiplier and ion source unit applies to §4 only. The differences between the two sets of experiments are discussed in §4.2 and §5.2.

3.2 Vacuum system

3.2.1 Machine support frame

The molecular beam machine sits on a frame designed to meet three requirements: flexibility to change experimental configuration; ease of access to chambers, flanges and pumps; and strength to support the weight of all current and future machine components. Figure 3.1 illustrates the frame and important dimensions. Seven supports, welded from 2" x 1" tubing, hold two 3" x 2" beams or rails 320 mm apart. Two 5 mm x 10 mm bars running almost the entire rail length are pop riveted 20 mm apart to one rail. These bars provide a groove in which the chamber mounts may be moved (see below). Two rubber feet screw into the bottom of each support and are adjusted so that both rails are level. Supports, where indicated, are bolted together in pairs with four horizontal braces and also to the rails. 1" square braces are bolted between the rails in three locations to maintain their parallel spacing. Two diagonally opposed cross-braces (also shown) provide additional low frequency vibration damping. All frame components with the exception of the 8 mm stainless steel bolts are of mild steel and are coated with anti-corrosion and green semi-gloss enamel paints.

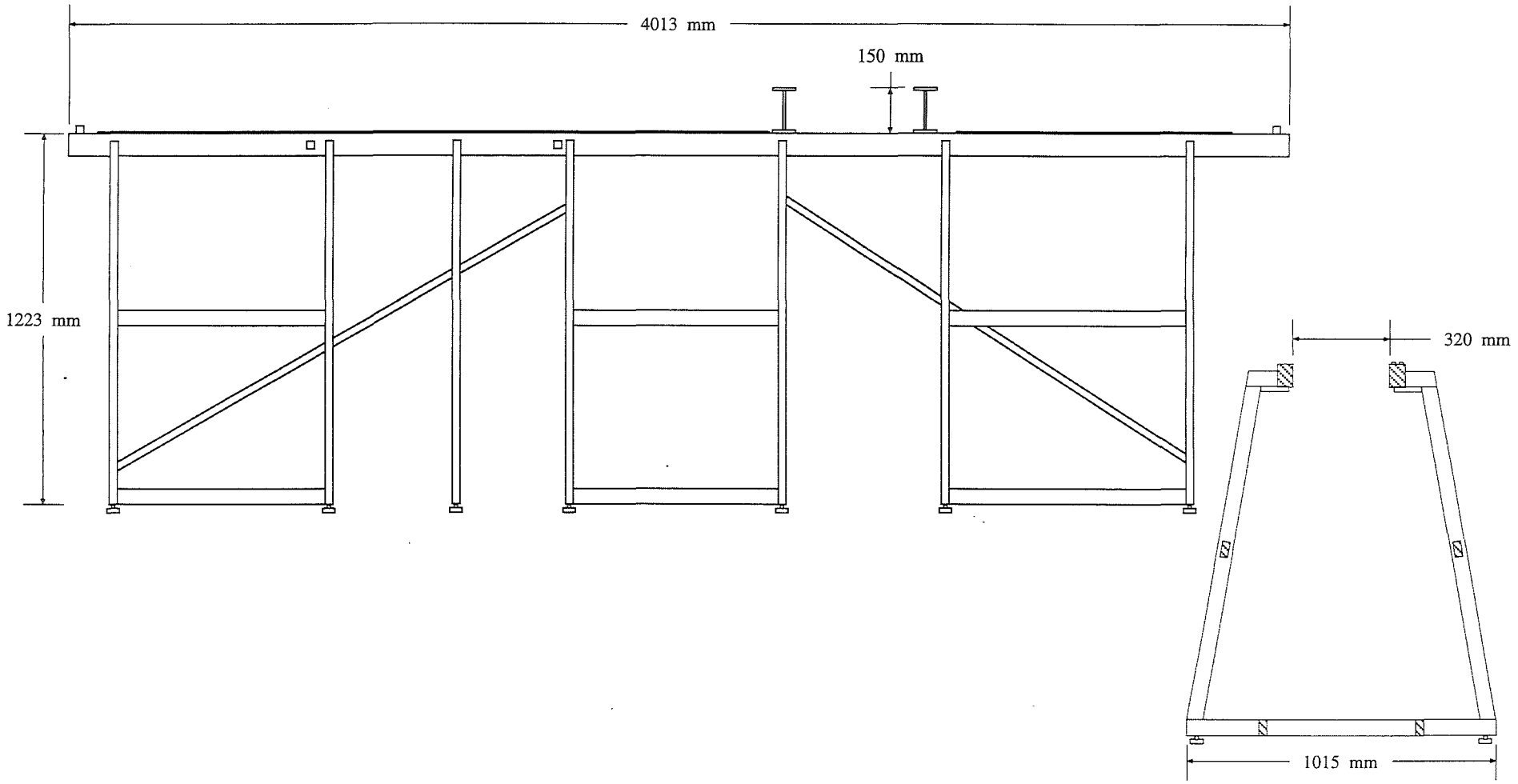

Figure 3.1 Molecular beam machine support frame. Scale 1:20.

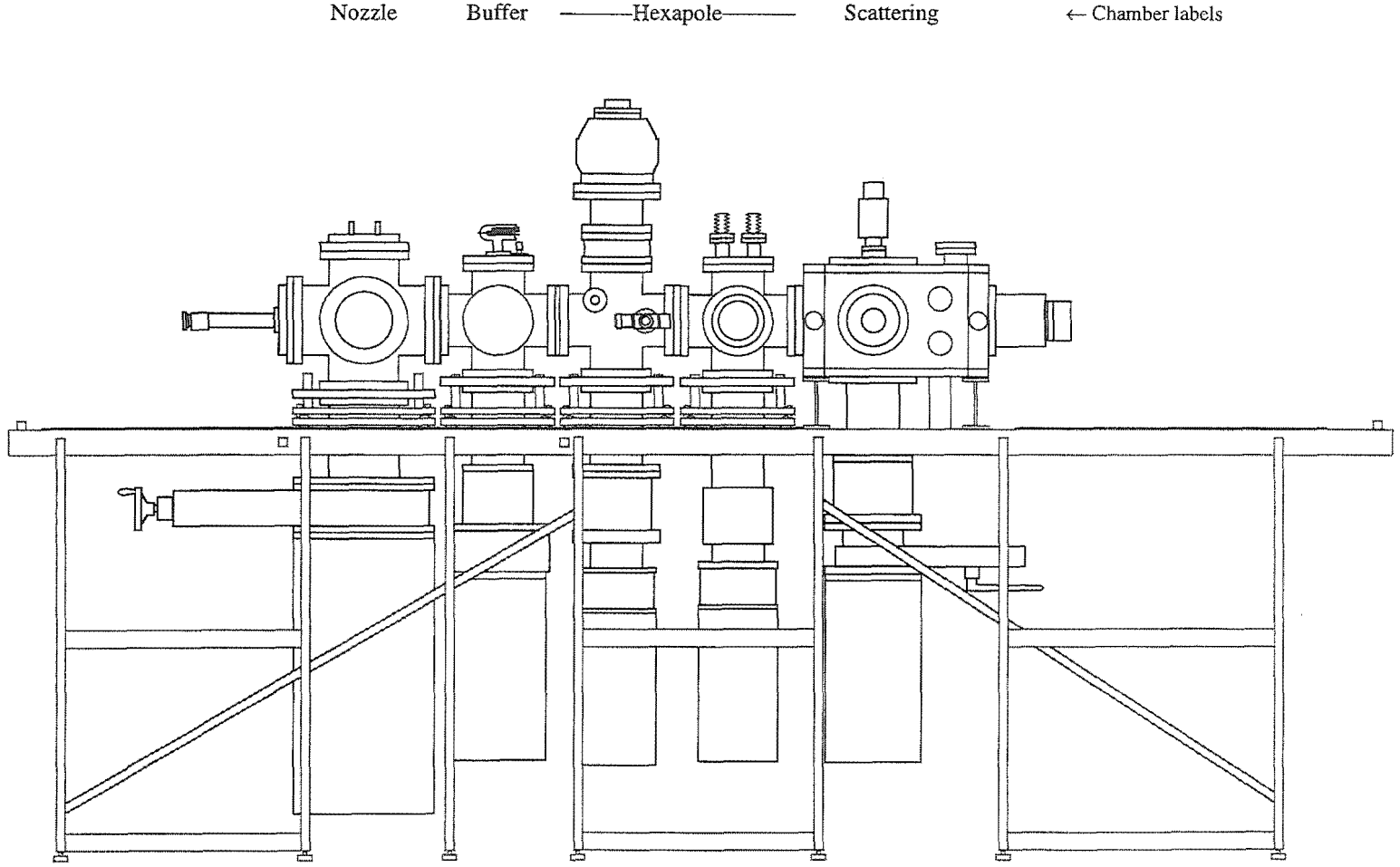

Figure 3.2 Molecular beam machine (side on). Scale 1:20.

3.2.2 Chambers and mounts

The vacuum assembly comprises five chambers bolted together and supported on heavy mounts sitting on the guiding rails. These are the nozzle, buffer, hexapole one and two, and scattering chambers (Figure 3.2). Excluding the scattering chamber, every other chamber is mounted to separate *xyz*-translators facilitating initial alignment of the machine and subsequent reconfiguration or maintenance. Each translator, an example for 8" OD Conflat flanges is shown in Figure 3.3, consists of three 20 mm thick stainless steel plates, one for every spatial direction. A chamber bolts to the upper side of the top plate while a spool, gate valve and diffusion pump are secured to the under side. All flange/plate interfaces are sealed by Conflat knife edge and copper gaskets.

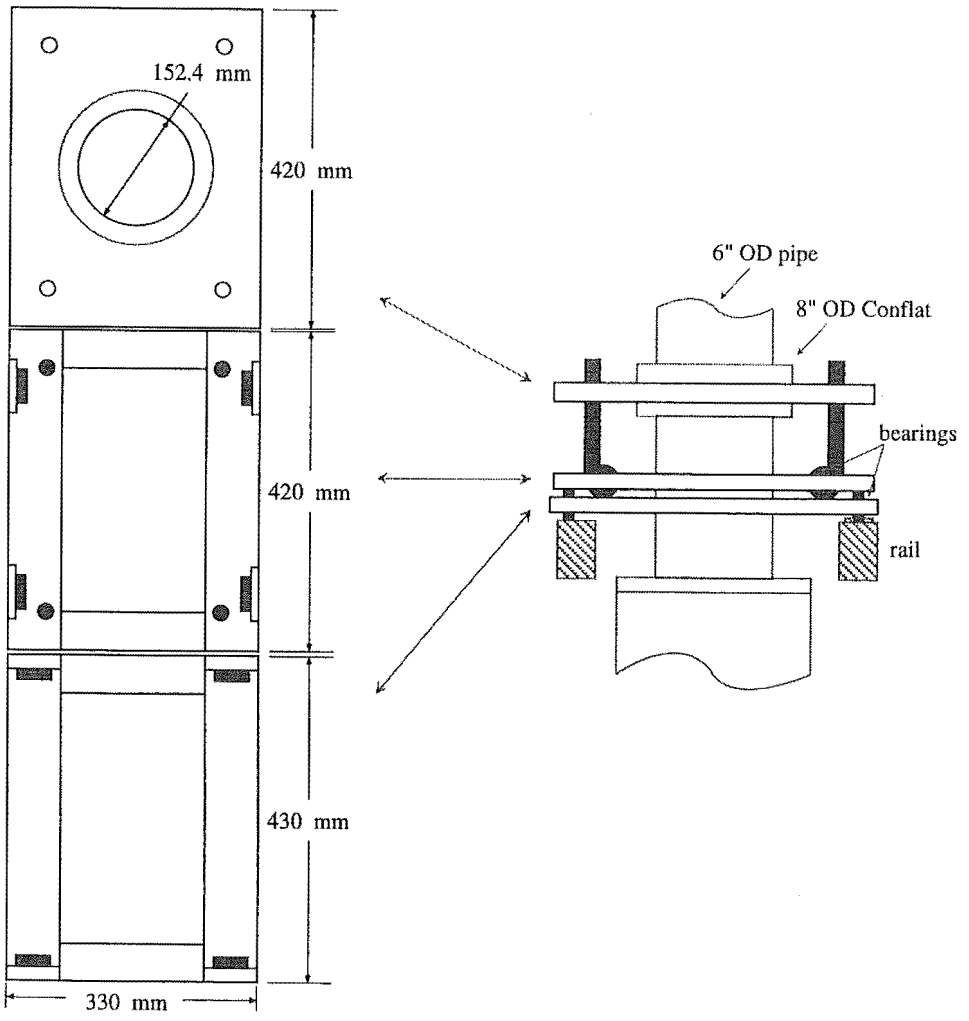

Figure 3.3 Chamber mount. Scale 1:10.

3.2.2.1 Nozzle chamber

A 10" OD flange stainless steel 6-way cross (Huntington Laboratories) houses the supersonic nozzle, Figure 3.4. The high gas load during nozzle operation is adequately handled by a 7020 l/s (for helium) Varian, VHS-10 diffusion pump and backed by a 1080 l/min Alcatel, 2063C mechanical pump. Isolation of the chamber from the diffusion pump is achieved by an aluminium-bodied gate valve (Duniway Stockroom, 10") mounted directly above the pump. The height of the gate valve is lowered with a spacing spool connected between the valve and the chamber's translator. A liquid nitrogen trap comes down from the top chamber arm. Attached to the trap are two long copper plates that clamp a copper venetian blind baffle welded to a copper ring above the chamber's bottom arm. This baffled cold surface provides sufficient protection against oil backstreaming while not reducing the effective pumping speed significantly. Typical pressures with the nozzle open, measured by a glass-housed ion gauge (Duniway Stockroom, T-100-K) on a chamber side-arm, are 10^{-4} to 10^{-5} torr.

3.2.2.2 Buffer chamber

The buffer chamber is illustrated in Figure 3.5. This chamber and pumping system serves to buffer the pressure of the nozzle chamber from the hexapole and scattering chambers and it comprises an 8" OD flange 6-way stainless steel cross (Huntington Laboratories). Plates fitting snugly into the arms along the machine axis almost completely seal the chamber. On each plate is mounted a skimmer for the molecular beam to pass through. Pressures of 10^{-6} to 10^{-7} torr are maintained by a 3000 l/s Varian, VHS-6 diffusion pump backed by a 700 l/min Edwards, E2M40 mechanical pump. Maximum pumping speed in the buffer chamber is less important than an oil free vacuum so a baffled liquid nitrogen trap (inset of Figure 3.5) is mounted inside the spool directly above the isolation gate valve (NRC, 77).

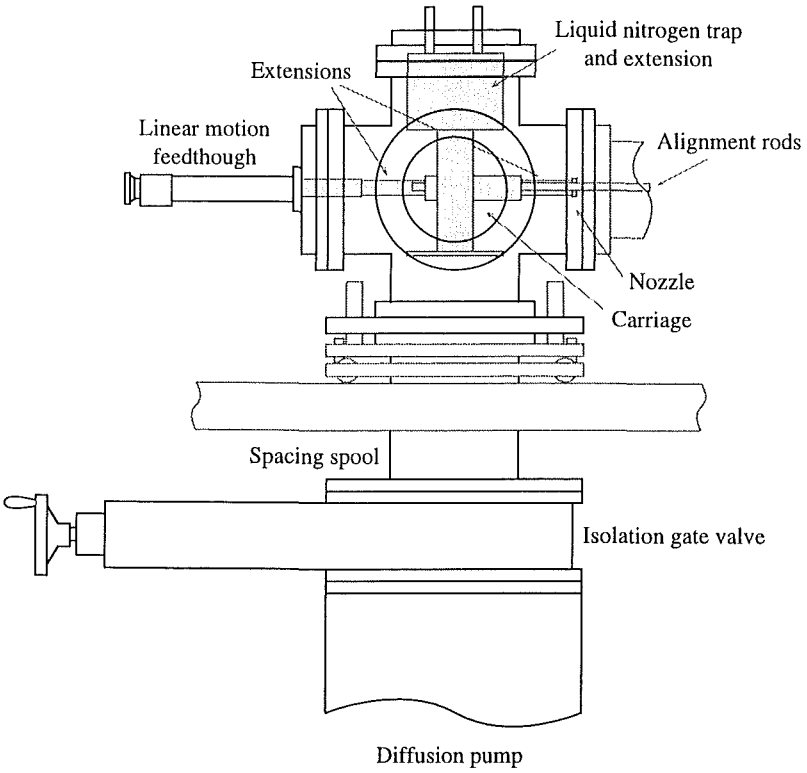

Figure 3.4 Nozzle chamber. Scale 1:12.

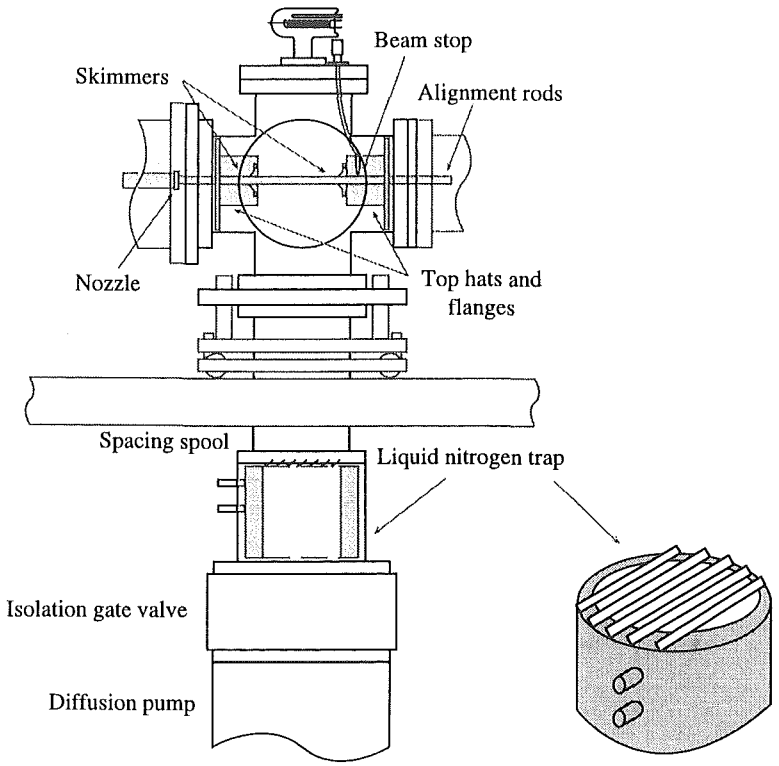

Figure 3.5 Buffer chamber. Scale 1:12.

3.2.2.3 Hexapole chambers

Two 8" OD flange chambers house the hexapole electrostatic filter, see Figure 3.6. The first chamber is made from a 4-way stainless steel cross (Varian) with three 2 3/4" Conflat flange spigots to which are attached an ion gauge (Duniway Stockroom, T-100-K), a variable leak valve (Leybold Heraeus, 283-41 DN 10 KF), and a blank flange. Mounted on top of the chamber is a 540 l/s Alcatel, TMP5900CP turbomolecular pump backed with a 373 l/min Alcatel, 2020A mechanical pump. This turbomolecular pump is operated at night to maintain a machine pressure of 10^{-6} torr. It is isolated during experiments with a pneumatic bellows sealed gate valve (Alcatel, CF 150). The second is a 6-way stainless steel cross (Huntington Laboratories), two 2 3/4" Conflat flange ceramic high voltage feedthroughs (Huntington Laboratories) are mounted into the

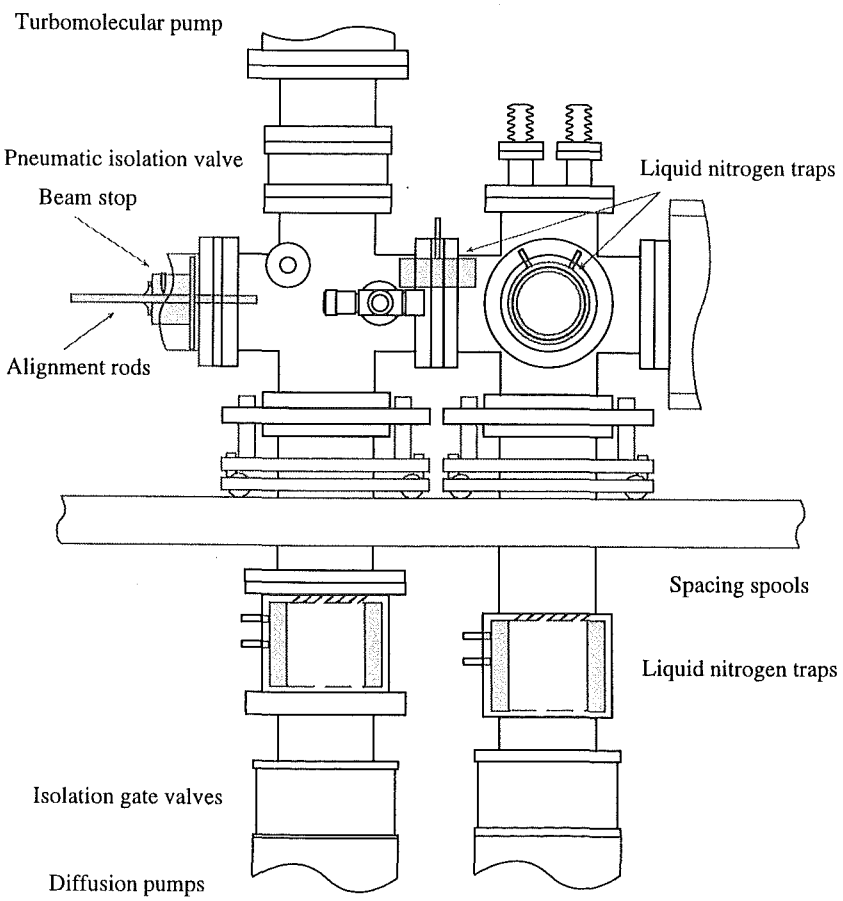

Figure 3.6 Hexapole chambers. Scale 1:12.

topside 8" OD Conflat. The positive and negative 0-30 kV required for hexapole operation are connected to these feedthroughs. Below both chambers are spacing spools, baffled liquid nitrogen traps, isolation gate valves (Airco Temescal, 5010) and 1500 l/s Varian, VHS-4 diffusion pumps. Backing the first VHS-4 is a 342 l/min Edwards, EDM20 mechanical pump and the second an 75 l/min Alcatel, 2004A pump. Two additional liquid nitrogen traps are placed in the chamber volumes: a half-moon-shaped trap above the hexapole, in the arms joining both chambers; and a donut-shaped trap in one of the side-arms of the 6-way cross. Operating pressure for the electron impact orientation experiments is ~10^{-7} torr and less than $5x10^{-5}$ torr for the upper Stark state relaxation experiments.

3.2.2.4 Scattering chamber

A custom designed and fabricated stainless steel chamber machined in the Chemistry Department's Mechanical Workshop rests on two I-beams placed across the frame rails (Figure 3.7). The chamber consists of a base, mid-section and lid, sealed together with two large Viton 'o'-rings coated with diffusion pump oil. Clamps around the chamber prevent movement of the individual sections. Three bolts positioned triangularly in the I-beams fit into machined recesses in the base. The chamber is levelled by adjusting these bolts. Numerous 2 3/4", 4 1/2", 8", and 10" OD Conflat flange faces are machined into each section of the chamber. Over two hundred 8 mm tapped holes inside the mid-section allow mounting of vacuum components. A 1 ton lifting crane mounted on a rail attached to the roof and running more than the length of the machine is used to raise the chamber lid. Spacing spool, baffled liquid nitrogen trap, isolation gate valve (Vacuum Research Manufacturing Company) and 3000 l/s Varian, VHS-6 diffusion pump are mounted to a 10" OD Conflat flange face on the chamber base. The diffusion pump is backed by a 726 l/min Varian, SD700 mechanical pump. An ion gauge mounted to the chamber lid measures a pressure of low 10^{-8} torr. During operation this pressure rises to between 10^{-6} and 10^{-7} torr.

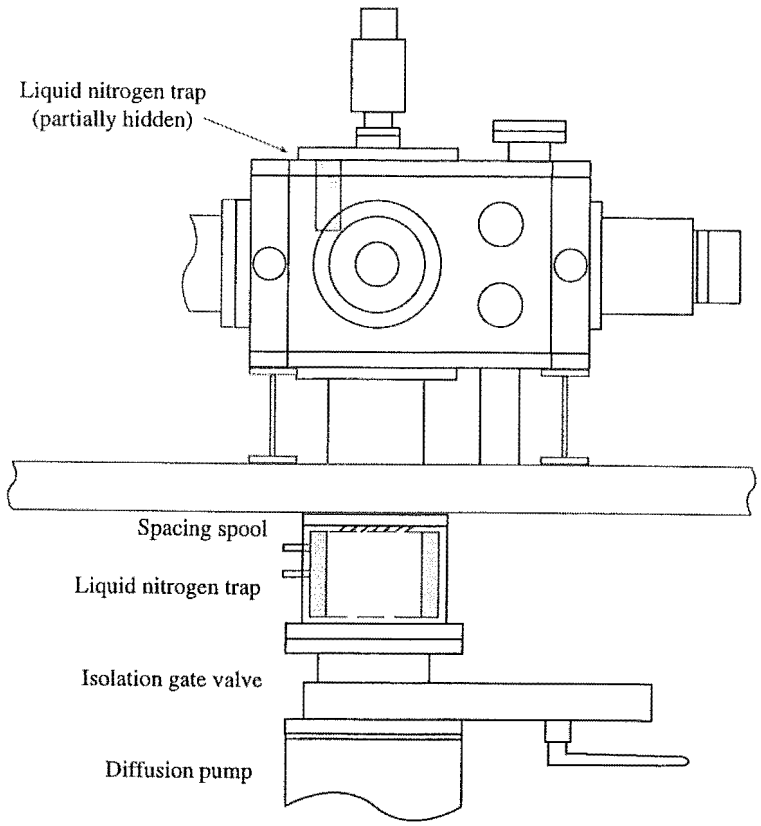

Figure 3.7 Scattering chamber. Scale 1:12.

All gate valve/spool and gate valve/diffusion pump interfaces are sealed on Viton 'o'-rings coated with diffusion pump oil. Forelines, that is the connecting tube between diffusion and mechanical pumps, are constructed of 1 1/2" and 2" flexible stainless steel bellows and sealed at both ends by Alcatel NW25 or NW40 fittings. Isolation between diffusion and mechanical pumps is achieved by bellows valves (stainless steel gate valve for the VHS-10). The nozzle and scattering chamber forelines are also connected directly to their respective chambers via stainless steel bellows valves. Both valves are opened to pump the machine volume from 1 atm to 10^{-4} torr. The turbomolecular pump is then used to lower the pressure to 10^{-6} torr before finally filling the liquid nitrogen traps and opening the diffusion pump isolation gate valves. Diffusion pumps are charged with DC705 silicone oil (Corning) and mechanical pumps with CVP-190-5 oil (Duniway Stockroom). Mechanical pumps are overhauled periodically and their oil changed every six months. Cooling water is directed to the turbomolecular and

diffusion pumps from a seven port inlet/outlet manifold. Power to all pumps is supplied from a distribution board next to the pressure measurement and protection control panels.

3.2.3 Vacuum monitoring and protection

As mentioned in preceding paragraphs, pressure inside the machine is measured with a number of ionisation gauges (Duniway Stockroom, T-100-K) each of which is connected to an MKS model 290 control and readout unit. Calibrated for air, the gauges have an operational range of between 10^{-3} and 10^{-9} torr. Above 10^{-3} torr the gauge filament is automatically switched off to prolong its life. Pressure in the pump forelines is usually higher, in the range of 10^{-1} to 10^{-4} torr, and up to 1 atm during pump down. Thermocouple gauge heads (Duniway Stockroom, DST-531), which operate over this pressure range, are fitted into each foreline and connected to MKS model 286 control and readout units. An additional thermocouple is used to sample the high vacuum region in the scattering chamber and monitors pressure during pump down. Temperature sensors are bolted to the side of each diffusion pump which provides an accurate assessment of the cooling water flow rate. Water pressure failure results in a temperature increase on the pump surface from approximately 45 to 100 °C in a short space of time and eventually to the oil boiling point which is over 200 °C.

The MKS ion gauge and thermocouple controllers have adjustable pressure set points which, if exceeded, cause relay outputs on their rear panel to open. Outputs from one ionisation gauge controller and all thermocouple controllers, along with the temperature sensor signals, are fed into a vacuum protection unit.

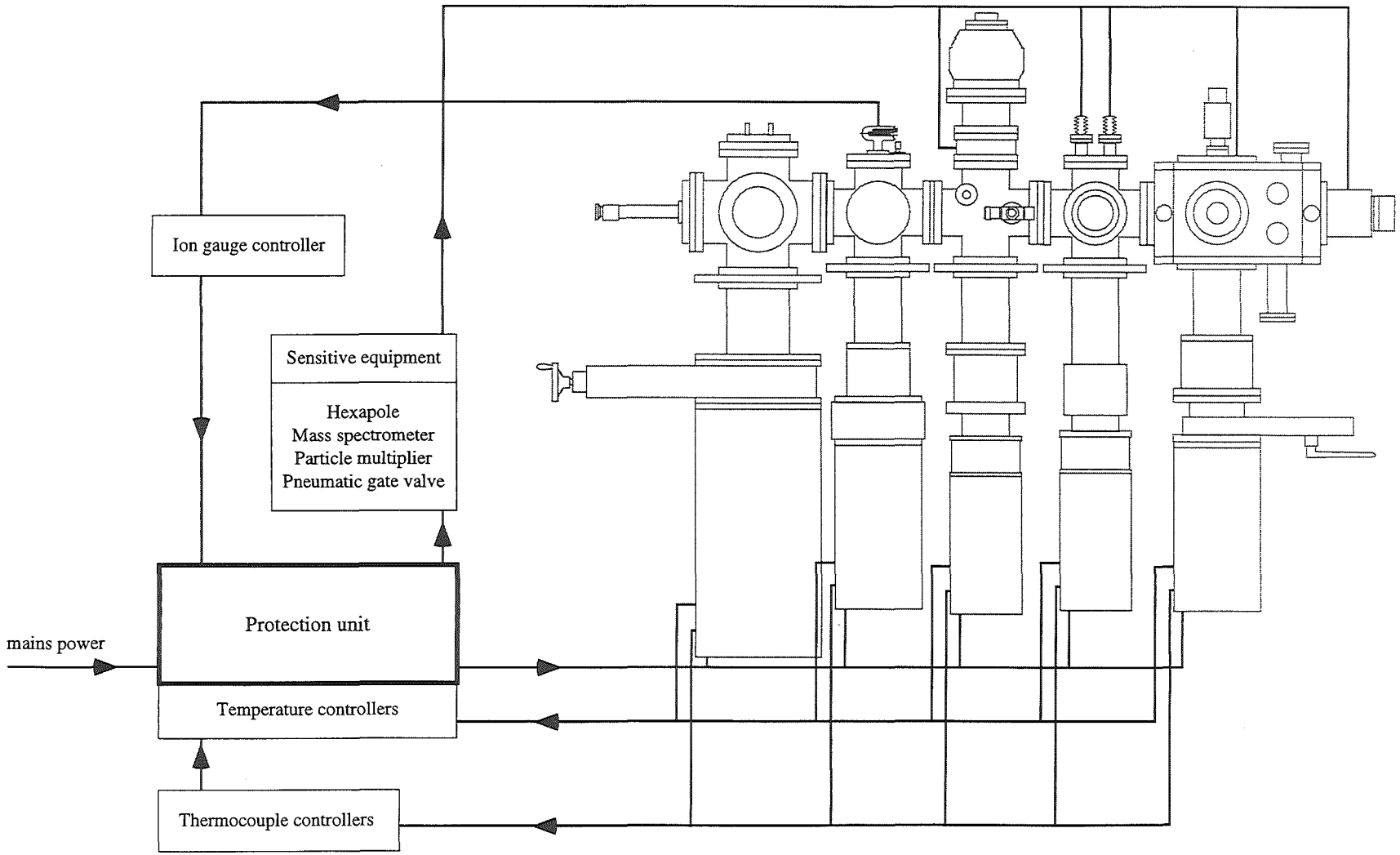

Figure 3.8 Vacuum protection scheme.

The vacuum protection unit illustrated in Figure 3.8 was designed and fabricated by the Chemistry Department's Electronics Workshop, it controls power supplied to all diffusion pumps, the turbomolecular pump pneumatic gate valve, and sensitive electronics. Events resulting in protective action are summarised:

- Cooling water failure. When the temperature on any diffusion pump exceeds an internally set maximum, power to all diffusion pumps is shut off. This supply must be manually restarted after the fault is corrected.
- Foreline pressure rise. Power to the appropriate diffusion pump is switched off when the thermocouple set point relay opens. Often this occurs when the nozzle is operated with long open times and the gas load becomes too much for the pumps. When pressure falls again power is automatically restored to the pump.
- Loss of high vacuum. The ion gauge pressure set point is adjusted to $5x10^{-5}$ torr. Power to the turbomolecular pump pneumatic isolation valve, mass spectrometer, and hexapole rods is cut off if this pressure is exceeded. Supply resumes when high vacuum is reestablished.

3.3 Sample handling

The sample delivery system, shown in Figure 3.9, is constructed from 1/4" stainless steel and copper tubing. Connections are made with brass Swagelok fittings. Valves are brass on/off valves with Swagelok fittings (Nupro, JN). Copper tubing sections of the system are reserved for inert gases with the exception of some short upper Stark state relaxation experiments where CH_3F and CH_3Cl are used as the quenchers. Stainless steel reservoirs for both gaseous and liquid samples are manufactured in the Chemistry Department's Mechanical Workshop. Liquid samples are purified in the system by vacuum distillation.

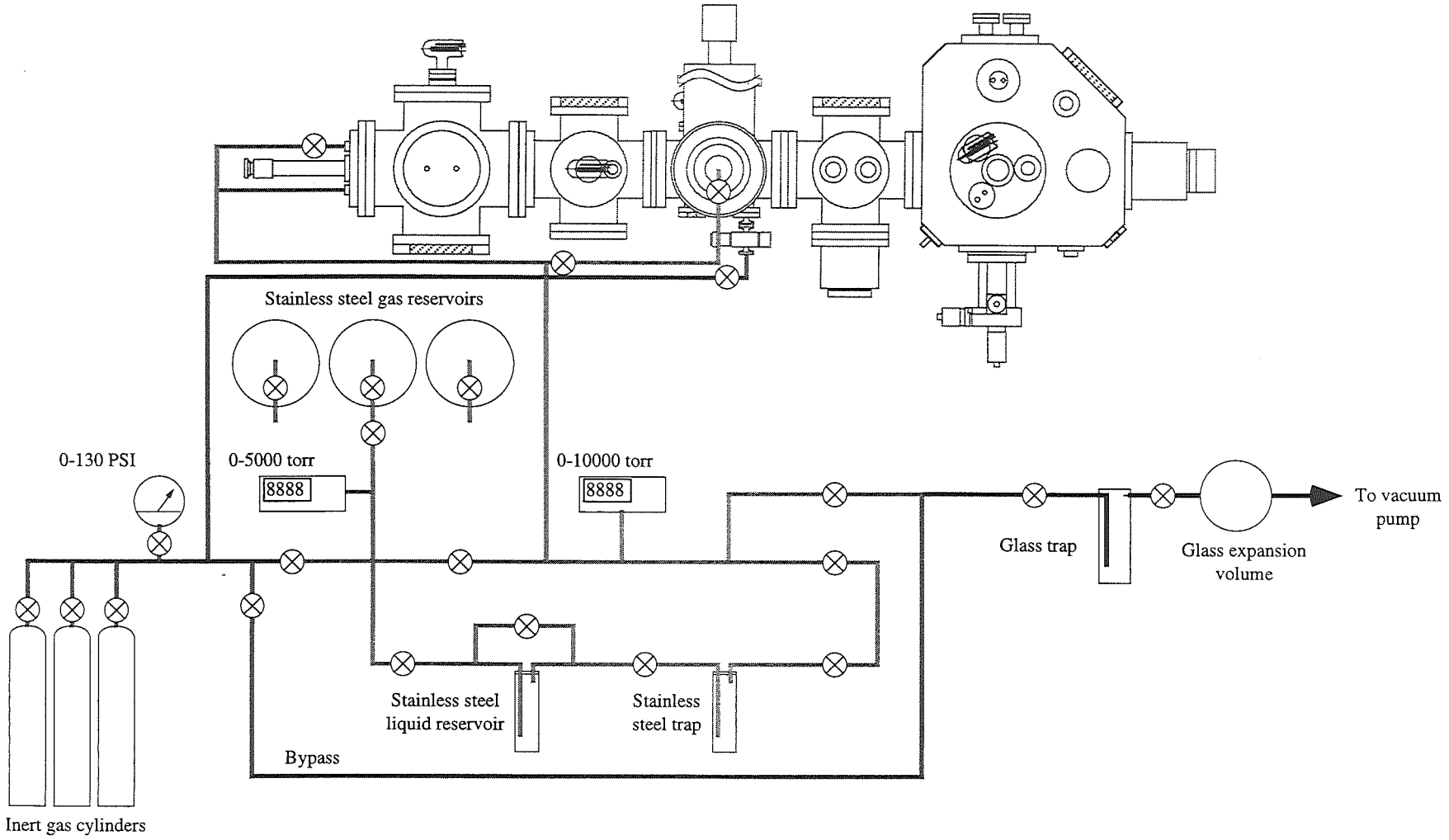

Figure 3.9 Sample delivery system. Copper (—) and stainless steel (—) tubing indicated.

Porous glass ceramic filters fitted in-line with the nozzle prevent liquid from blocking the valve opening. Table 3.1 provides details of the source, purity and storage of all samples. A 100 l/min Edwards, Speedivac ES-100 mechanical pump is connected to the system via a glass buffering volume. Pressure is monitored by 0-5000 torr and 0-10000 torr capacitance manometers (MKS Baratron, 122AA-05000BB and 221-AA-10000, respectively) connected to separate controllers (MKS, PDR-C-1C and PDR-C-1B, respectively). Additional pressure measurement is made with a face-dial 0-130 psi meter. The machine is vented with argon through a valve attached to the nozzle chamber (Figure 3.9). Overnight the turbomolecular pump is purged with nitrogen (also indicated). Two further gas lines, one to force liquid nitrogen into the machine's traps, and the other to pressurise the turbomolecular pump pneumatic gate valve, are attached to separate cylinders of dry nitrogen with 1/4" copper tubing and brass Swagelok fittings. Pumping of these lines is not required.

Sample	Purity (%)	Storage	Source
He	99.99	Cylinder	NZIG
Ne	99.95	Cylinder	Matheson
Ar	99.95	Cylinder	NZIG
Kr	99.95	Cylinder	BOC
Xe	99.99	Cylinder	BOC
H_2	'Industrial'	Cylinder	NZIG
SF_6	99.99	Cylinder	Fluorochem
CO_2	99	Cylinder	NZIG
N_2O	99.9	Cylinder	NZIG
N_2	99	Cylinder	NZIG
CH_3F	99.5+	Lecture bottle	Fluorochem
CH_3Cl	99.5+	Lecture bottle	Aldrich
CH_3Br	99	Cylinder	Aldrich
CCl_3H	'Spectroscopic'	Bottle	Mallinckrodt
CF_3Br	99	Cylinder	Wormald

Table 3.1 Sample details.

3.4 Supersonic beam source

A solenoid valve designed for molecular beam work (General Valve Corporation, model 9-181) is mounted in the nozzle chamber (Figure 3.10). The valve, or nozzle, has an aperture of 300 μm diameter sealed by a spring loaded teflon poppet. To improve supersonic beam formation in this experimental configuration the aperture is reduced to 70 μm diameter with a laser drilled molybdenum disc (JEOL, SVC). The disc is held in place over the existing aperture by a stainless steel face plate.

Gas from the sample handling system is fed to the nozzle through Swagelok/Cajon vacuum feedthroughs and 1/4" flexible stainless steel bellows (Cajon, 321-4-X-12). The bellows is sealed to the nozzle and feedthrough with brass Swagelok fittings. Electrical connections are made with soldered multi-strand copper wire covered with resin-free fibreglass sheath, through a three pin Amphenol vacuum feedthrough.

The nozzle is bolted to a carriage than can be translated along the principal machine axis with a calibrated linear motion feedthrough (Huntington Mechanical Laboratories, VF-156). Linear bearings along the carriage length run smoothly on two rods parallel to the principal axis. Aluminium extensions on the carriage allow the nozzle to be positioned as close as 1 mm to a skimmer which connects to the buffer chamber. The 8" flange on which all nozzle feedthroughs are mounted seals on a Viton 'o'-ring smeared with diffusion pump oil. A bolt screwed into the bottom of the flange secures it to a mount similar in design to the chamber translators described previously. Removal of the flange for maintenance and alignment is simple and rapid. Flakes of teflon from the nozzle poppet often block the molybdenum disc aperture and must be first loosened with sonication and then washed away in solvents.

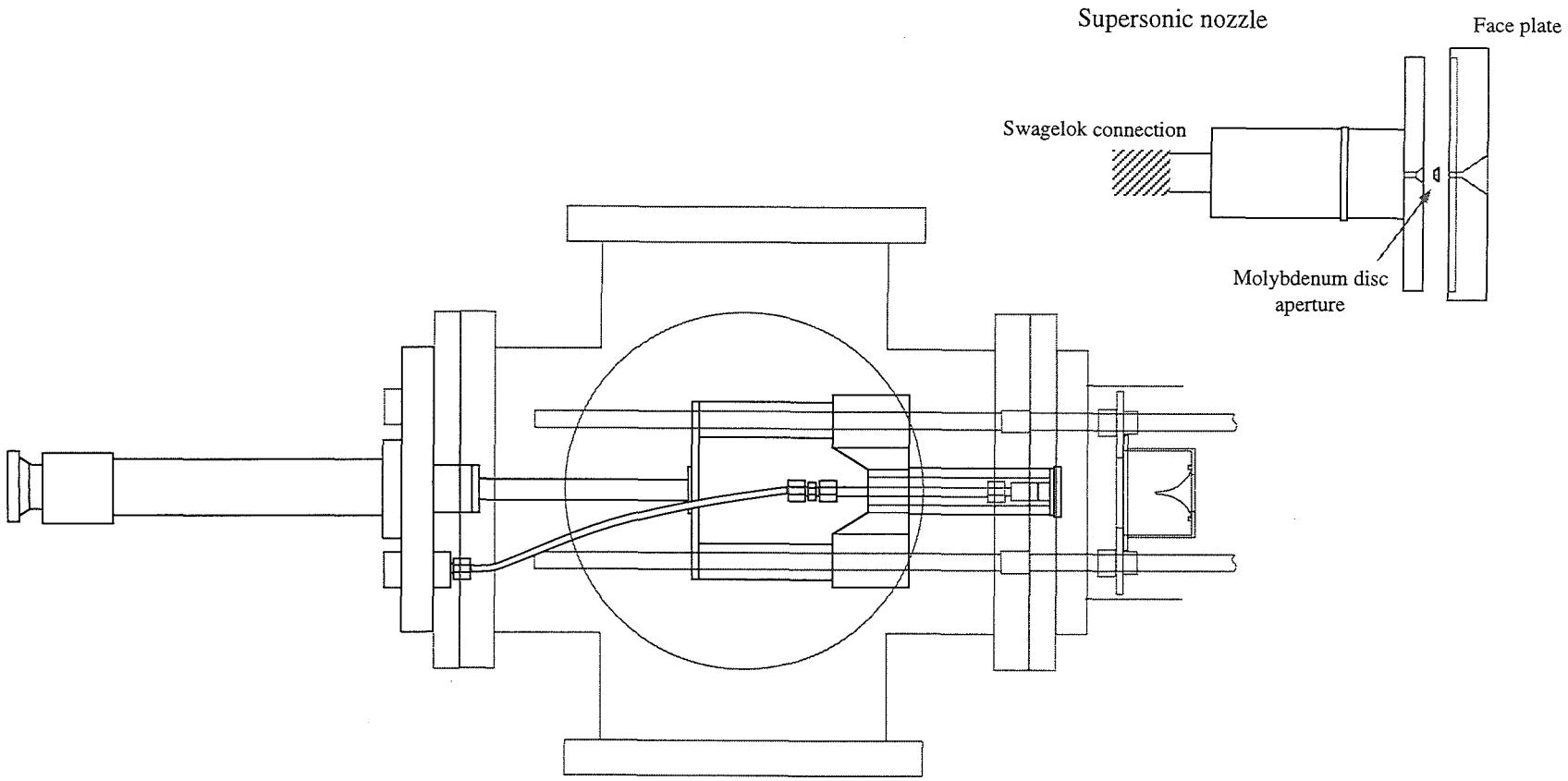

Figure 3.10 Supersonic nozzle assembly. Scale 1:5. Nozzle close up, scale 1:1.

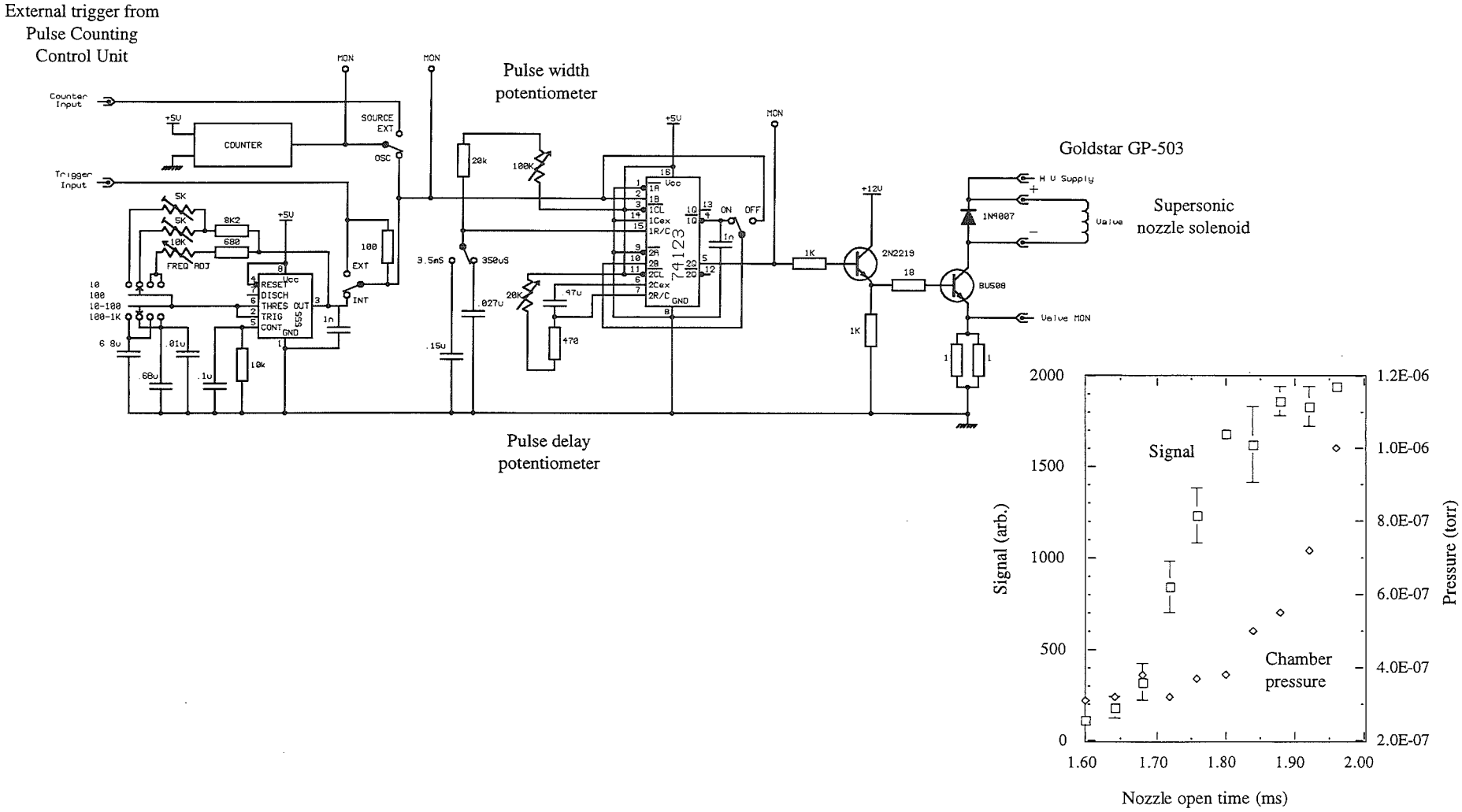

Figure 3.11 Beam Source Driver circuit (inset, effect of open time on signal).

The electrical pulse necessary to actuate the nozzle is supplied from a Beam Source Driver (BSD) constructed in the Chemistry Department's Electronics Workshop. Pulse length, height, frequency and delay may be adjusted with the BSD (Figure 3.11).

Nozzle operation frequency is selected from an internal or external trigger source. Usually the trigger is supplied externally from the Pulse Counting Control Unit at 10 Hz. Pulse width, or open time, is set with a 10-turn potentiometer between 200 μs and 2.2 ms. The delay feature is not used in this work and is set to the minimum of 0.2 ms. Figure 3.11 also illustrates the effect of nozzle open time on beam intensity and chamber pressure. Voltage is supplied from internal 12 V @ 1 A, 24 V @ 1 A or external power supplies (Goldstar 50 V @ 3 A, 5P-503). For optimum results the external supply is selected. Table 3.2 summarises the typical operating conditions of the nozzle.

Open time	1.2-1.4 ms
Voltage	37 V
Frequency	10 Hz
Delay	0.2 ms (minimum)
Nozzle-skimmer distance	17.5 mm

Table 3.2 Nozzle operating conditions.

3.5 Supersonic beam alignment

Two 12 mm diameter stainless steel rods (Figure 3.12) running parallel to each other and equispaced about the machine axis provide the plane of reference to which a number of vacuum components are aligned. The rods, held in place by flanges at both ends of the buffer chamber, extend into the nozzle and first hexapole chambers as indicated in the figure. Two stainless steel flanges are mounted on the rods and one positioned in each of the chamber arms. The flanges minimise conductance of gas from

the nozzle chamber through to the hexapole and scattering chambers and also provide a surface to which beam skimmers may be attached. A 1 mm diameter electroformed nickel skimmer (Beam Dynamics) is clamped against a top hat mounted on the first flange. The skimmer tip is positioned approximately 2 mm away from the supersonic nozzle when at full extension (see previous section). A second skimmer, of aluminium and 1.5 mm diameter (Chemistry Department's Mechanical Workshop), is attached to the second flange with a similar top hat and placed close to the hexapole rods. Both skimmers are centred on their top hats using a lathe.

To align vacuum components the nozzle is replaced with a He-Ne laser (Applied Laser Systems, 670 nm 5 mW). Lining up the laser beam with the first skimmer and the centre of the scattering chamber gives the reference axis. The second skimmer is centred on this axis by loosening the top hat mounting screws and adjusting its position.

A flexible spring hangs down into the buffer chamber and is attached from a vernier feedthrough on the buffer chambers top flange. Pressed into the spring is a steel rod with a 1.5 mm diameter ball on its tapered end. The rod and its ball slide through a tube welded into the second top hat. Turning the vernier feedthrough allows positioning of the ball so that it intersects the molecular beam/hexapole axis. For this reason the ball is called a beam stop and its use is described in §2.4.

3.6 Hexapole

The 10 mm diameter hexapole rods are centreless ground stainless steel, 83.3 cm in length. They are held apart on an inscribed radius of 5.88 mm by two ceramic mounts, Figure 3.13. Earlier experiments with different mounts had an inscribed radius of 7.50 mm necessitating the use of higher voltages to achieve the same field strength.

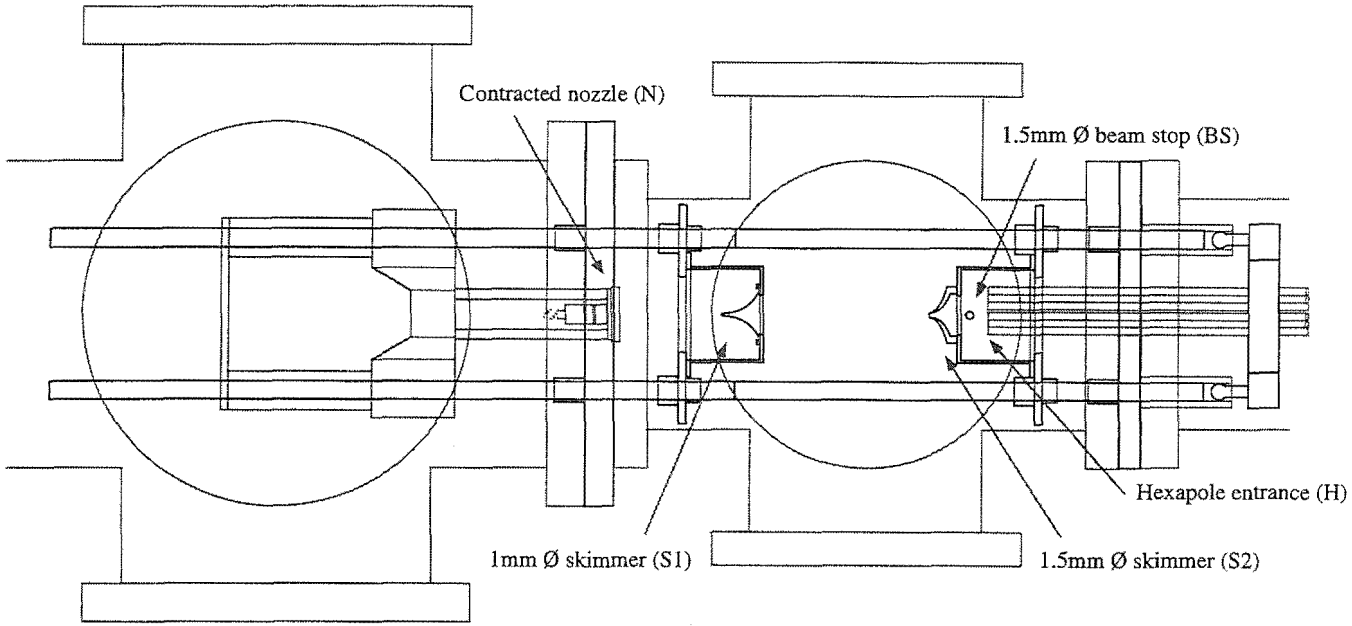

(mm)	N	S1	S2	BS	H
N	-	72	209	235	250
S1		-	137	163	178
S2			-	26	41
BS				-	15
H					-

Figure 3.12 Alignment rods, skimmers and beam stop. Scale 1:5.

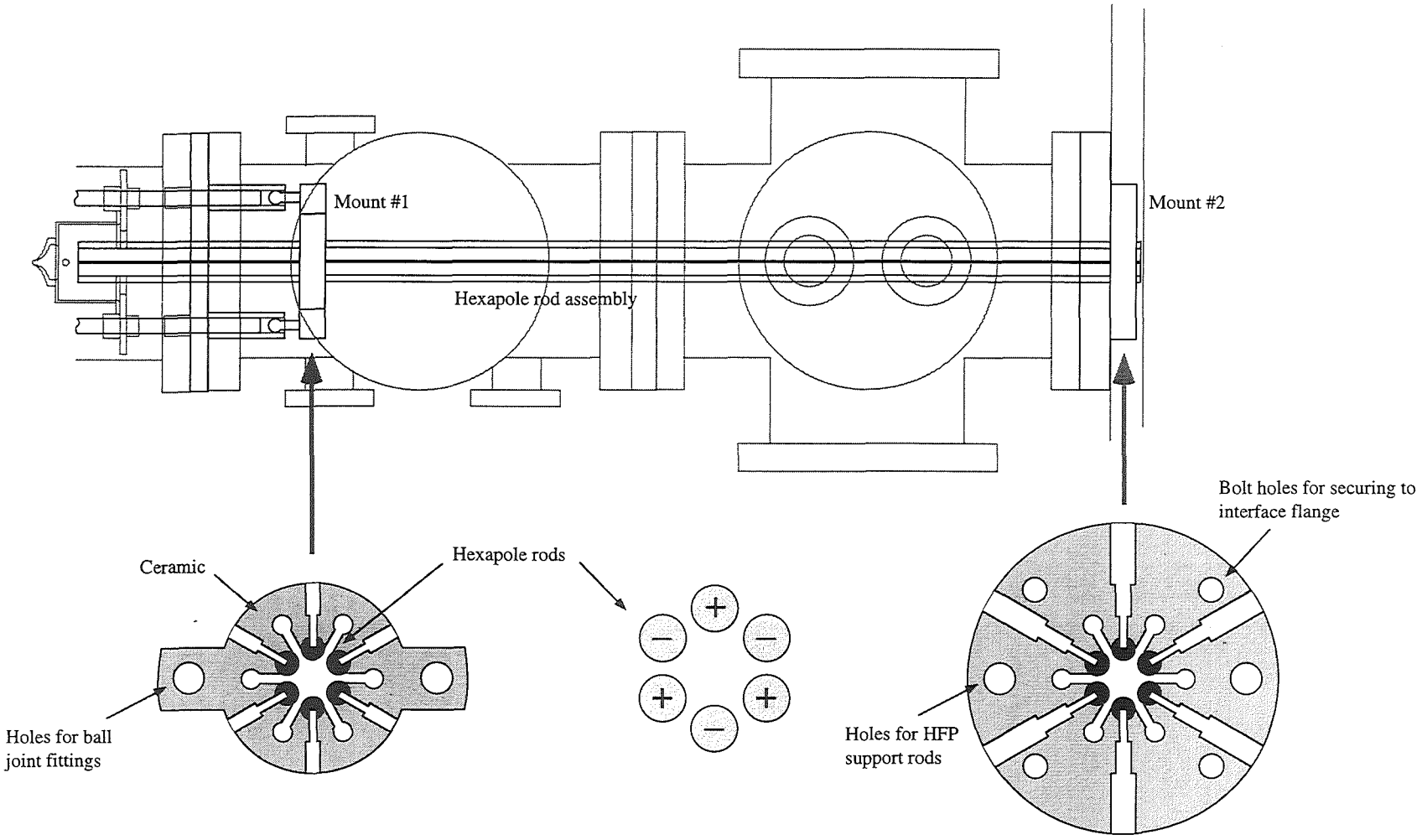

Figure 3.13 Hexapole (Scale 1:5) and ceramic mounts (Scale 1:2.5).

Each rod is held against the mounts by two screws. Surface distance between the rods is maximised by machined slots in the ceramic.

Two alignment rods, described in the previous section, extend into the first hexapole chamber. On to the end of each rod is pressed a metal sleeve. The ceramic mount closest to the buffer chamber has two ball joints which are pushed into these sleeves. Alignment of the hexapole is achieved by pivoting the assembly on these ball joints while the He-Ne line-up laser is operating. Once centred the second ceramic mount is bolted against an interface flange between the second hexapole and scattering chambers.

Electrical connection to each hexapole rod is made by a short length of 3 mm diameter copper rod pressed into a reamed blind hole situated halfway along the hexapole rod. The copper rods from like-biased 'poles' are soldered to a single copper strip and then to a length of copper braid. Both braids are soldered to high voltage ceramic feedthroughs on the top flange of the second hexapole chamber.

The 1.5 mm diameter skimmer forms the entrance aperture to the hexapole assembly and the exit aperture was either a fixed 8 mm diameter orifice for electron impact experiments or a variable shutter for cross-section experiments. Transmission of the on-axis $M = 0$ symmetric-top molecules is prevented by centring the beam stop described in the previous section. Two different exit apertures are used in this work. For the electron impact ionisation asymmetry studies a plate with 8 mm diameter hole is fixed to the homogeneous field plate assembly while for the upper Stark state relaxation experiments an adjustable iris (diameter > 1 mm) is mounted on a 10 mm deep stainless steel top hat pressed into the 8" flange opening of the scattering chamber.

Voltages of up to 30 kV are applied to the hexapole rods by two oppositely biased computer controlled high voltage power supplies (Glassman, EH-series 0-30 kV). In practice the highest voltage used is ±7 kV above which discharge across the ceramic

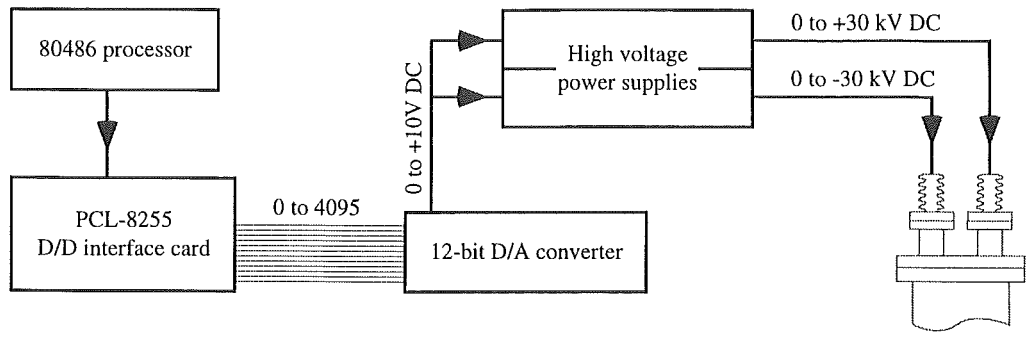

Figure 3.14 Hexapole computer interface.

mount surface occurs. A maximum voltage of ±13 kV was used for experiments with larger hexapole rod spacing, though the field strength between rods was the same in each case. Current is limited on each supply to 0.01 mA to prevent damage in the event of a discharge. Both high voltage supplies are connected to a single 12-bit 10 V digital-to-analog converter which in turn is linked to an IBM PC-compatible 80486 processor by a PCL-8255 digital-to-digital interface card. Computer instructions set the hexapole voltage during experiments with a precision of better than ±7 V. Figure 3.14 illustrates the interface configuration.

3.7 Electron beam source

A beam of near-monochromatic electrons is produced by a custom designed and fabricated electron source. Electron energy is variable between 30 and 300 eV. Figure 3.15 illustrates elements of the 'gun' and the electron emission source.

The emission source is a 12.7 mm length of 0.007" rhenium wire coated at the tip with a mixture of 90.1% $BaZrO_3$, 5.6% $BaCO_3$ and 4.3% $SrCO_3$ to reduce the metal work function. This wire, or filament, is looped so that the tip pokes through the Pierce element aperture. A negatively biased current of greater than 2 A @ 12 V heats the filament to the point where electrons are emitted from the metal surface and accelerated

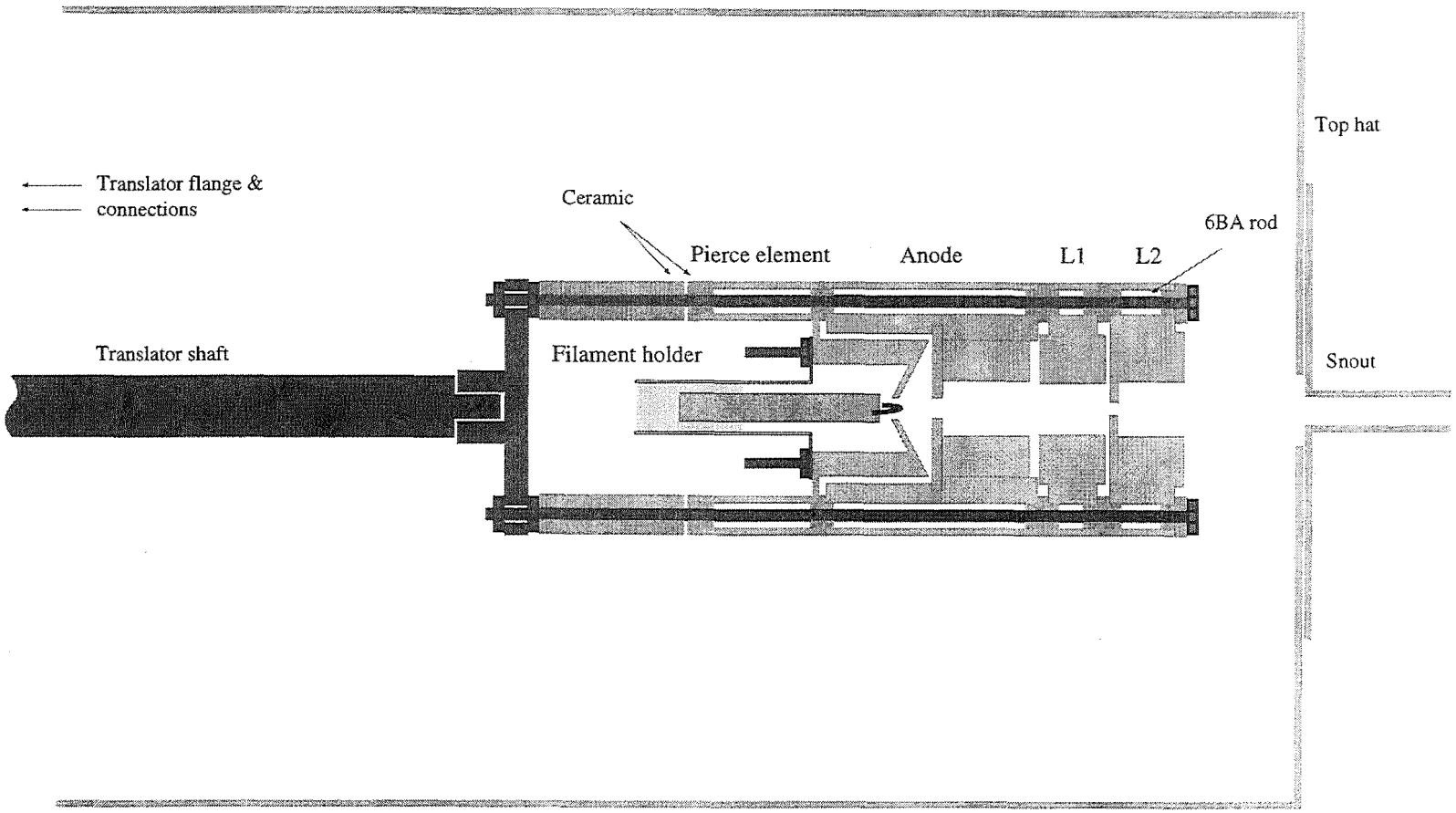

Figure 3.15 Electron gun. Scale 1:1.

toward the anode aperture. The anode, L1 and L2 elements act together as a modified Einzel lens to produce a focused electron beam. Table 3.3 summarises the electron source settings and resulting beam intensity for this work.

EE (eV)	Pierce (V)	Anode (V)	L1 (V)	L2 (V)	Flux ($\mu A\ mm^{-2}$)
100	-76	152	-61	139	0.15
150	-123	47	-110	145	0.31
200	-174	105	-135	171	0.34
240	-205	40	-200	197	1.0
300	-211	205	-151	136	1.0

Table 3.3 Electron gun settings employed for various electron energies (EE).

Four isolated 6 BA rods hold the electron gun elements together. These rods are fastened to a stainless steel plate which in turn is fixed to the shaft of an *xyz*-translator (Huntington Laboratories, PM-600). The electron and molecular beams are intersected at right angles by adjusting the translator and monitoring beam ion signal. Electrical connections to each element are single-core silver wire insulated with glass ceramic rod. Leads are attached to an 8-pin feedthrough on the translator flange by dual-screw connectors. A large snouted top hat (Figure 3.15) surrounds the gun, its purpose being to terminate electric field lines of the gun and minimise poisoning of the filament by backstreaming pump oil. Two 1 1/2" holes in the top hat placed well back from the homogeneous field region allow for pumping of the top hat interior.

A Faraday cup is mounted opposite the gun, on the other side of the homogeneous field plates, to collect the electron beam. In separate experiments the large top hat and Faraday cup are removed and a concentric ring collector (Figure 3.16) fabricated from machinable glass ceramic (Corning, Macor) and brass collector rings placed 75.2 mm away from the end of gun element L2. Optimum Einzel lens settings are determined in

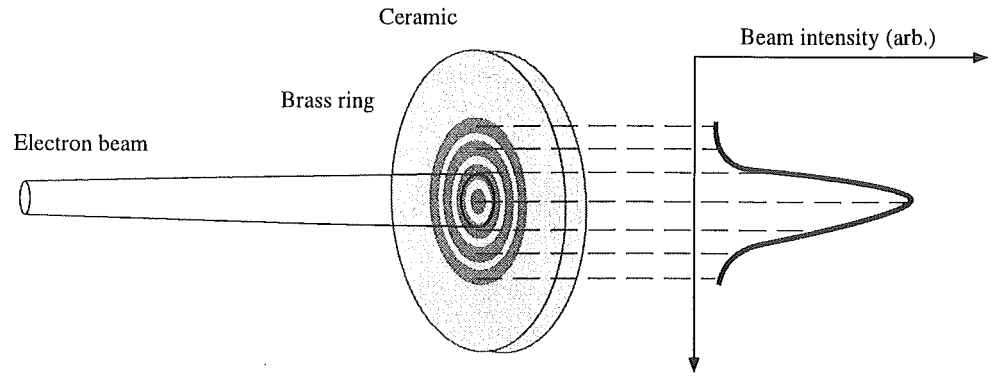

Figure 3.16 Concentric ring electron collector.

this configuration. The beam width at half height is approximately 3 mm and typical flux at the beam core is 10^{-6} A mm^{-2}.

3.8 Detectors

3.8.1 Amptektron thermal ion detector

Ions formed by the intersecting electron and molecular beams are detected by an Amptek Inc., Amptektron MD-501L thermal positive ion detector. The Amptektron unit is housed in a metal can 83 x 57 x 19 mm in the vacuum chamber and consists of a Channeltron electron multiplier (CEM), charge sensitive amplifier discriminator and output driver (Figure 3.17). A charged particle striking the CEM surface results in a cascade of electrons accelerating down the CEM length, these electron bursts being collected by the amplifier discriminator, and then converted to a 5 V 220 ns wide pulse at pin B. This signal is directed to external pulse counting circuits.

The Amptektron is mounted on the shaft of a rotary motion feedthrough (Huntington, PR-275-M) so that the entrance aperture (3.58 mm diameter) is on-axis with the molecular beam and 25 mm further downstream than the intersecting electron beam,

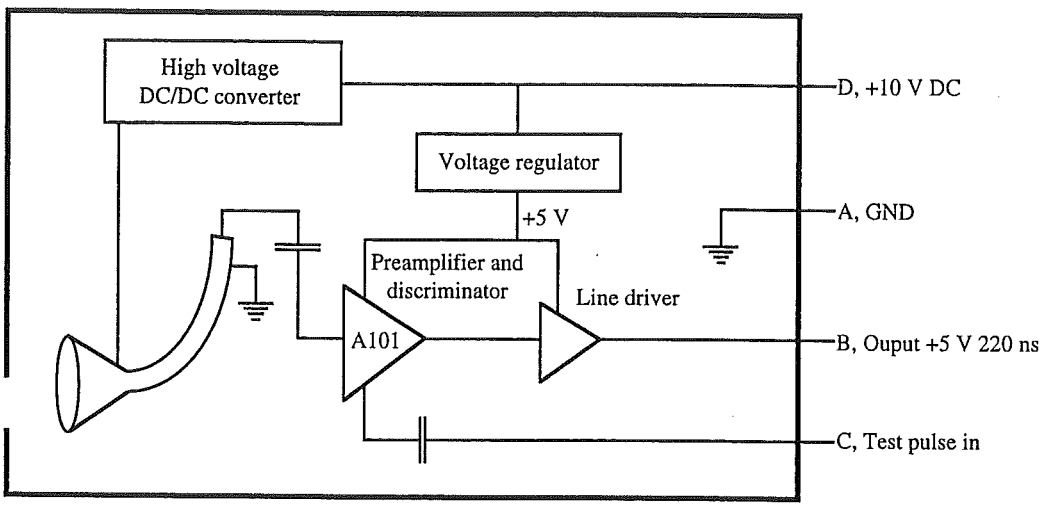

Figure 3.17 Amptektron schematic.

Figure 3.18. Rotation of the Amptektron in 1.8° steps is controlled by computer instructions to the stepping motor driver unit (§3.10.1). A typical argon beam profile obtained by stepping the Amptektron is shown in Figure 3.18.

Initially configured with +400 V on the CEM cone the Amptektron output signal from ionised molecular beam species was too low for the electron impact ionisation asymmetry experiments. Signal levels are now adequate after factory modification for low energy particle detection with a cone voltage of +3000 V.

Reducing the acceptance angle of ions into the Amptektron entrance aperture by addition of a collimating plate greatly favours detection of ions produced from the highly-directed molecular beam (Figure 3.18). This collimation provides one other condition which is crucial to the electron impact asymmetry experiments - an essentially field free region in front of the detector.

Vacuum cables are silver wire protected with resin-free fibre-glass sheathing. The output and earth leads are twisted together with an earthed braid covering the twisted

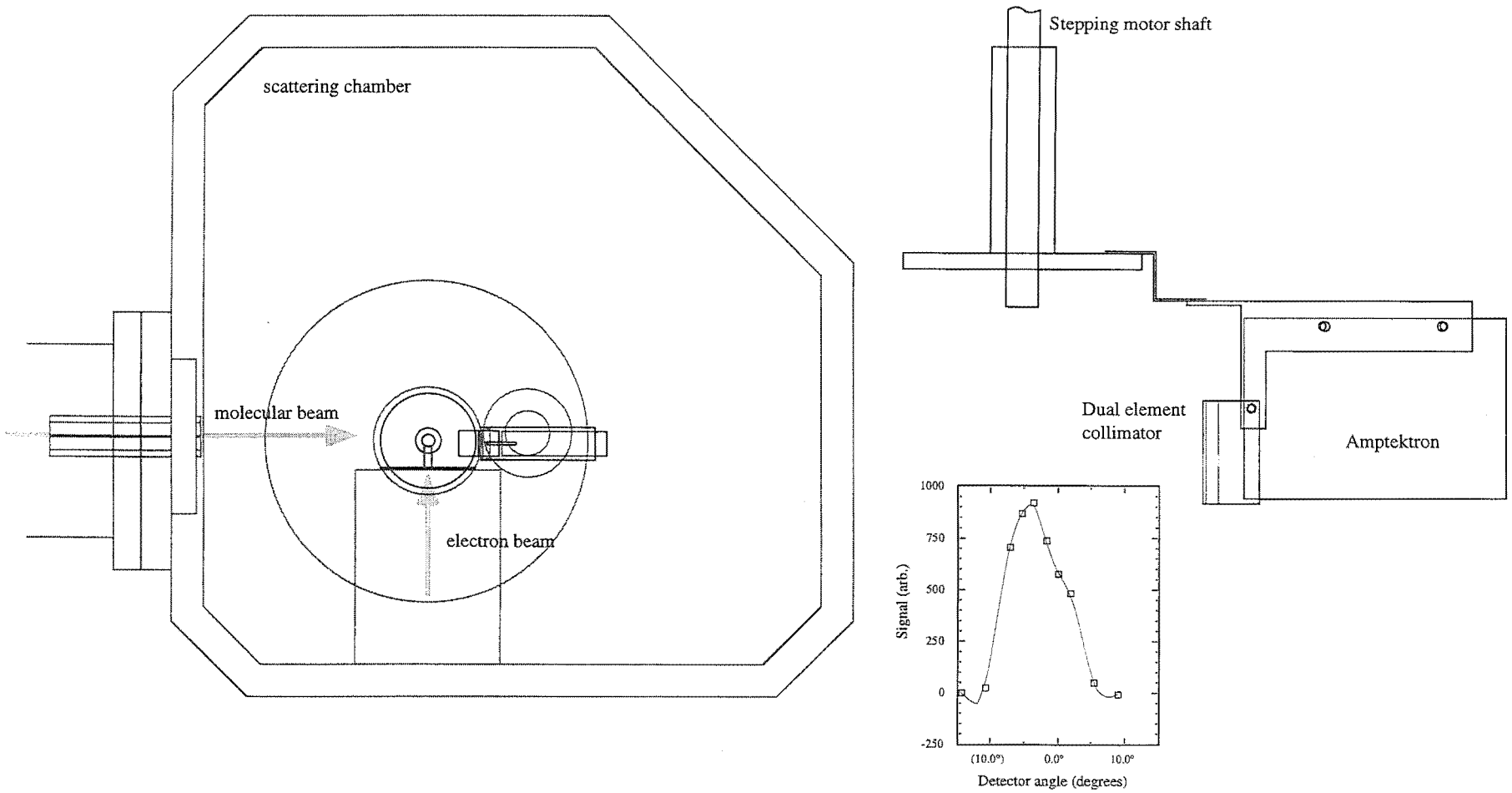

Figure 3.18 Amptektron low energy particle detector. Scale 1:5. Side on view, scale 1:2. Beam profile.

pair. Cables are connected to an 8-pin vacuum feedthrough on the scattering chamber lid. Power to the Amptektron is supplied from an ultra-stable 10 V DC power supply constructed in the Chemistry Department's Electronics Workshop. Output pulses from the Amptektron are processed and counted by the Pulse Counting Control Unit.

The sensitivity of the Amptektron to charged particles, specifically the Channeltron particle multiplier, is proportional to their velocity. Heavier, slower species are less efficiently detected and in the context of symmetric-top molecules only CH_3Cl and CH_3F were suitable for use with the Amptektron. Studies of higher mass species requires additional discrimination against background gas and in this work a mass spectrometer is used. The electron impact asymmetry results are collected with either the Amptektron or an on-axis quadrupole mass filter.

3.8.2 Quadrupole mass filter

A Vacuum Generators SXP300 0-300 m/z unit quadrupole mass spectrometer is mounted on-axis to the molecular beam (Figure 3.19). An ion source is attached in front of the quadrupole filter and behind, in the usual off-axis configuration, is a Channeltron electron multiplier (CEM) biased for positive ion detection. Output from the CEM is measured either as an analog signal or as a series of current pulses - the only difference being the processing electronics used. Analog signal is directed into the SXP300 analog amplifier via a 2 MHz notch filter (to remove RF noise). For pulse counting measurements the current pulses are passed to an Extranuclear Laboratories pulse counting preamplifier (model #032-3) and then to the Pulse Counting Control Unit.

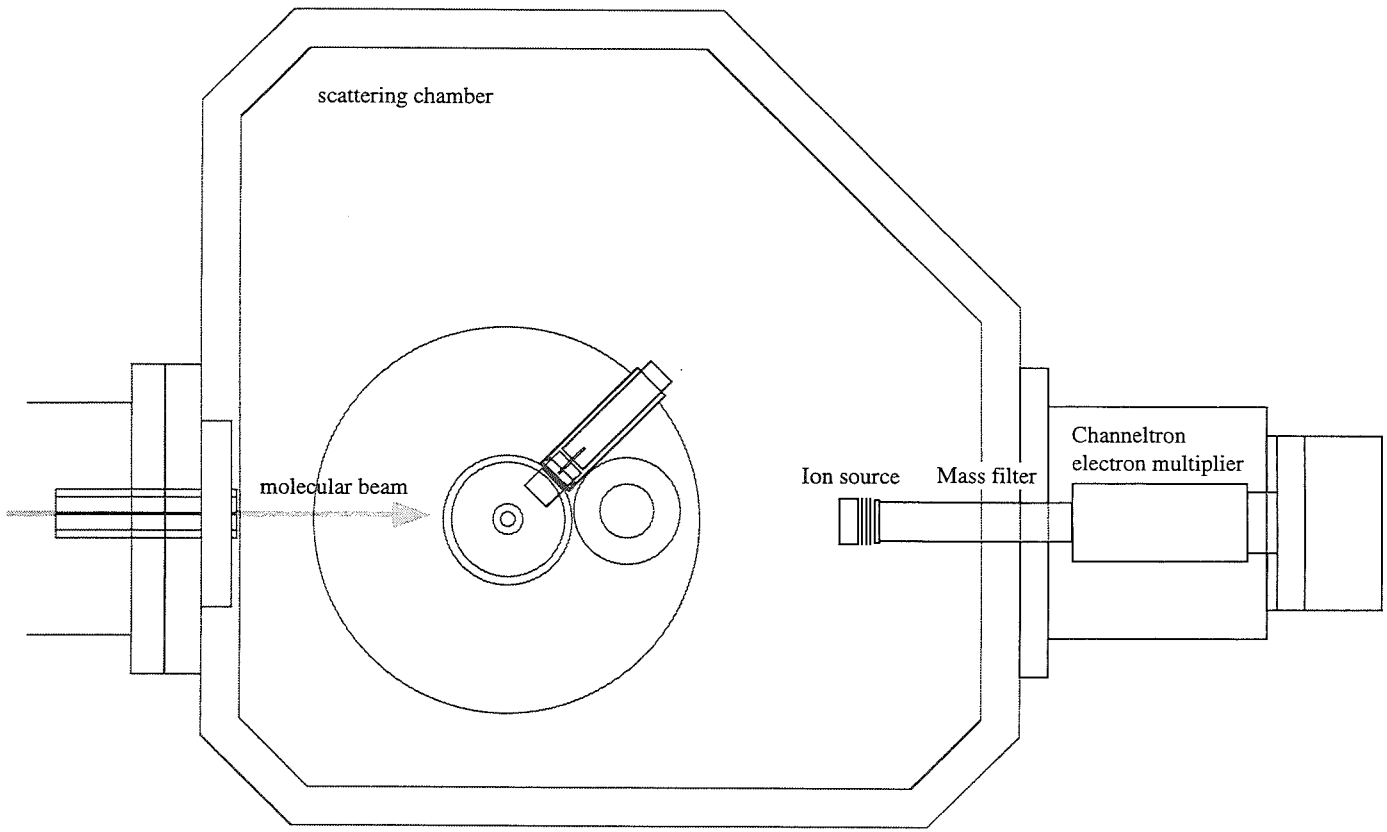

Figure 3.19 Quadrupole mass filter and ion source. Scale 1:5.

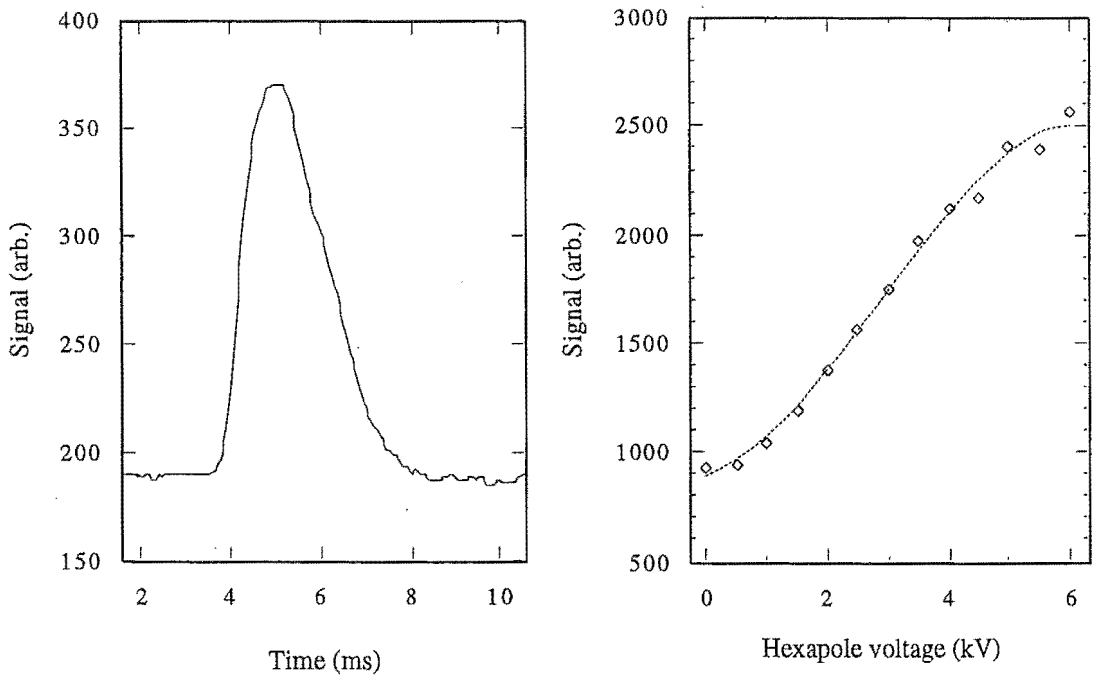

Figure 3.20 Data acquired with the mass spectrometer. On the left, an arrival time distribution for argon, and the other, a hexapole transmission curve for methyl chloride.

The quadrupole is a powerful diagnostic tool providing measurements of the supersonic molecular beam profile and the beam focusing effect of the hexapole (Figure 3.20). Often the detector is used to assess whether the nozzle valve is blocked. The Amptektron unit, described previously, is easily rotated off-axis to expose the quadrupole to the beam. Settings for the mass spectrometer are listed in Table 3.4.

Electron energy	70 eV
Ion energy	16.2 eV
Emission	$5x10^{-5}$ A
CEM cone voltage	-2.1 kV

Table 3.4 Mass spectrometer settings.

The mass spectrometer is also used to investigate electron impact ionisation asymmetry for species heavier than CH_3Cl and the orientation dependence of fragment ion signals.

For these experiments the Amptektron is removed and the filter mounted close to the homogeneous field plate assembly. The commercial ion source is replaced with an electrostatic ion lens purpose designed and fabricated to focus ions formed by the intersecting molecular and electron beams (refer to Figure 3.21 which also shows simulated ion trajectories with and without an orienting electric field). Constructed from stainless steel plates, the front lens plate is sandblasted and coated with Aqua-dag colloidal graphite to minimise electron scattering. Leads are single-core copper wire insulated with resin-free fibreglass sheath. Each lead is soldered to a lens plate and at the other end to a 8-pin vacuum feedthrough on the scattering chamber mid-section. Voltages to the lens elements are supplied from a custom power supply bank containing four ±200 V DC power supplies.

Successive particle multiplier failures prevented the SXP300s' use for some of the electron impact studies. For these cases the mass spectrometer was mounted in its original configuration with the commercial ion source and the Amptektron unit installed in its place.

3.8.3 Channeltron electron multiplier and ion source

A Channeltron electron multiplier (CEM) coupled with the SXP300 mass spectrometer ion source (Figure 3.22) measures the molecular beam intensity for upper Stark state relaxation experiments.

The multiplier is mounted under a ceramic block by soldered connections and placed directly behind the ion source. Both CEM mount and ion source are bolted to a stainless steel plate which in turn is attached to the Huntington Laboratories *xyz*-translator otherwise used for positioning of the electron beam source. The detector is centred on the molecular beam axis by adjusting the translator settings.

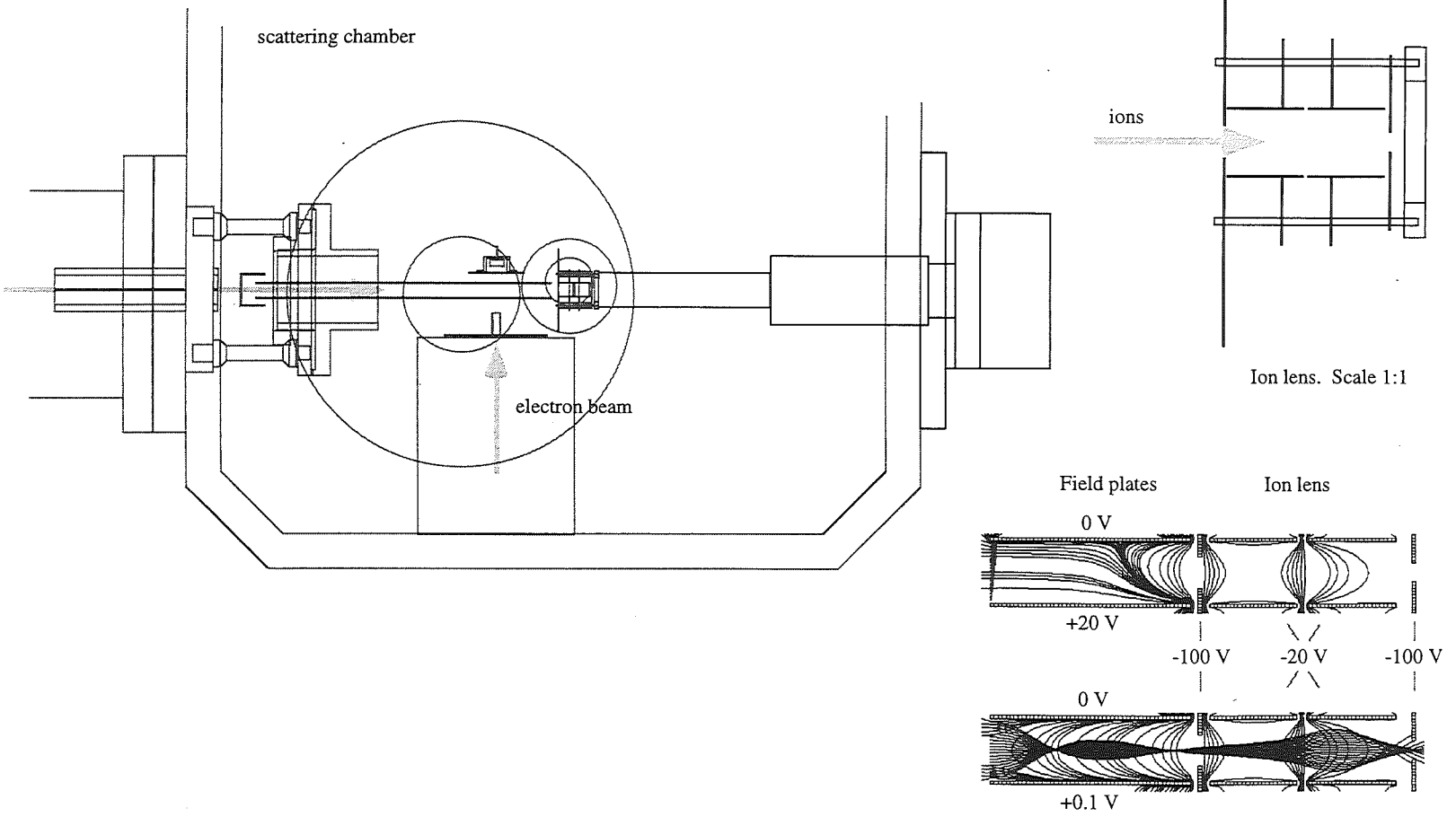

Figure 3.21 Mass filter with ion lens. Scale 1:5.

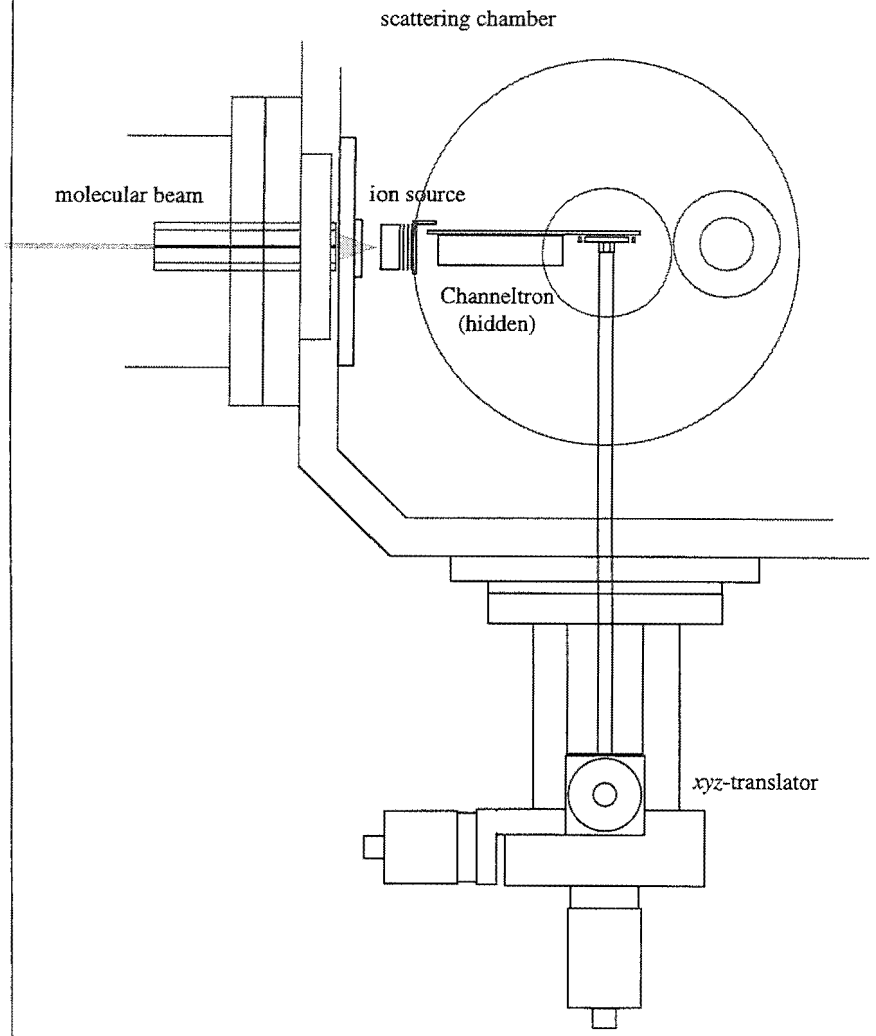

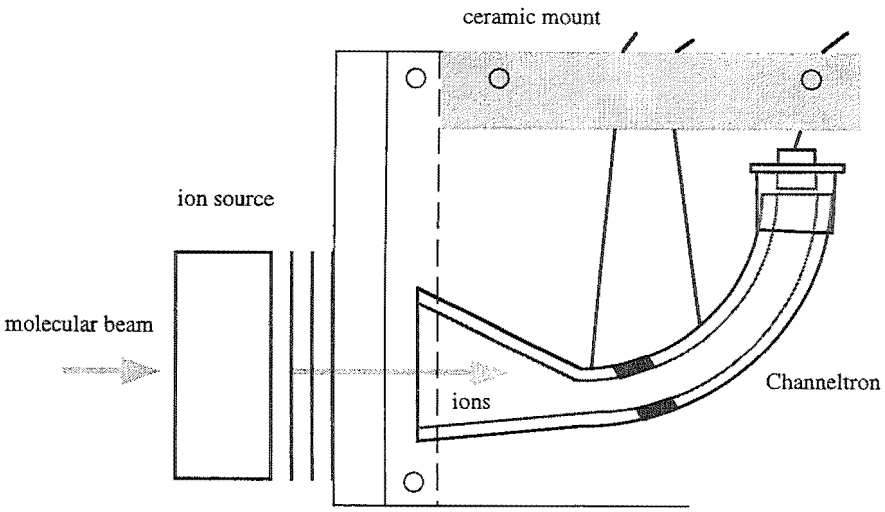

Side view. Scale 1:1.

Figure 3.22 Channeltron electron multiplier and ion source. Scale 1:5.

Leads from the ion source are fibre-glass sheathed (Jones Stroud Insulations, Vidaflex L124) single core copper wire connected to the mass spectrometer interface flange. This allows the ion source to be controlled from the SXP300 electronics unit.

High voltage and earth leads for the CEM are soldered to the nickel tabs supplied with the Channeltron and at the other end to the vacuum feedthroughs. The signal lead is single core silver wire soldered to the CEM collector, sheathed with fibreglass, twisted together with a sheathed earth wire, and finally surrounded by an earthed braid. Both the signal and high voltage leads are connected to BNC vacuum feedthroughs while the earth is connected to a standard 8-pin feedthrough.

Ion source current and voltage and CEM high voltage are supplied from the SXP300 control unit. Table 3.5 details CEM and ion source settings for this work. Output pulses from the CEM are fed to the Extranuclear Laboratories charge sensitive preamplifier and then counted with the Pulse Counting Control Unit.

Electron energy	50 eV
Emission	5×10^{-5} A
Ion energy	16.2 V
Focus plate	-94 V
CEM cone voltage	-2.1 kV

Table 3.5 Ion source and channeltron settings.

3.9 Homogeneous field plates

The homogeneous field plates (HFPs) are central to the electron impact ionisation asymmetry experiments, providing the electric field about which state-selected symmetric top molecules are oriented. The design of the HFPs also facilitate the ionisation and detection of oriented molecules (refer to §5.2).

The HFPs are made up of two 1 mm thick stainless steel sheet plates 185 x 40 mm held 10 mm apart at each corner by tapped 5 mm diameter perspex rod spacers. At the hexapole end an open-ended box carries the hexapole exit aperture which is electrically isolated from both plates (Figure 3.23). The exit aperture is an 8 mm diameter orifice aligned on-axis with the molecular beam using a He-Ne laser (§3.5). Both HFPs and the exit aperture are held in a perspex mount fixed to the scattering chamber wall by two stainless steel rod spacers (Figure 3.23). A 10 mm diameter hole is drilled through each HFP allowing the electron beam to intersect the molecular beam and then exit the field region with minimal scattering off the plate surfaces. By convention the plates are named 'near' and 'far' with respect to the electron beam source. An earthed 20 mm long snout with 5 mm internal diameter is fixed to the end of the electron gun top hat (Figure 3.15). This is positioned so that the end of the snout is slightly back from the near plate aperture and centred on it. This snout minimises the interaction of the electron beam with the near HFP which is held at either ground potential or ±20 V. A brass Faraday cup is mounted on a stainless steel plate behind the far HFP. The cup is centred on the electron beam to facilitate measurement of beam flux.

Shim plates of the same length as the HFPs are mounted above and below to shield the homogeneous field region from stray electric fields. Above the top shim shield is a large copper plate attached to a liquid nitrogen cold finger. Cryogenic pumping reduces the local background gas pressure and this improves the experimental signal-to-noise ratio.

All metal surfaces described in this section (excluding the cold plate) are sandblasted and coated with colloidal graphite (Aqua-dag) to minimise electron scattering.

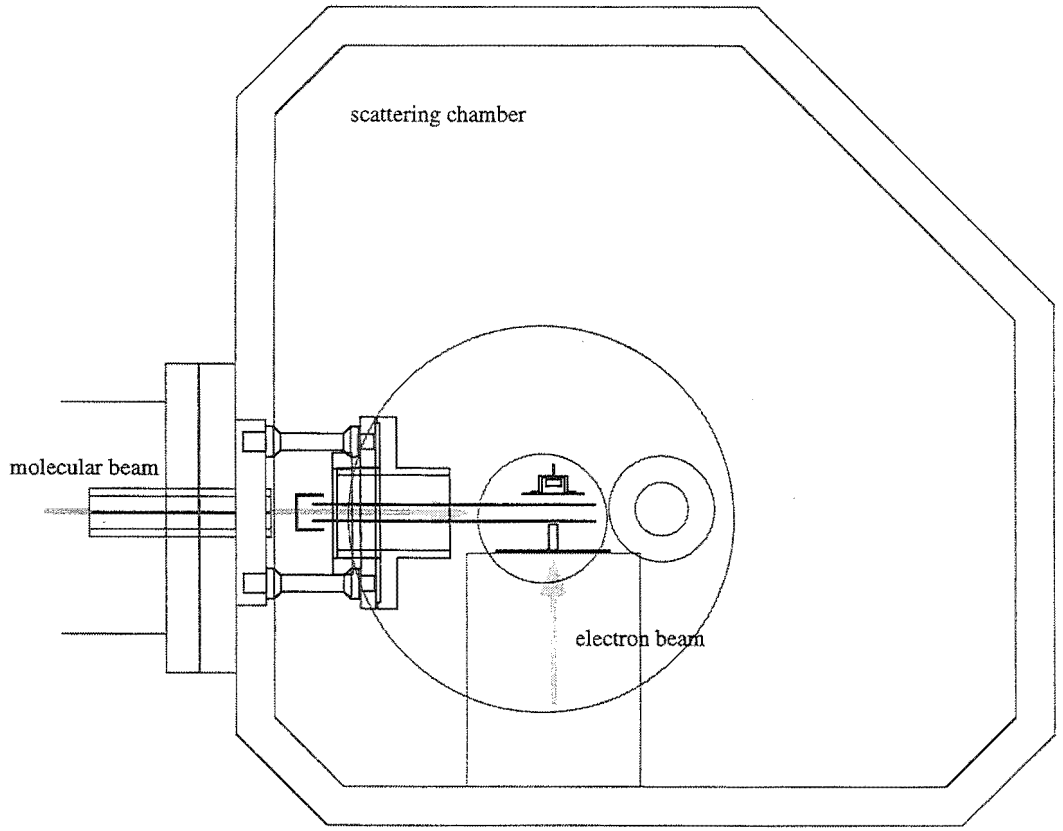

Figure 3.23 Homogeneous field plate assembly. Scale 1:5. Electric field shielding and the copper cold surface are not shown in order to improve clarity.

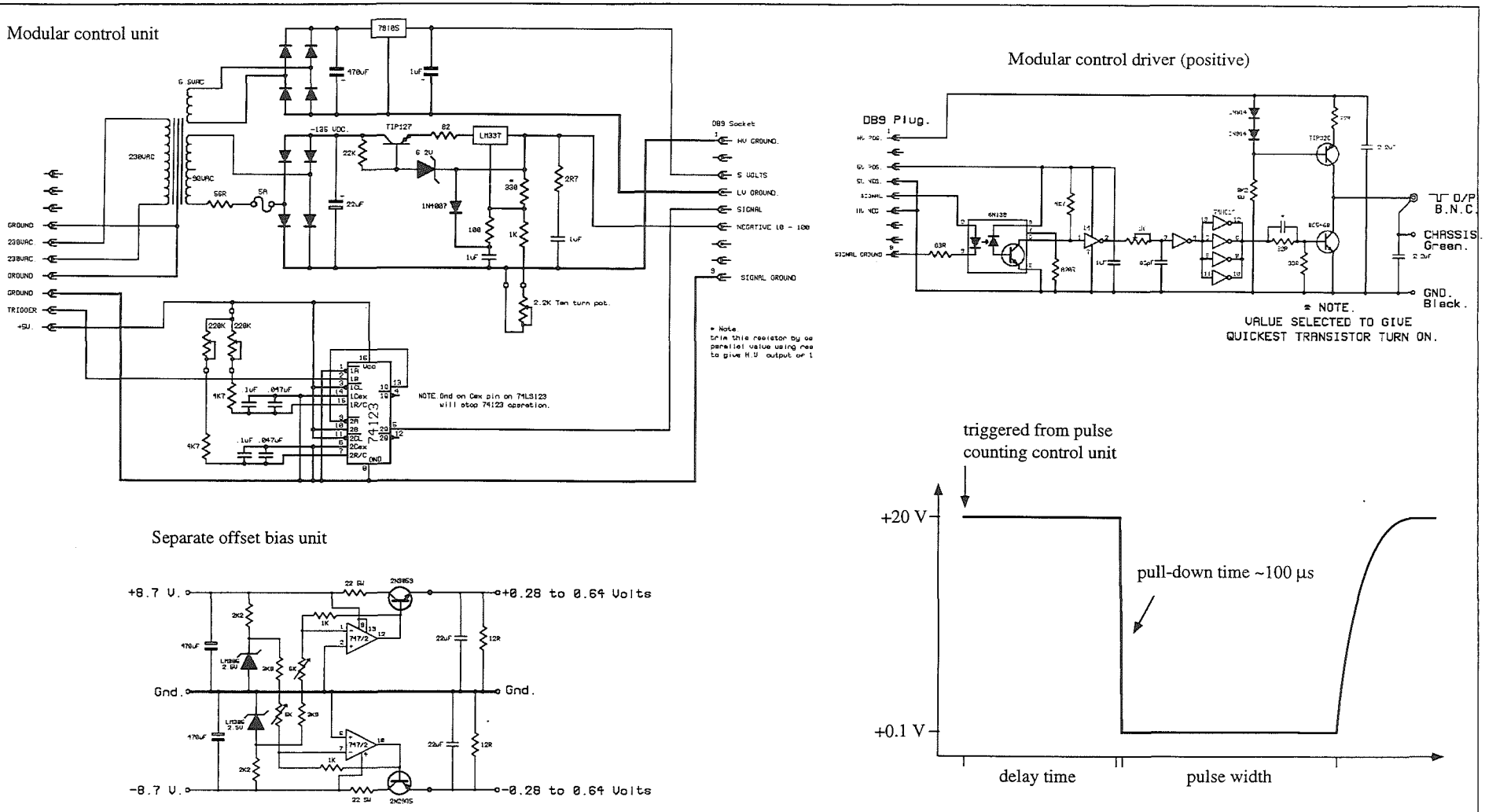

Figure 3.24 Homogeneous field plate pulsing unit circuits. Inset, HFPPU output.

Electrical connections to the HFPs, shields and aperture plate are made by press-on connectors. Each 'male' connector is soldered to a single-core copper wire protected by resin-free fibreglass sheath. The Faraday cup connection is a lock-nut type and the wire is single core silver sheathed in a similar manner. Shield, aperture and Faraday cup leads are attached by double-screw type connectors to an 8-pin feedthrough on the side of the scattering chamber. The HFP leads are attached to BNC feedthroughs by press-on connectors.

The homogeneous field must be switched off rapidly to avoid deflection of ionised beam molecules, as explained in §5.2. A plate pulsing unit (HFPPU) designed and constructed by the Chemistry Department's Electronics Workshop is connected to one of the HFPs and the other plate earthed (Figure 3.24). The HFPPU generates a 0-100 V variable width ground-going pulse with a fall time of approximately 0.1 ms. Triggered by the Pulse Counting Control Unit the pulse is delayed so that a large portion of the molecular beam is within the HFP region before the field collapses. Typically set to 20 V the plate voltage is pulled down to a value close to 0V by a separate offset bias unit. After approximately 10 ms the voltage supply is released and returns the plate to 20 V.

The HFPPU unit houses six independent pulsing supplies, three positive and three negatively biased. Only one supply is used in these experiments. Field direction between the plates is reversed by swapping the HFPPU connection to the opposite field plate. Figure 3.25 illustrates the effect of voltage pulsing on the ion signal generated from electron impact ionisation of background gas in the scattering chamber.

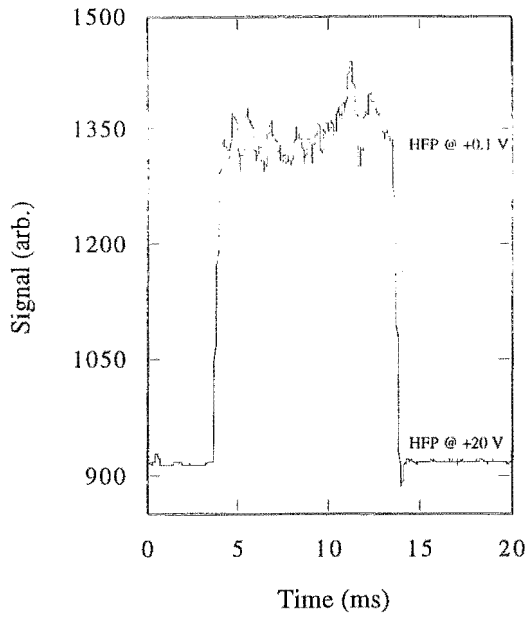

Figure 3.25 Effect of HFPPU on the background ion signal.

3.10 Computer interfacing

3.10.1 Stepping motor

Two stepping motors are used in these experiments - a Huntington PR-275-M motorised rotary motion feedthrough for positioning the Amptektron detector and a Howard Industries 1-19-3407 motor coupled to a Leybold Heraeus variable leak valve. Both motors are controlled by an IBM PC-compatible 80486 processor (Figure 3.26). Program commands to the PCL-7388 lab card direct pulse and direction signals to the driver unit (Crystalap, STD-206). Operating at 240 V / 50 Hz AC the STD-206 supplies a constant 0.6 A to the stepping motor coils. The Huntington motor rated for 8 V @ 0.5 A tolerates this current while the Howard Industries motor rated for 12 V @ 0.3 A overheats. To allow continuous operation of the variable leak valve during upper Stark state relaxation experiments power to the STD-206 is reduced to 150 V AC by a Variac. Computer interface routines are detailed in Appendix 1.

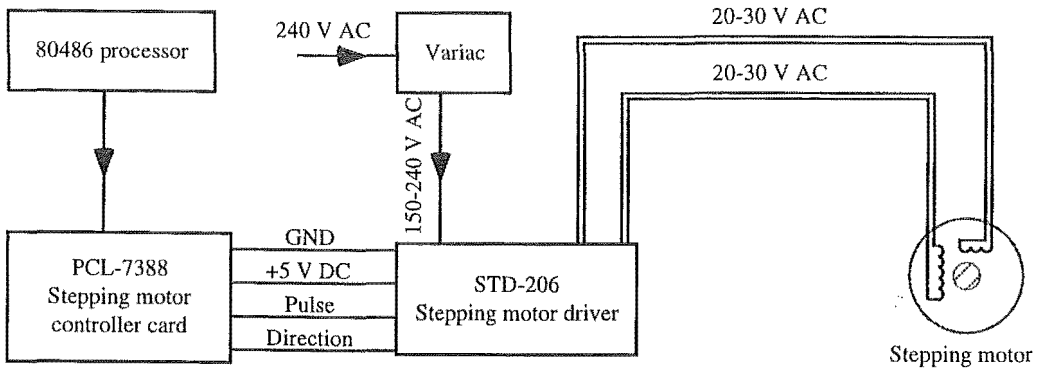

Figure 3.26 Stepping motor computer interface.

3.10.2 Ionisation gauge

Upper Stark state relaxation experiments require pressure in the hexapole chambers to be recorded at the same time as the molecular beam intensity. An MKS ion gauge controller, type 290 is modified so that its Binary Coded Decimal (BCD) output can be latched by the 8255 digital-digital computer interface card (Figure 3.27). Computer interface routines are listed in Appendix 2.

3.10.3 Signal processing and the PCL-8255 lab card

Output from the Amptektron, mass spectrometer and Channeltron electron multiplier detectors is stored on an IBM PC-compatible 80486 computer. Two data acquisition schemes are employed (Figure 3.28).

Analog signals are digitised by a digital storage adaptor (Thurlby, DSA524). The DSA transforms voltage-time information into 1024 8-bit bytes. Repeated acquisitions, triggered by the Pulse Counting Control Unit (see below), are averaged by the DSA and then transferred by 19200 Baud RS-232 serial interface to the computer. Appendix 3 details DSA interface routines. An example of an arrival time distribution recorded in this way is shown in Figure 3.20.

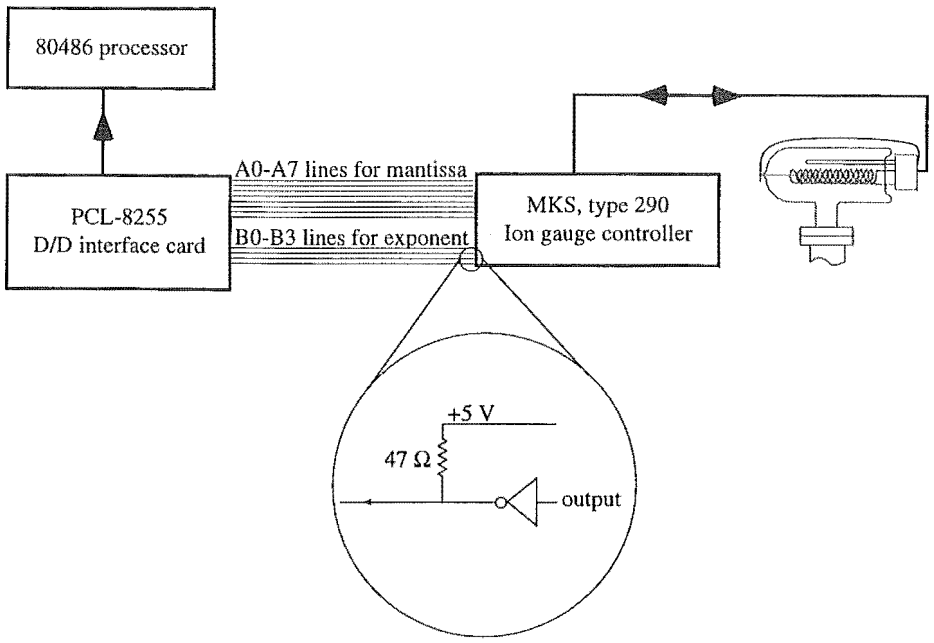

Figure 3.27 Ion gauge computer interface. Each output from the MKS controller is pulled up to +5 V when it goes 'high'. This is a modification on the controller circuit board.

Alternately, signal which is first amplified by an Extranuclear Laboratories pulse counting preamplifier (Amptektron output is already amplified) is directed into the Pulse Counting Control Unit (PCCU). Figure 3.29 illustrates a typical argon beam arrival time distribution. The PCCU takes this signal as a series of +5 V pulses and places two 'windows' or gates over the signal at specified times. These gates or the pulse 'train' during each gates operation is passed to a modified PCL-8255/8253 lab card and counted.

Figure 3.30 details the PCCU circuit and a brief description is given here. Output from a 10 kHz 555 oscillator is fed into a 4017 decade counter. This frequency is divided and passed successively into three further decade counters. Output from these is used (in conjunction with 4013B flip-flops) to switch the gates '1' and '2' on and then off again at the selected times.

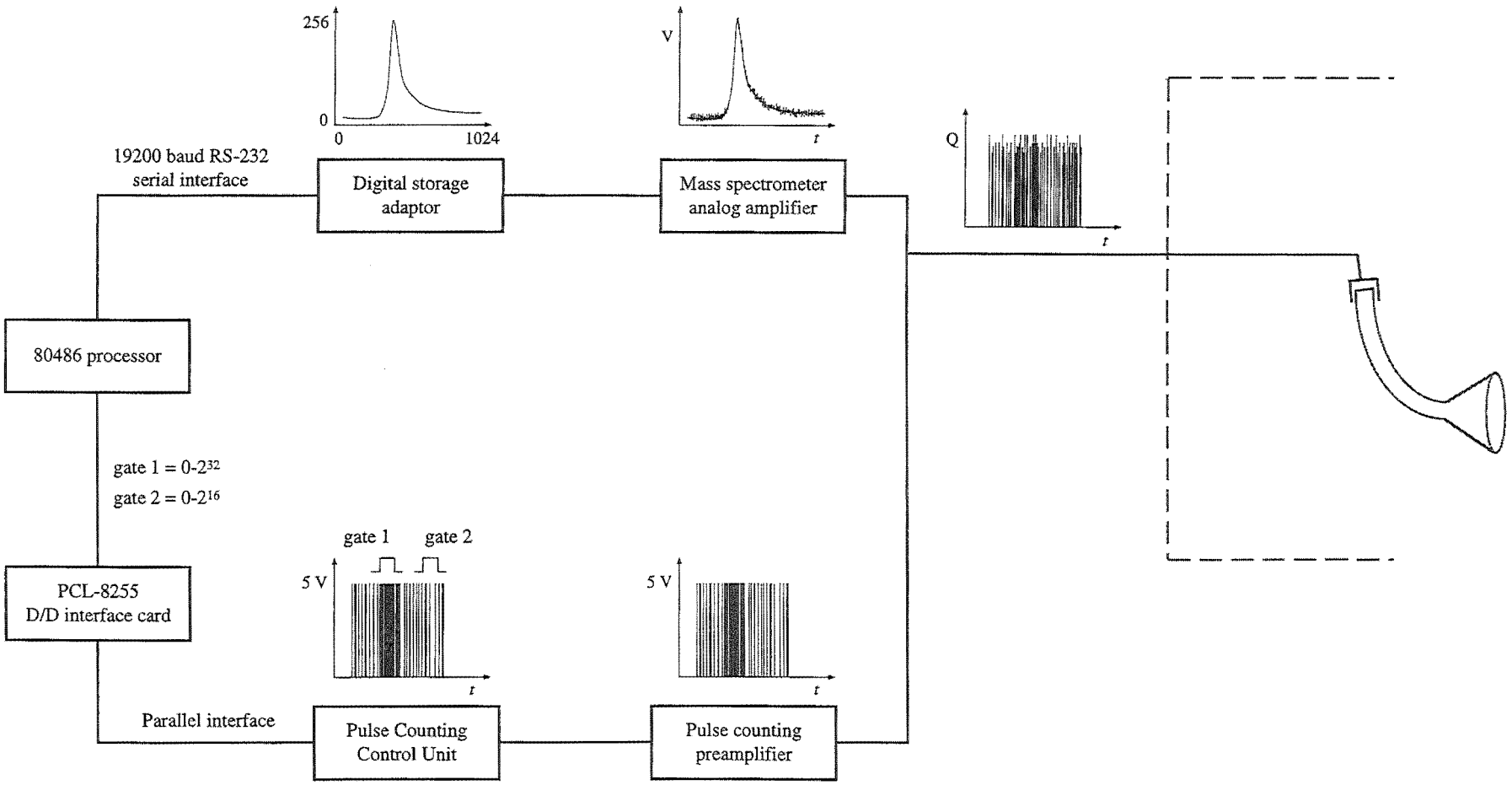

Figure 3.28 Data acquisition schemes.

The beam source driver, digital storage adaptor and oscilloscope, described previously, are triggered from the output of one of three decade counters. Normally this trigger frequency is selected to be 10 Hz.

Pulses passed to the PCL-8255 lab card on the gate 1 and 2 lines are counted by three 8253 multi-mode counters. Counters 0 and 1 operate in combination for gate 1 pulses, while counter 2 is used for gate 2. When counter 0 is full its OUT pin goes high and clocks over counter 1, a circuit containing 74245LS, 7425 octal transceivers and a 7404 inverter is mounted on the PCL-8255 board (Figure 3.31). The 8253 counters must be initialised before data acquisition. Counters 0 and 1, configured differently to counter 2, must be sent two pulses. Counter 2 is initialised without any pulses. The two pulses must be received by the counter CLK pins, however, these are the same pins accepting gate signals from the PCCU. A computer instruction setting pin C1 on an 8255 chip low is inverted by the 7404 chip and passed to the ENG pin of an octal transceiver, preventing the transceiver from passing gate signals to the 8253 chips. The same low value on pin C1 enables the second octal transceiver to pass the required pulses (computer generated) from pin C2 on the same 8255 chip to counters 0 and 1.

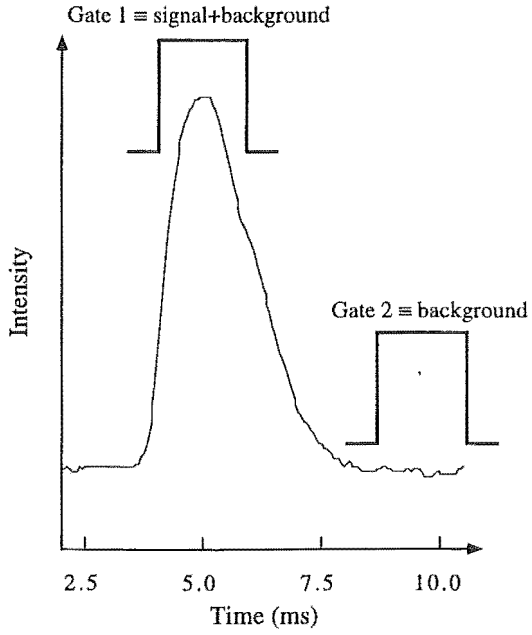

Figure 3.29 Gate placement over an arrival time distribution.

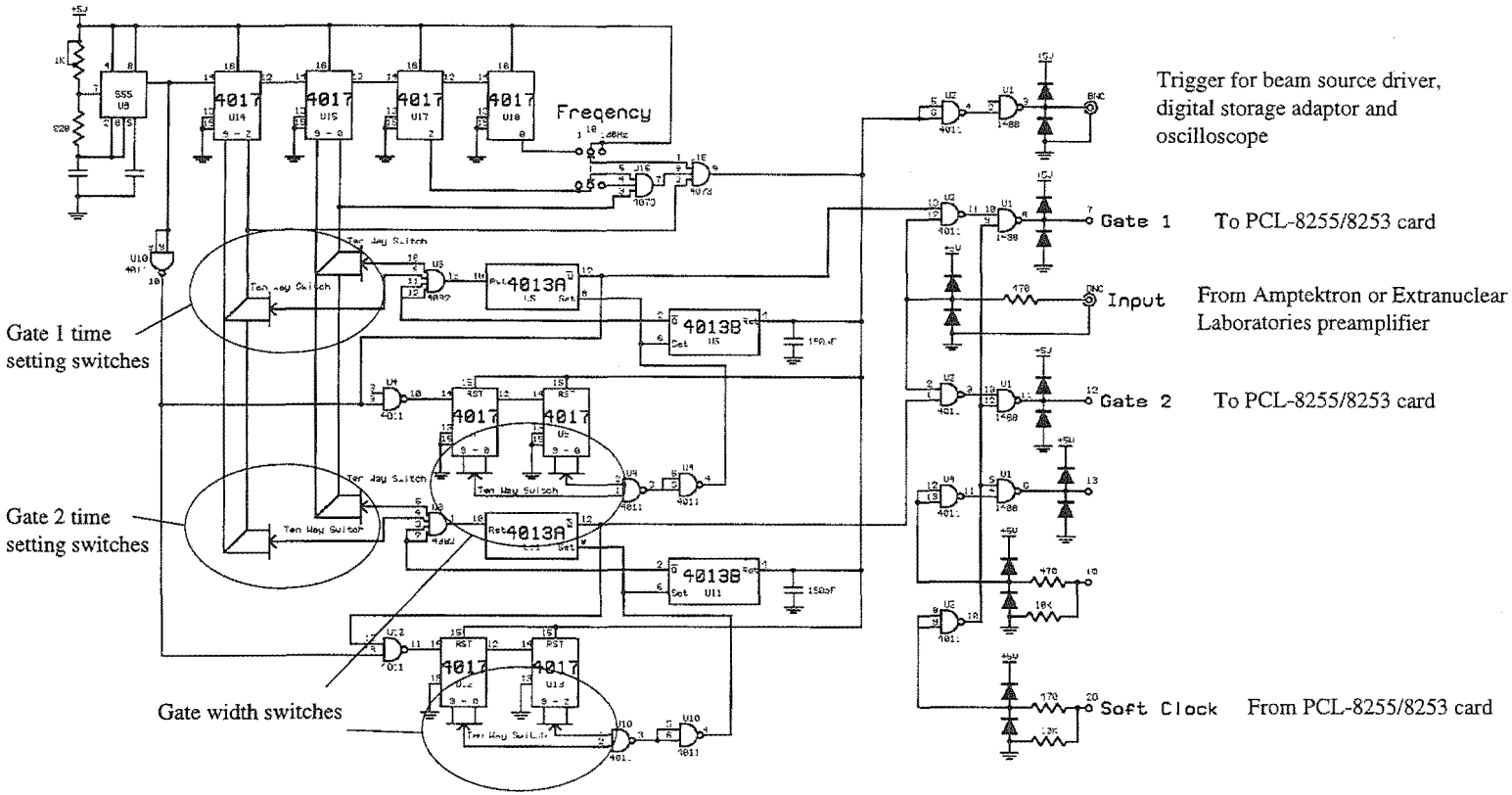

Figure 3.30 Pulse counting control unit circuit.

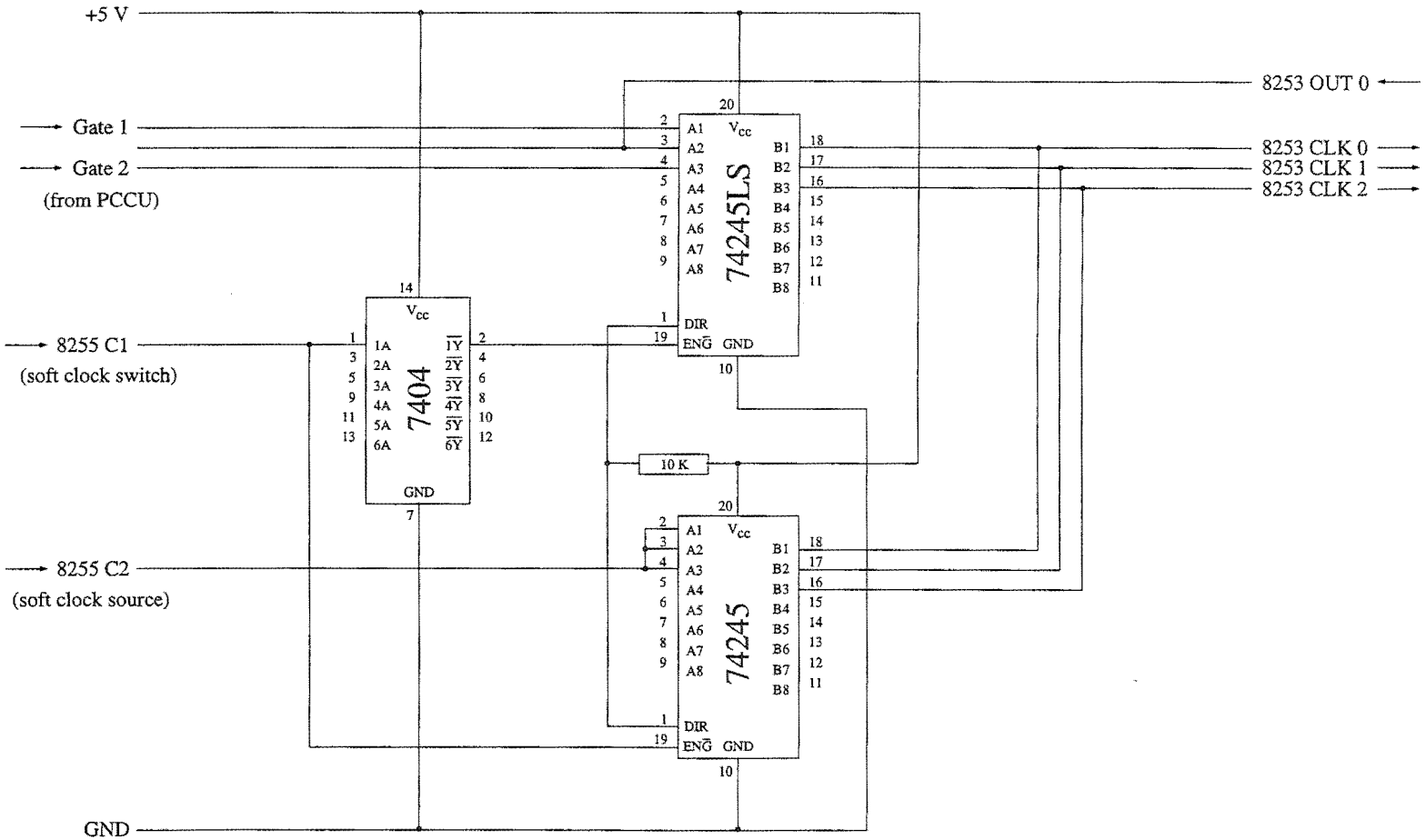

Figure 3.31 8253 multimode counter reset circuit.

Setting pin C1 high enables the gate signals to be passed to the counters again. Appendix 4 details the interface routines that set up and control counting of signals from the PCCU.

The 8255 chip used to control pulse counting is one of four mounted on the PCL-8255 lab card. Each chip has twenty four signal lines (A0-A7, B0-B7, C0-C3 and C4-C7) that may be configured to act as inputs or outputs of digital information. Three lines (CO, C1 and C2) on one chip are used as outputs for pulse counting. The hexapole high voltage power supplies are controlled from the output of another 8255 chip (Appendix 7). In this case lines A0-A7 and C4-C7 are connected to a 12-bit digital-to-analog converter. Although not used for this work, similar control of the SXP300 mass spectrometer electron energy and mass settings is possible.

Configured for input a third 8255 chip is connected to an MKS ion gauge controller. Pressure coded in three 4-bit words, two for the mantissa and one for the exponent is latched in (lines A0-A7 and B0-B3) and recorded periodically during pulse counting experiments. Appendix 2 lists computer instructions for these interfaces.

3.10.4 Miscellaneous interfacing

An ADDA-14 14-bit analog-to-digital and digital-to-analog conversion card is used to collect signals from an electrometer (Keithley, model 486) and a capacitance manometer (MKS, PDR-C-1C) controller. Nozzle backing pressure is recorded periodically by the IBM PC-compatible during both electron impact ionisation asymmetry and M-state quenching experiments. Electron flux striking a Faraday cup opposite the electron gun is recorded during electron impact ionisation asymmetry experiments. Computer interface routines are listed in Appendix 5.

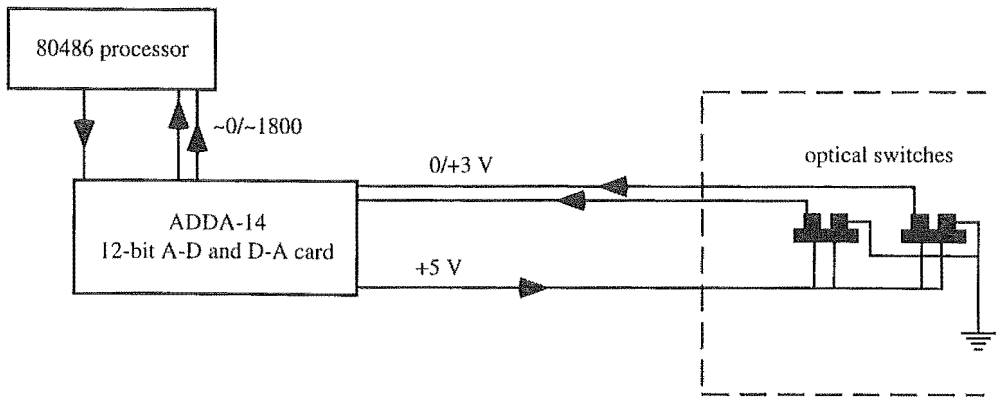

Figure 3.32 Optical switch protection scheme.

The Amptektron particle detector is to be replaced in the future by a rotating quadrupole mass spectrometer, and rotational limit protection measures have been designed using the outputs of two vacuum compatible optical switches. The two switches are connected to analog-to-digital channels on the ADDA-14 card (Figure 3.32). Computer instructions to monitor the status of these inputs are incorporated into the stepping motor control routines. A metal tab, attached to the quadrupole body, passing through the optical path of one of the switches results in motor operation being suspended preventing a collision with other vacuum components. In this way the detectors angular position is also calculated.

Chapter 4

Upper Stark State Relaxation Cross-sections

4.1 Introduction

Symmetric-top molecules are state-selected in a hexapole electrostatic filter as described in §2.4. Those molecules which are in upper Stark states are focused toward the molecular beam axis (ie. move to lower field) by the filter. Experiments reported both in §5 and in many other investigations use the filter to select upper Stark states which are then oriented in a weak homogeneous electric field. It has been observed that orientation asymmetry effects may disappear when background pressure within the hexapole filter is high and that this is due to the defocusing of upper Stark state molecules [Brooks and Harland, private communication]. A cross-section for this process was assumed tentatively to be around 1000 $Å^2$. The purpose of this investigation is to quantify the observed loss of upper Stark state molecules from a molecular beam and to characterise the process in terms of the properties of the interacting species. The rationale behind the experiment is the selective loss of collisionally quenched upper Stark states from their original sinusoidal focusing trajectories. Quenched molecules move to higher field with the consequential attenuation of beam signal with quencher pressure. In a recent theoretical paper

stimulated by the experimental study reported in this thesis the defocusing of upper Stark state molecules is ascribed to collisional relaxation of the M quantum number (§2.5 and §4.3.1.2) [Phillips, 1995]. Phillips reports calculated cross-sections of between 20 $Å^2$ and 150 $Å^2$ for individual rotational states.

The experimental measurement of cross-sections for defocusing of the molecules CH_3Cl and CCl_3H in low rotational states $|JKM\rangle$ within a hexapole electrostatic filter by collisional relaxation of M and/or J quantum states are presented in this chapter. This experiment is the first of its' kind and is a new approach to the investigation of processes involving transfer of minuscule amounts of energy.

A number of quenchers are chosen in order to establish relationships between relaxation cross-section and the charge distribution properties (polarisability and dipole moment) of the interacting species. Cross-sections are found to exhibit a clear correlation with calculated long-range van der Waals potential terms for dispersion, dipole-induced dipole, and dipole-dipole interactions. Cross-sections are also found to increase with decreasing relative velocity, as predicted by theory.

An investigation of the variation of relaxation cross-section with hexapole filter voltage, $\pm U_o$, allows single $|JKM\rangle$ state relaxation cross-sections to be deduced for the molecules CH_3X (X = F, Cl and Br). Calculations of the hexapole filter transmission characteristics for these molecules are presented and used to rationalise the observed relaxation cross-section dependencies.

The method by which relaxation cross-sections are measured also provides information on the magnitude of elastic/inelastic collision cross-sections for each beam-quencher combination. While the experimental apparatus is not optimised for the determination of accurate total elastic/inelastic collision cross-sections, results for CH_3Cl-inert gas combinations show good correlation with the same long range electrostatic potential employed in the discussion of relaxation cross-sections.

4.2 Experimental

The theoretical basis for the measurement of collision cross-sections is detailed in §2.5. To summarise, the intensity of a beam of particles, in this case symmetric top molecules, is recorded as a function of quencher gas pressure within a collision cell sandwiched between the beam source and beam detector. For the determination of relaxation cross-sections the collision cell must encompass a hexapole electrostatic filter. Figure 4.1 illustrates the experimental arrangement used here. The cell is defined as the region between the skimmer (S2) and exit aperture (EA). Cell and hexapole lengths are noted in Figure 4.1 with aperture radii.

A pulsed supersonic molecular beam is formed in the nozzle chamber as described in §2.2 and §3.4, and is collimated by two skimmers, one of which is S2, prior to entering the cell.

Pressure in the scattering cell is determined by a Bayard-Alpert-type ionisation gauge (Duniway Stockroom, T-100-K) mounted on a 2 3/4"-Conflat flange to the first hexapole chamber. The gauge is calibrated against a number of gases using a differential MKS capacitance manometer (§4.2.1). Output from the gauge controller is read by a 80486 IBM-compatible computer (§3.10.2). Quencher gas enters the cell through a Leybold-Heraeus variable leak valve (283-41 DN 10KF) which is mounted on a 2 3/4"-Conflat flange to the first hexapole chamber. The valve is coupled to a stepping motor driven by the same 80486 computer (§3.10.1). Software subroutines to read ionisation gauge pressure and control the motor operate together in a negative feedback loop to set quencher pressure and keep it constant as required (Appendix 6).

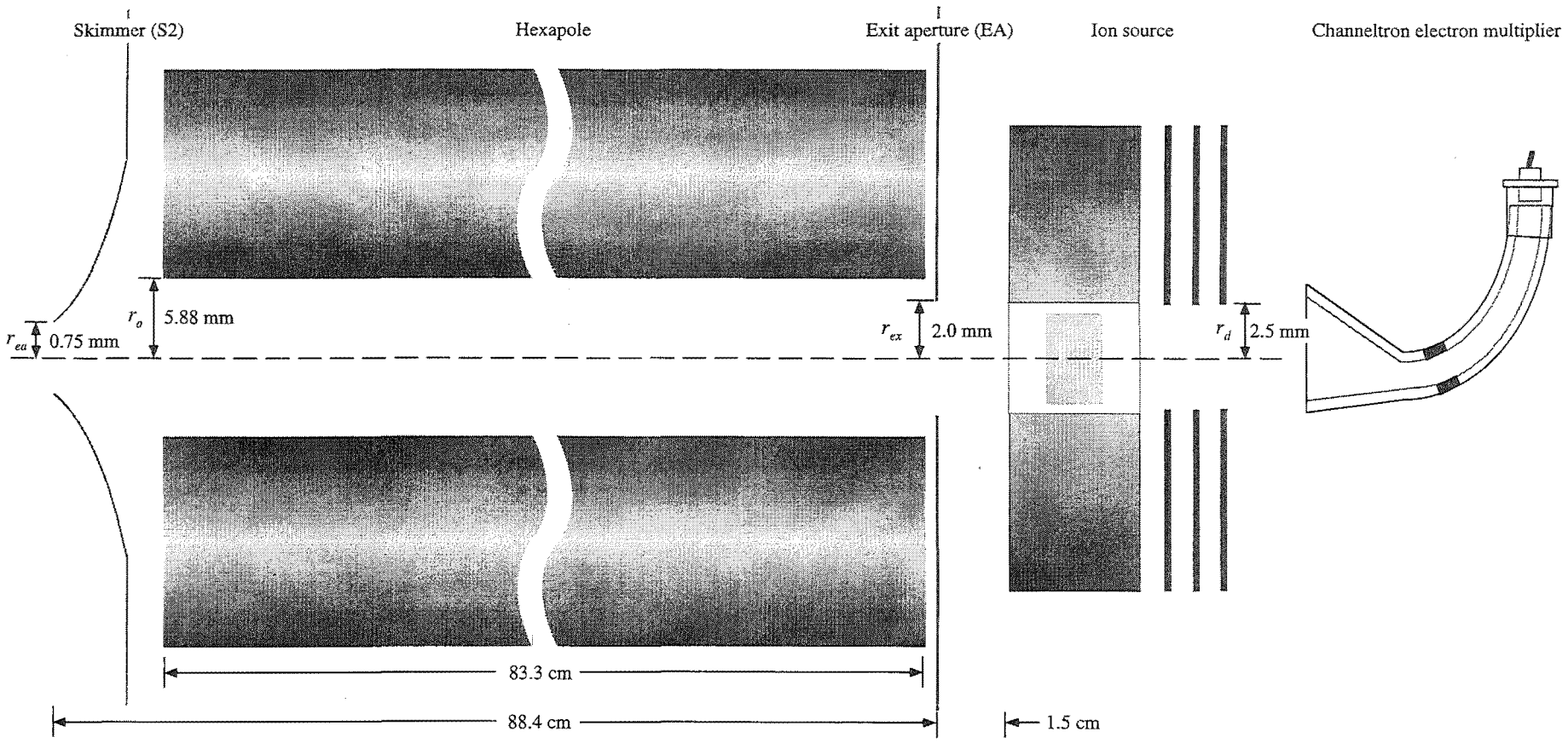

Figure 4.1 Experimental arrangement. Scale distorted.

Pressure within the confines of the hexapole filter is assumed to be equal to the pressure in the surrounding chamber. To ensure this, one of the VHS-4 diffusion pumps attached to the hexapole chambers is valved off completely and the other partially throttled. The rates of effusion into and out of the cell are then assumed to be constant and small.

Pressure in the cell is kept below 10^{-4} torr throughout experimental measurements to prevent electrical discharge of the hexapole filter. The buffer and scattering chamber pressures are maintained at 10^{-7} and 10^{-8} torr, respectively, so there is often a large pressure drop between the scattering cell and adjacent chambers. There will be leakage of quencher gas into both buffer and scattering chambers through the skimmer and exit apertures resulting in an increase in the effective scattering cell length. This increase or *end effect* is insignificant for the experimental arrangement here due to the overall length of the cell and the way in which the relaxation cross-sections are determined (§4.2.3).

Cryogenic pumping in the form of four liquid nitrogen cold traps within the cell reduces background pressure to 10^{-8} torr. Completely filled cold traps are able to maintain this pressure for between 45 and 50 minutes. Experiments must be performed during this period. Addition of liquid nitrogen to the cold traps results in an initial increase in trap temperature as N_2 carrier gas passes through. Pressure within the vacuum system increases significantly and affects the quenching process. Measurements to determine relaxation cross-sections at fixed hexapole voltage (§4.3.1) last 10 minutes for each beam-quencher combination, and several experiments may be performed before the liquid nitrogen cold traps require refilling. When the variation of cross-section with hexapole voltage is investigated measurement times are limited by the cryogenic pumping cycle to 45 minutes.

Hexapole voltage supplies (0 to ±30 kV DC) are controlled by a computer driven 12-bit 10 V DC digital-to-analog converter. The hexapole voltage may be set to within ±7 V of the desired value (§3.10.3). An upper limit of ±5 kV is imposed by the increased possibility of electrical discharge at high quencher pressures.

Molecular beam intensity is measured by a channeltron electron multiplier coupled with an electron bombardment ion source (§3.8.3). Important dimensions of the multiplier/ion source unit are shown in Figure 4.1. The ion source entrance aperture, subsequently referred to as the detector aperture (DA), is centred about the molecular beam axis by adjustment of the *xyz*-translator to which the detector is attached. Figure 4.2 illustrates beam profiles for CH_3Cl along both horizontal and vertical axes (defined with respect to the laboratory). Settings for the nozzle, ion source and detector are listed in Table 4.1. Electron energy and ion energy are adjusted to maximise the detection of beam species and minimise the contribution to signal from background gas. Lower electron energy favours ionisation of species having lower ionisation potentials. For CH_3Cl and CCl_3H ionisation potentials are 11.22 and 11.37 eV respectively, which are lower than the values of the expected background N_2 and O_2 with ionisation potentials of 15.58 and 12.07 eV, respectively. Increasing ion energy improves the detection of species with higher mass-to-charge ratios and is set differently for the two beams used here.

	CH_3F	CH_3Cl	CH_3Br	seeded CCl_3H
Nozzle-skimmer (mm)	11.5	11.5	11.5	11.5
Electron energy (eV)	50	50	50	20
Ion energy (eV)	16.2	16.2	16.2	40
Emission (μA)	50	50	50	150
Multiplier cone (kV)	1.57	1.54	1.58	1.59

Table 4.1 Important nozzle, ion source, and channeltron settings.

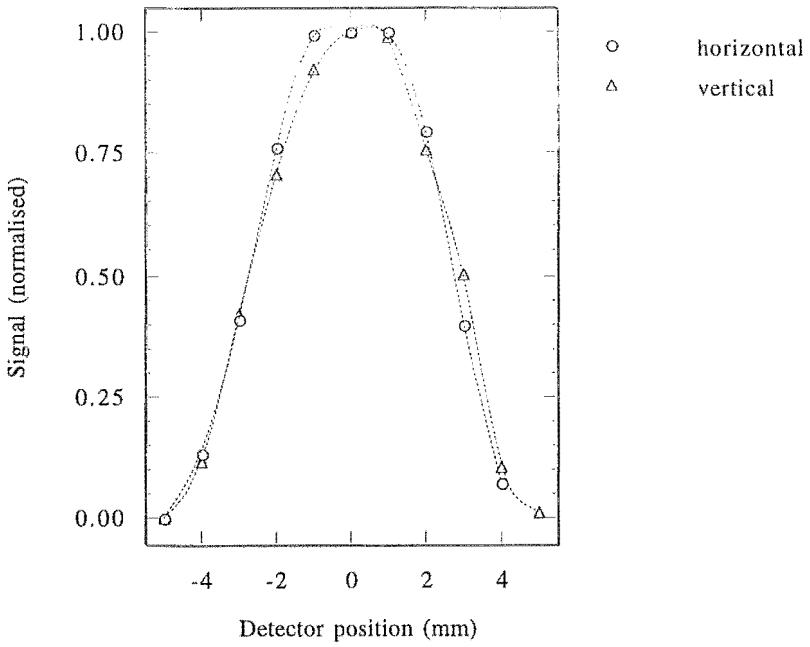

Figure 4.2 CH_3Cl molecular beam profiles measured with the channeltron detector.

Output from the channeltron is a series of current pulses, each corresponding to the detection of a single ion (where ion detection rates are less than 10^6 s^{-1}). Pulses are transformed into 5 V TTL pulses by a preamplifier/discriminator (Extranuclear Laboratories, model #032-3) and processed by the Pulse Counting Control Unit (PCCU) as described in §3.10.3 and §4.2.2.

4.2.1 Ion gauge calibration

Pressure in the scattering cell is measured with a Bayard-Alpert-type ionisation gauge (Duniway stockroom, T-100-K) and recorded by computer, as detailed in §3.10.2. The ionisation gauge consists of a rhenium filament, attractor grid and collector wire. Gas within the gauge is ionised by electrons emitted from the hot filament. The success of the electron impact process (§2.6) is dependent on the gas species' ionisation cross-section. Ions are accelerated from the grid, held at +150 V, to the thin wire anode held at ground potential where they register as a current in an external electrometer circuit. For identical ionisation gauge operating conditions (ie. voltages and filament current)

the current measured at the collector is proportional to the gas pressure in the gauge and the electron impact ionisation cross-section. The gauge and controller are factory calibrated with air and a corresponding ionisation cross-section of 2.81 $Å^2$ at 75 eV [Lampe, 1957]. For this work, a number of different gases are used and so the relationship between measured and true pressure in terms of ionisation cross-section at 75 eV is first determined by calibration against a differential MKS Baratron (model 310-CH) capacitance manometer (10^{-5}-10 torr).

The manometer consists of a thin metal diaphragm-fixed ring capacitor exposed on one side to the pressure of interest and on the other to a reference pressure (10^{-7} torr) at least two orders of magnitude lower than the resolution of the device. The difference in capacitance between the diaphragm and fixed ring electrode is determined by a comparator and output as absolute pressure independent of gas species.

Figure 4.3 shows the separate vacuum system used for ionisation gauge calibration. The chamber is evacuated to a pressure of $5x10^{-8}$ torr by a 300 l/s Alcatel, TMP-5400CP turbomolecular pump backed with a 345 l/min Alcatel, 2021 mechanical pump. Reference pressure for the Baratron device is separately maintained by a 100 l/s Edwards diffusion pump and an Alcatel 100 l/min 2004A mechanical pump.

Pure gases with known 75 eV electron impact ionisation cross-sections are bled into the chamber with a Leybold-Heraeus variable leak valve (model 283-41 DN 10 KF). Pressure recorded by the ionisation gauge control unit is plotted against that found using the Baratron. Slopes from these plots are obtained for He, N_2, Ar and Kr. Figure 4.4 illustrates typical measurements for He. The average slopes for each of the four gas samples are summarised in Table 4.2. From these slopes the following relationship for absolute pressure is determined:

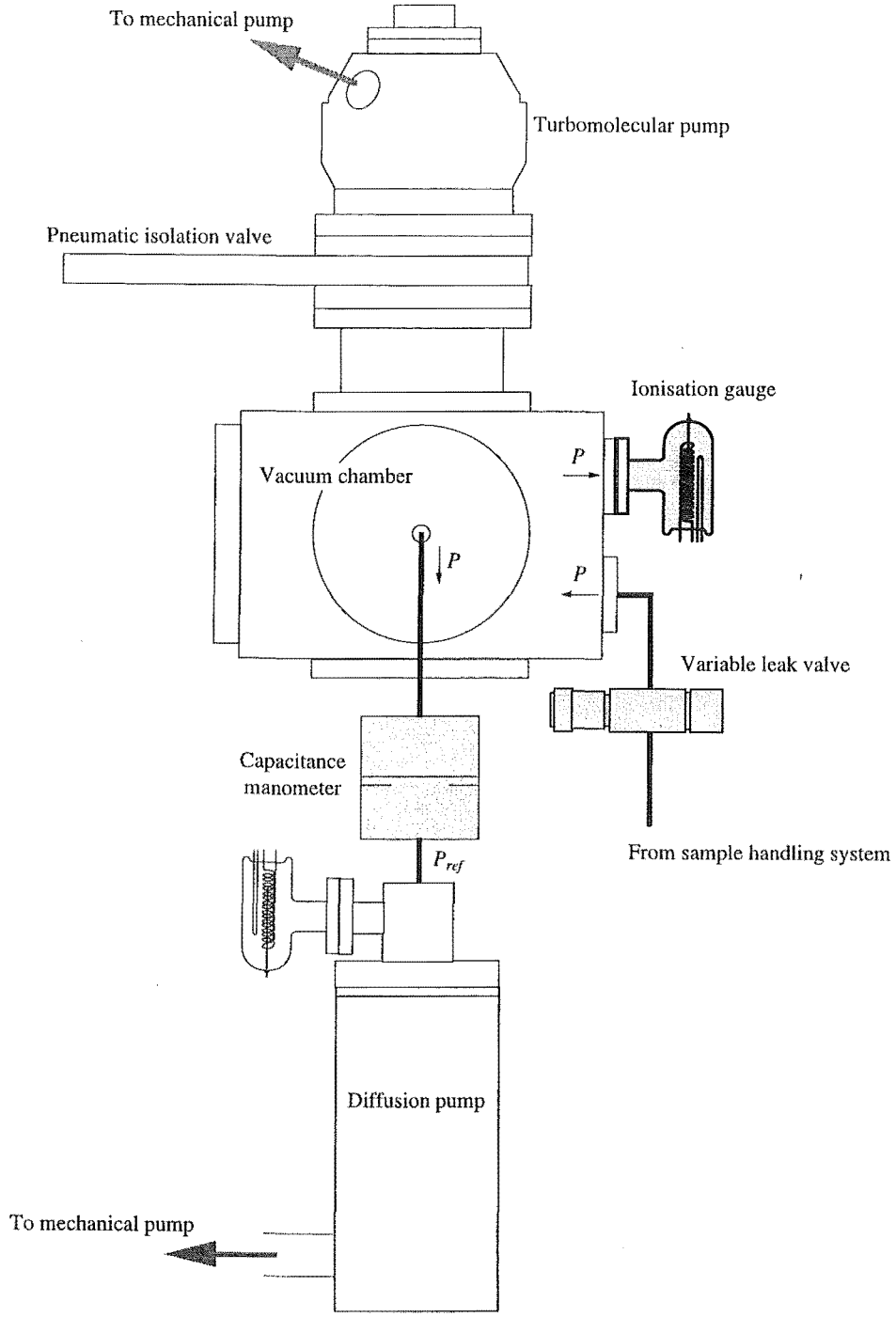

Figure 4.3 Ionisation gauge calibration apparatus. Not to scale.

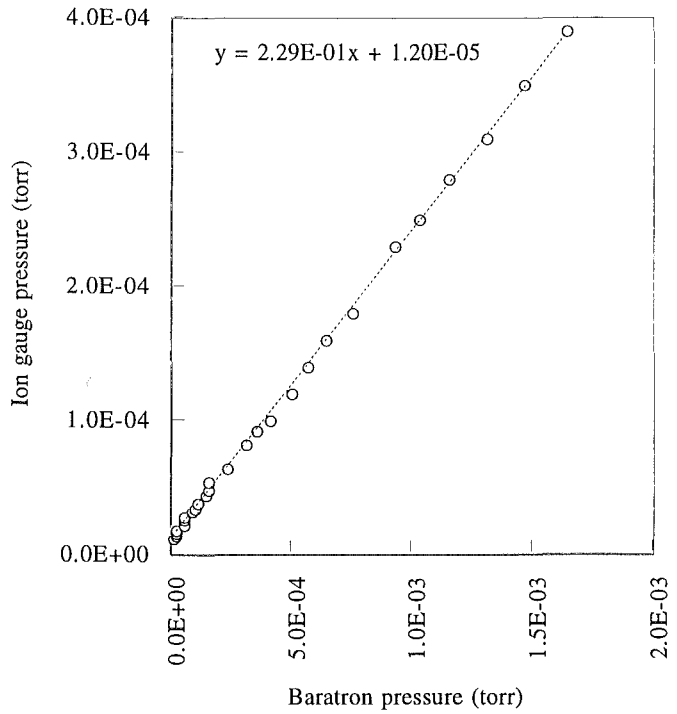

Figure 4.4 Typical ion gauge calibration results for He.

$$P = \frac{P_{IG}}{0.41\sigma_{EI} + 0.047} \tag{4.1}$$

where P_{IG} is the pressure measured with the ionisation gauge and σ_{EI} the 75 eV electron impact ionisation cross-section.

	Slope	σ_{IE} (x10^{-16} cm^2)
He	0.21±0.01	0.386
N_2	1.16±0.02	2.88
Ar	1.56±0.02	3.52
Kr	2.15±0.08	5.18

Table 4.2 Ion gauge calibration slopes.

4.2.2 Data acquisition

5 V TTL pulses from the signal preamplifier/discriminator (§4.2) are processed by the Pulse Counting Control Unit (PCCU) as described in §3.10.3. A brief summary is given here. The supersonic molecular beam is pulsed at a frequency of 10 Hz. For a period of 2-3 ms, ten times a second, the detector will receive ions formed from beam molecules (and background gas) while for the remaining time ion signal will be due to background gas only. Figure 3.29 illustrates the arrival time distribution of CH_3Cl. The PCCU *gates* the incoming signal into two separate time periods, *gate* 1 and *gate* 2. Figure 3.29 also illustrates the positioning of these gates so that beam and background signal is monitored by gate 1 while background only is monitored by gate 2. The PCCU supplies the trigger for the Beam Source Driver (BSD) and gate positions and width are set on the front panel.

Both gate signals are directed into an 8253/8255 pulse counting card inside the 80486 computer. Software subroutines initialise counter chips on the card to accumulate gate signals, and latch the number of counts after a time, t_c. Beam intensity recorded by the computer is given as

$$I = gate\ 1 - gate\ 2. \tag{4.2}$$

Both gates are set 2.0 ms wide to collect as much beam signal as possible. Gate 2 is positioned 0.2 ms after the nozzle opens and records background signal only. Gate 1 is then adjusted with the beam on to maximise intensity, I. For CH_3Cl this position is 3.6 ms.

Hexapole voltage and quencher pressure are controlled by software subroutines (§3.10 and §4.2). Quencher pressure, P_{IG}, and beam intensity, I, are recorded by software routines also. Experiments described here are preformed by the 80486 computer using

these subroutines (Appendix 8). A single experiment, whether it be the determination of relaxation cross-sections at fixed hexapole voltage, or as a function of hexapole voltage, follows the procedure below:

1) The experimentalist enters into the computer parameters listed in Table 4.3.
2) Pressure is set by the computer and allowed to stabilise for 2-10 seconds depending on the condensability of the quencher.
3) Beam intensity is recorded first with the hexapole switched off, $I_{o,P}$, and then at each hexapole voltage specified in step 1, $I_{HV,P}$. Quencher pressure is monitored and adjusted as necessary during measurements to keep it constant.
4) Steps 2-3 are repeated until measurements have been made at all quencher pressures specified in step 1.
5) The variable leak-valve is closed and the computer analyses intensity measurements following the methods described in §4.2.3.

Number of pressure increments	7 - 8
Pressure increment	1×10^{-6} torr for He through to 5×10^{-6} torr for Xe
Voltage range	0 and 5 kV, or 0 to 5 kV in 250 V steps
Quencher ionisation cross-section	[Lampe, 1957]

Table 4.3 Parameters for computer controlled attenuation experiment

Experiments are repeated a number of times (§4.3.1 and §4.3.2) for each beam-quencher combination (see Tables 4.4 and 4.5).

4.2.3 Data analysis

Collision cross-sections are calculated using the Beer-Lambert equation

$$\frac{I}{I_o} = \mathrm{e}^{-nL\sigma} \tag{4.3}$$

where I is beam intensity, n the quencher particle density in cm^{-3}, L the scattering cell length in cm, I_o the beam intensity in the limit of no attenuation, and σ the collision cross-section in cm^2. Particle density, n, is calculated from the measured ion gauge pressure after a correction (equation 4.1) and application of the ideal gas equation, to give

$$\ln I = \frac{-P_{IG} \cdot 3.2404\mathrm{x}10^{16} \cdot L}{0.41\sigma_{EI} + 0.047}\sigma + \ln I_o \tag{4.4}$$

where P_{IG} is the ion gauge pressure in torr, and σ_{EI} the quencher ionisation cross-section at 75 eV. The validity of using the ideal gas equation to calculate quencher pressure is questionable, however, it is also used in the calculation of electron impact ionisation cross-sections and it is expected that the deviations from ideality for the two calculations are cancelled out to a large extent by the form of equation 4.4.

The cross-section for relaxation of upper Stark state molecules requires a knowledge of the intensity of upper Stark state molecules reaching the detector. Removing the contribution of elastic and inelastic collisions to beam attenuation by subtracting the zero hexapole voltage beam intensity,

$$I_{SS,P} = I_{HV,P} - I_{o,P}, \tag{4.5}$$

leaves the upper Stark state beam intensity, $I_{SS,P}$. When hexapole voltage is close to zero the transmission of upper Stark state molecules is negligible and $I_{HV,P} \approx I_{o,P}$. The threshold for transmission of upper Stark state molecules is given by

$$U_{th} = \frac{\pi^2 r_o^3}{6l^2} \frac{mv^2}{\mu} \tag{4.6}$$

where l is the hexapole length, and v the average beam velocity. Below this threshold cross-sections calculated with equation 4.4 are meaningless and are set to zero.

A plot of P_{IG} against beam intensities, I, measured at each pressure gives a straight line, where the slope is determined by a linear least-squares analysis [Atkins, 1994]

$$s = \frac{-3.2404\text{x}10^{16} \cdot L}{0.41\sigma_{EI} + 0.047}\sigma. \tag{4.7}$$

Figure 4.5 illustrates typical attenuation observed for upper Stark state molecules of CH_3Cl with Ar quencher. Equation 4.7 is rearranged to give the collision cross-section

$$\sigma = \frac{-s \cdot (0.41\sigma_{EI} + 0.047)}{3.2404\text{x}10^{16} \cdot L} \text{ in cm}^2. \tag{4.8}$$

The choice of scattering length, L, in the Beer-Lambert equation, is different for determination of relaxation cross-sections than that for elastic or elastic/inelastic cross-sections. The focusing of upper Stark states only occurs in the presence the inhomogeneous electric field, therefore the attenuation path length must be equal to the length of the hexapole, 83.3 cm. Strictly, L will be larger than this because field strength does not fall to zero immediately outside the filter. However, the simple harmonic motion that an upper Stark state molecule undergoes in the field will not be stable until it enters the filter proper, and the author believes the choice of 83.3 cm to be justified.

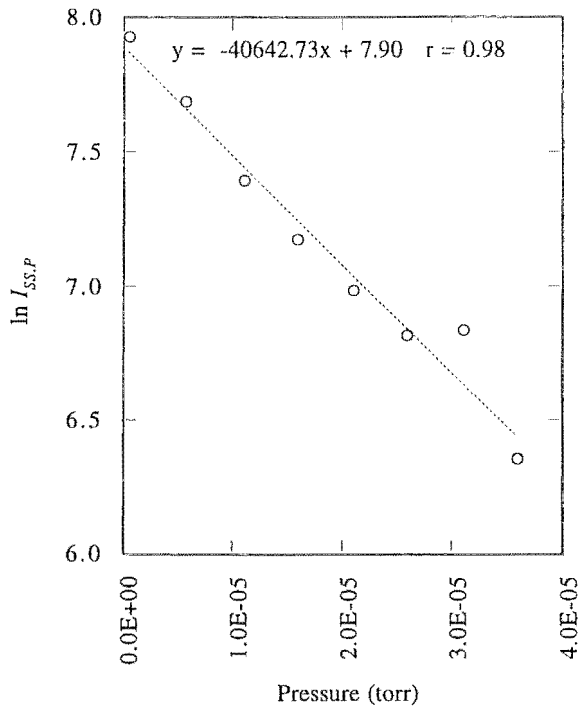

Figure 4.5 Attenuation of CH_3Cl upper Stark state molecules by Ar.

The statistically correct Q-test is applied to all sets of measurements to reject outliers with 90% confidence so that those remaining values are not subject to random variation [Dean and Dixon, 1951]. Discussion of the magnitude of the cross-section standard deviations is expanded in §4.3.1.

4.3 Results and discussion

The results and discussion presented here are separated into three sections: relaxation cross-sections measured at fixed hexapole voltage (5 kV); variation of relaxation cross-section with hexapole voltage; and elastic/inelastic collision cross-sections.

4.3.1 Relaxation cross-sections measured at $U_o = \pm 5$ kV

Collision cross-sections for the relaxation of upper Stark state molecules of CH_3Cl and 20% CCl_3H seeded in Ar within a hexapole filter whose rods are biased at ±5 kV are

reported and discussed here. Tables 4.4 and 4.5 list the measured cross-sections for each beam-quencher combination. These results represent the first measurements of symmetric top upper Stark state relaxation cross-sections. A range of non-polar and polar quenchers are studied in order to test the validity of any model proposed to account for the relaxation process.

The results for seeded CCl_3H have higher standard deviations than those measured for CH_3Cl. This is rationalised in terms of the seeding process. It is unlikely that the volatile liquid-inert gas mixture will be homogeneous and composition will vary during the course of an experiment. This is especially so for such a high seed-carrier ratio, however, mixtures with lower ratios are impractical because of the low detection efficiency of CCl_3H, and samples of pure CCl_3H frequently block the supersonic nozzle. Van der Waals clusters of CCl_3H molecules may also form in the supersonic expansion and this is highly dependent on the seed-carrier ratio. Variation of this ratio during an experiment would result in a change of cluster concentration and the rotational population distribution of remaining molecules.

Quencher	σ (Å^2)	$\pm$ (Å^2)	Measurements
He	190	17	9
Ne	157	11	9
Ar	224	19	9
Kr	242	18	9
Xe	277	19	9
N_2	276	24	9
SF_6	251	17	9
CO_2	227	19	9
N_2O	278	30	5
CH_3F	382	43	3
CH_3Cl	443	26	9

Table 4.4 Relaxation cross-sections for a beam of CH_3Cl.

Quencher	σ (Å^2)	$\pm$ (Å^2)	Measurements
He	245	109	12
Ne	152	27	8
Ar	379	159	10
Kr	418	94	9
Xe	401	26	8
N_2	349	24	10
SF_6	288	43	7
CO_2	275	21	7
N_2O	326	59	10
CH_3F	344	64	7
CH_3Cl	397	80	8
CCl_3H	815	172	9

Table 4.5 Relaxation cross-sections for a beam of 20% CCl_3H seeded in Ar.

Results from Tables 4.4 and 4.5, and additional investigations, are discussed in the following sections:

- comparison with available literature;
- velocity dependence of cross-sections, determined by seeding CCl_3H in the carriers He, Ar and Xe; and
- correlation with long range van der Waals potentials.

4.3.1.1 Comparison with literature

A rationalisation for the involvement of M and J quantum number transitions in the relaxation process is presented in §2.5. A brief summary is given here.

Cross-sections of the order reported here suggest that interaction occurs between beam-quencher species at distances greater than 7-8 Å. A van der Waals potential for CH_3Cl-Ar including terms for dispersion and dipole-induced dipole interactions calculated at

this distance amounts to 29.7-13.3 J mol^{-1}. The minimum energy difference between adjacent rotational energy states for CH_3Cl is 21.2 J mol^{-1} (refer to Figure 2.13). Transitions involving $\Delta K \neq 0$ are forbidden. In contrast, the energy difference between adjacent Stark states,

$$\Delta W_{\Delta M=\pm 1} = \pm \mu \varepsilon \frac{K}{J(J+1)} \qquad (4.9)$$

is only 1.6 J mol^{-1} for CH_3Cl J = K = 1 states at a hexapole voltage of ±3.4 kV and assuming a radial displacement $r = r_0 / 2$ (§2.4 and §4.3.2.2). Energy for $\Delta J = \pm 1$ (low J) and $\Delta M = \pm 1$ transitions is available from the van der Waals interaction at the separations corresponding to cross-sections measured here.

The paper of Phillips calculates relaxation cross-sections specifically for our apparatus using time-dependent perturbation theory and a van der Waals potential term for dipole-induced dipole interactions. Cross-sections for CH_3X (X = F, Cl, Br and I) and CF_3Cl molecules are calculated considering only the transitions $\Delta M = \pm 1, \pm 2$.

Calculated cross-sections reported by Phillips for collisions with the CH_3F-Ar beam-quencher combination are 70-80 Å^2. Phillips takes the cross-sections for individual rotational states and averages them over the calculated rotational state population distribution. For CH_3Cl-Ar at a hexapole voltage of ±5 kV the 'total' relaxation cross-section is calculated to be ~60 Å^2. This value does not compare well with the experimentally determined cross-section of 224 Å^2.

While Phillips does argue convincingly the involvement of ΔM transitions and a long range van der Waals potential in the relaxation process, a number of predictions are inconsistent with experimental results. Phillips excludes ΔJ transitions from the calculation to determine cross-sections, because of the insufficient energy available from the van der Waals interaction potential at a separation of 10 Å. However, Phillips

ignores dispersion interactions in calculating this energy. Including a dispersion term in the van der Waals potential shows that energy of the magnitude required for ΔJ transitions (low J) is available at such separations. Calculated hexapole transmission curves for CH_3Br, based on the experimental arrangement used here, do not agree in form or magnitude with experimental curves. This lack of agreement suggests that either the trajectory calculations or the choice of rotational population distribution over which transmission probability is summed are flawed. Plots of experimental cross-section against hexapole voltage show a number of peaks corresponding to the relaxation of individual rotational states. The fact that these features are observed indicates that a low rotational temperature is used in calculations (§4.3.2). Using the same temperature in transmission curve calculations should have resulted in more complex curve structure than is reported (§4.3.2).

Toennies measures J'→J" collision cross-sections for J-state-selected TlF molecules for a range of non-polar and polar quenchers [Toennies, 1962]. Cross-sections for the $|2,0\rangle$ state of 152 Å^2 for He and 2140 Å^2 for NH_3 (r_{max} ~ 26 Å!) are reported. The large variation in cross-section is argued to result from the dipole-dipole interaction, and in the case of symmetric-top molecules, the possibility of dipole locking because of the homogeneous electric field present within their collision cell.

Bennewitz, *et al.* measure the cross-sections for TlF molecules in $|1,0\rangle$ and $|1,1\rangle$ states by collision with a beam of inert gas atoms [Bennewitz, 1964]. A range of relative velocities are investigated, all lower than those reported here because of the effusive beam sources employed. Cross-sections for attenuation with Ar quencher are approximately 674 Å^2, from either state, for a relative velocity of 305 m s^{-1}. The result for CH_3Cl-Ar measured here is 224 Å^2 at a relative velocity of 687 m s^{-1}. The energy difference between adjacent Stark states for TlF depends on the square of the dipole moment and is approximately 0.02 J mol^{-1} for J = 1 and a field strength of 300 V cm^{-1}. Adjacent J-levels are separated by at least 5.3 J mol^{-1}, therefore transitions of either

ΔM or $\Delta J = \pm 1$ for TlF requires a much smaller van der Waals interaction, which is available at larger distances. At equal relative velocities the cross-section for collision with Ar for CH_3Cl will be significantly smaller than that for TlF (§4.3.1.2). This difference is probably due to the larger polarisability volume and dipole moment of TlF, 6.7 $Å^3$ and 4.23 D, respectively, which influence the strength of the van der Waals interaction.

4.3.1.2 Velocity dependence

Experiments in which collisions of alkali-metal and inert gas atoms are investigated show an inverse relationship between total cross-section and relative velocity of the collision species [Rothe and Bernstein, 1959]. This is rationalised qualitatively in the following manner. The transition resulting in beam attenuation has a non-zero probability of occurring when there is a frequency component in the combined projectile-target (beam-quencher) wavefunction equal to the energy difference of that transition. Transition probability is proportional to the magnitude of the frequency component. At higher relative velocities the interaction time is less which has the direct effect of reducing the width and magnitude of the Fourier frequency profile [Hagstrum, 1953]. Cross-sections will decrease at higher relative velocities as a result of the decreased amplitude of the favourable frequency components.

The quantitative effect of relative velocity on cross-section depends largely on the form of the interaction potential that describes the process. Rothe and Bernstein find cross-sections to have a velocity dependence, $v_r^{-0.4}$, with

$$v_r = \left(v_b^2 + v_q^2\right)^{1/2} \tag{4.10}$$

where v_b and v_q are the beam and quencher velocities. Landau and Lifshitz, and Massey and Mohr independently calculated the velocity dependence to be $v_r^{-2/(s-1)}$ for a

potential varying as r^{-s} [Massey and Mohr, 1934; Landau and Lifshitz, 1959]. The experimental observation by Rothe, *et al.* is equivalent to $s = 6$, as expected.

Relaxation cross-sections are reported in Table 4.6 for 20% CCl_3H seeded in the carrier gases He, Ar and Xe, with Ar as the quencher. The effect of changing the carrier gas is to vary beam velocity from a calculated 327 m s^{-1} for the Xe carrier to 712 m s^{-1} for the He carrier (§2.2.2). Interpretation of these results is hampered by the large standard deviation of each cross-section and optimisation of the experimental apparatus for these measurements is necessary (§4.4). However, an inverse relationship between velocity and relaxation cross-section is evident and the power-fit of Table 4.6 data is equivalent to $s = 6$. Correlations between cross-section and long range van der Waals potential terms discussed in §4.3.1.3 are made after multiplying the potential terms by the $v_r^{-0.4}$ relative velocity dependence.

Carrier gas	v_r (m s^{-1})	σ (Å^2)	$\pm$ (Å^2)	Measurements
He	816	288	71	9
Ar	635	379	159	10
Xe	514	387	80	8

Table 4.6 Relaxation cross-sections for seeded CCl_3H with an Ar quencher.

4.3.1.3 Correlation with van der Waals potentials

The existence of cross-sections 150 Å^2 and higher suggests that a long range interaction (>7 Å) is responsible for the observed deflection of beam molecules. Rationalisation for this assertion is presented in §2.5 and above. The process may be described by a van der Waals potential of the form

$$V(r) = -\frac{C}{r^6} \qquad (4.11)$$

where r is the interparticle separation and C the van der Waals constant for the beam-quencher combination. The van der Waals constant is expressed as the sum

$$C = C_{disp} + C_{d-ind} + C_{d-d} \tag{4.12}$$

where the three C terms (from left to right) are for dispersion (London), dipole-induced dipole, and dipole-dipole interactions.

The first two terms are given by

$$C_{disp} = \frac{2}{3}\alpha_1'\alpha_2'\frac{I_1 I_2}{I_1 + I_2}, \text{ and} \tag{4.13}$$

$$C_{d-ind} = \frac{\mu_1^2 \alpha_2'}{4\pi\varepsilon_o}, \tag{4.14}$$

where the subscripts 1 and 2 refer to the individual collision participants, α' are polarisability volumes in 10^{-30} m^3, I are ionisation potentials in volts, μ_1 the dipole moment of participant 1 (the beam molecule) in C m, and ε_o the vacuum permittivity. These properties are known for all beam-quencher combinations investigated here.

The separation r is calculated from measured relaxation cross-sections by eqn. 2.63. Figures 4.6 and 4.7 are plots of $(C_{disp} + C_{d-ind}) \cdot v_r^{-0.4}$ against separation for CH_3Cl and 20% CCl_3H seeded in Ar colliding with non-polar species. Relative velocity is calculated from eqns. 2.3, 2.8 and 4.10. Correlation is observed in both plots for inert gas quenchers suggesting that cross-section is proportional to the strength of the electrostatic interaction. For a higher van der Waals constant the resonance between the established field and the ΔM or ΔJ transition will be reached at greater separations resulting in a higher cross-section (§2.5). Cross-sections for both SF_6 and CO_2 quenchers do not fit the correlations shown in Figures 4.6 and 4.7. These gases are

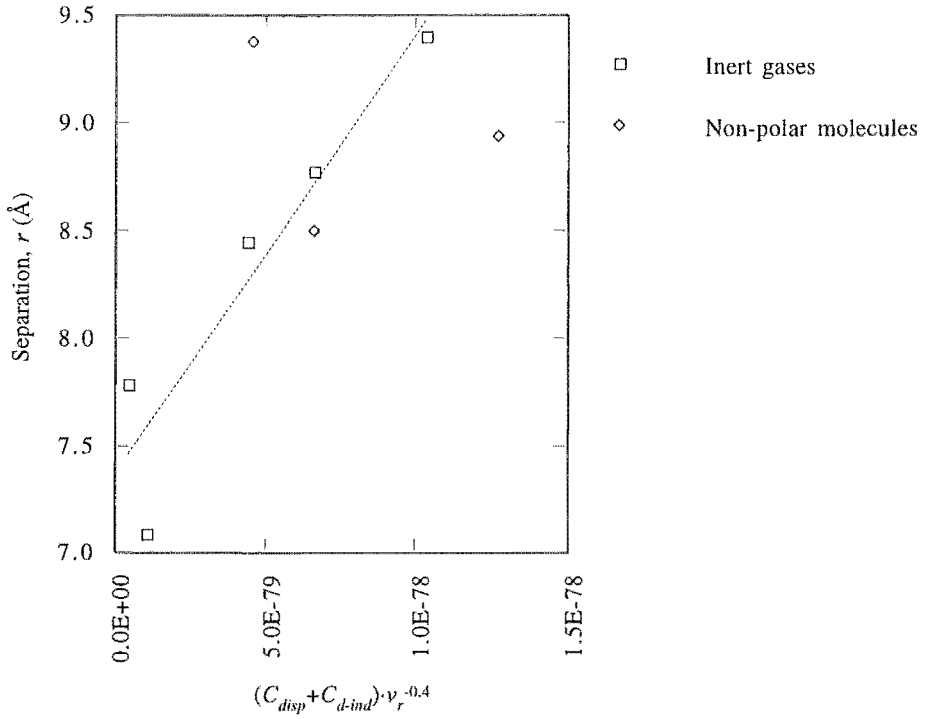

Figure 4.6 Correlation between interaction potential and CH_3Cl-quencher separation.

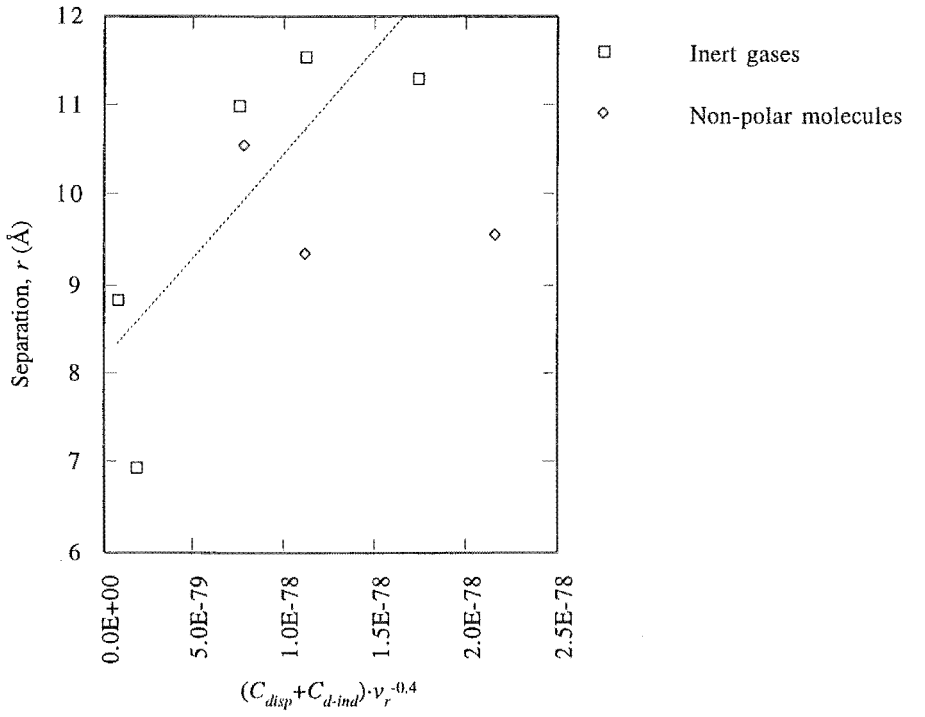

Figure 4.7 Correlation between interaction potential and seeded CCl_3H-quencher separation.

known to affect the ionisation gauge used to measure quencher pressure. In some cases the gauge must be left off overnight to allow the filament to degas.

Relaxation cross-sections for the polar quenchers N_2O, CH_3F and CH_3Cl on beams of CH_3Cl and 20% CCl_3H seeded in Ar are reported in Tables 4.4 and 4.5. A value for CCl_3H as a quencher on the seeded CCl_3H beam is also tabulated. Cross-sections for these quenchers are higher than for other quenchers having similar mass and polarisability, and a dipole-dipole interaction would account for this observation.

The van der Waals term for a dipole-dipole interaction is

$$C_{d-d} = \frac{2\mu_1^2\mu_2^2}{3(4\pi\varepsilon_o)^2 k\overline{T}_r} \qquad (4.15)$$

where $\overline{T}_r$ is the average rotational temperature of the two dipoles

$$\overline{T}_r = \frac{2T_{r,1}T_{r,2}}{T_{r,1}+T_{r,2}}. \qquad (4.16)$$

Equation 4.15 is known as the Keesom approximation and is applicable when the potential energy of the interaction is small compared with the energy of thermal motion, ie. $V << k\overline{T}$, where $\overline{T}$ is the average translational temperature of the collision species [Massey, 1969]. For a supersonic beam of CH_3Cl colliding with effusive CH_3Cl, $\overline{T}$ is calculated to be 371 K (§2.2). The separation for a cross-section of 443 Å^2 is 11.9 Å. At this distance the total van der Waals potential is 12.1 J mol^{-1} (refer below for a value of $\overline{T}_r$) while $k\overline{T}$ is 3 kJ mol^{-1}. The approximation only fails with strongly polar species such as CsCl where dipole locking becomes possible.

It is assumed that the rotational temperature of the quencher species is equal to the translational temperature of 298 K because of the effusive nature of the leak valve

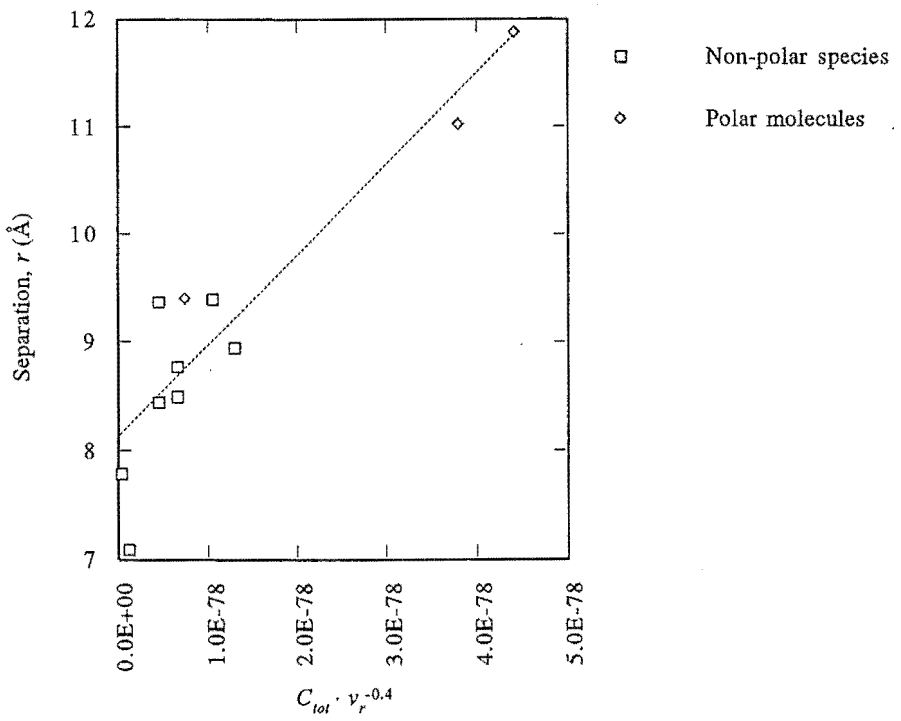

Figure 4.8 Correlation between interaction potential and CH_3Cl-quencher separation determined from relaxation cross-sections.

(§2.2.1). The rotational temperature of the beam species is not directly measurable in the present apparatus. However, the temperature $T_{r,1}$ can be found by linear-least squares analysis of the cross-section and $C \cdot v_r^{-0.4}$ data with $T_{r,1}$ as a variable. The temperature is adjusted to maximise the correlation coefficient, r, of the least-squares line. For CH_3Cl $T_{r,1}$ is found to be 130 K. It is not surprising that the correlation coefficient for 20% CCl_3H seeded in Ar is not improved by incorporation of the dipolar quenchers for any choice of beam temperature since there are large uncertainties in the appropriate cross-sections. Reasons for these uncertainties are discussed above. Figure 4.8 presents the data and line of fit for a CH_3Cl beam.

Good correlation between measured cross-sections and calculated van der Waals interactions is observed for CH_3Cl and a range of quenchers, and the cross-section results for seeded CCl_3H show the expected trend of increase with $C \cdot v_r^{-0.4}$. These comparisons are remarkable since relative velocity and beam and quencher rotational temperatures are estimates from theory or the fitting routine described above.

These results are the first measurements of symmetric top upper Stark state relaxation cross-sections. An attempt has been made to correlate the cross-sections with a simple long range attractive interaction, however, the relaxation process is likely to depend on a number of other parameters not considered here. It is hoped that future experimental and theoretical study will shed further light on the relaxation process investigated here.

4.3.2 Variation of relaxation cross-section with hexapole voltage

Discussion in §4.3.1.1 argues that experimental relaxation cross-sections are averaged over the cross-sections of individual states transmitted at the selected hexapole voltage. Filters can be designed to completely separate rotational states, however, the present device (for reasons given elsewhere) does not achieve this resolution. Instead, experimental transmission curves show 'bumps' on a increasing curve corresponding to the preferential transmission of a specific $|JKM\rangle$ state. However, these features are rapidly lost for curves measured with quencher present in the cell. This is interpreted in terms of the dependence of the relaxation cross-section on rotational state. At specific hexapole voltages the transmitted beam consists largely of molecules in a single rotational state, eg. $|111\rangle$, and a small percentage of other states. Where this is the case there is the possibility of estimating a state-to-states relaxation cross-section. It should be noted that the convention of expressing both K and M quantum numbers as positive integers is used here although for upper Stark states either M or K must be negative.

Transmission curves are measured for molecular beams of CH_3X (X = F, Cl and Br) with an Ar quencher at a range of quencher pressures as described in §4.2. Measurements are also reported for a beam of CH_3Cl with N_2 as the quencher. Relaxation cross-sections are extracted from the variation of beam intensity with quencher pressure for a range of hexapole voltages (§4.2.3). Figures 4.9 through to 4.11 present the cross-section data. For individual low-lying rotational states the

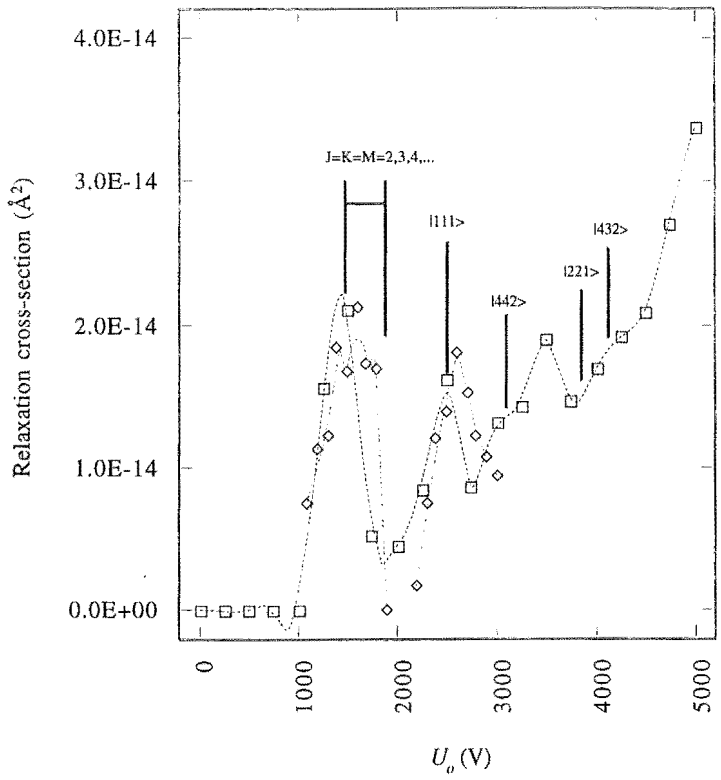

Figure 4.9 Variation of relaxation cross-section with hexapole voltage for CH_3Br with an Ar quencher.

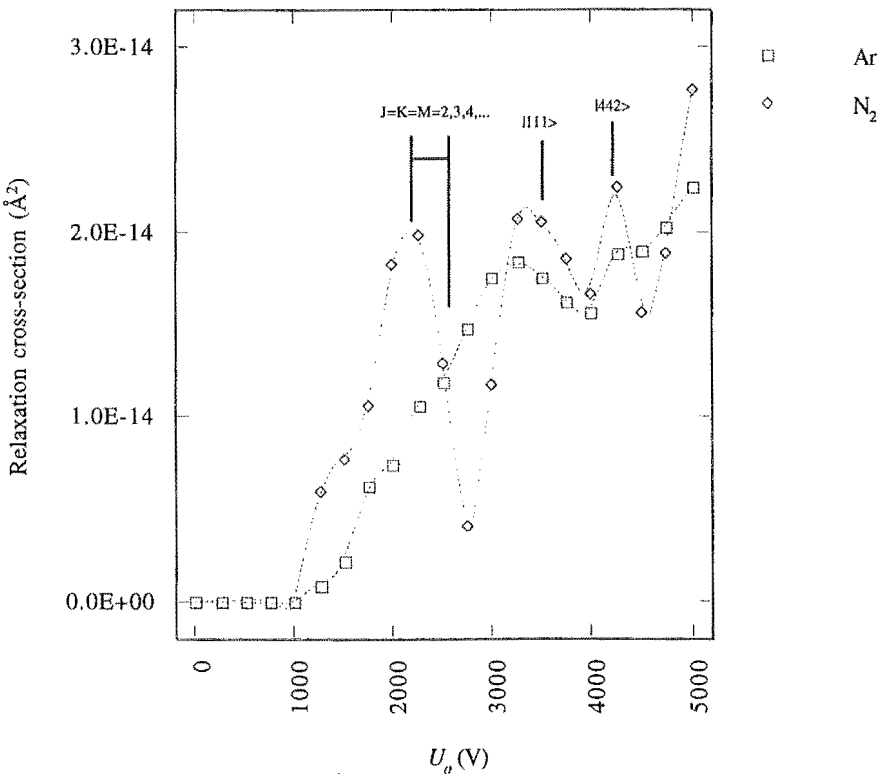

Figure 4.10 Variation of relaxation cross-section with hexapole voltage for CH_3Cl.

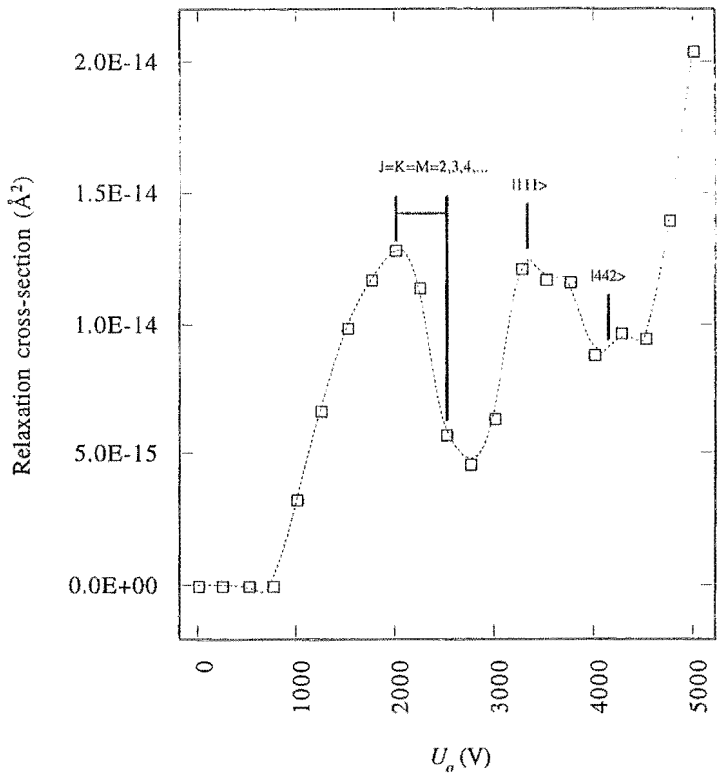

Figure 4.11 Variation of relaxation cross-section with hexapole voltage for CH_3F with an Ar quencher.

calculated voltages for which maximum transmission occurs are marked. Higher J states, where MK < J (J + 1) are not focused below 5 kV. These calculations are discussed in §4.3.2.2.

The correlation between features in the cross-section plots and calculated peak positions facilitates the assignment of measured cross-sections to individual states peaking at appropriate hexapole voltages.

Results are discussed in the following sections:

- general features and comparison with literature;
- calculation of transmission curves; and
- a discussion of correlations between simulated transmission curves and peaks in cross-section versus hexapole voltage plots.

4.3.2.1 General features and comparison with literature

Below 1 kV the probability of transmission of upper Stark state molecules is zero. The position of the threshold for $|JKM\rangle$ state transmission depends largely on the molecules' dipole moment. For the CH_3X series investigated here dipole moments lie in the range between 1.81 and 1.87 Debye. Equation 4.6 is used to calculate this threshold and agrees for a wide range of measured transmission curves. Cross-section results below this threshold are set to zero, as is explained in §4.2.3.

As the hexapole voltage is increased above the threshold, relaxation cross-sections show a general increase. Over the range of hexapole voltages available with this apparatus no asymptotic limit is reached.

Superimposed on the general increase of cross-section are a number of peaks, well defined at lower voltage but becoming more complex and smeared out at higher voltages. Peaks also broaden in going from CH_3Br through to CH_3F. In the case of CH_3Cl, peaks are better resolved by an N_2 quencher which has a higher density of states.

Results for each beam-quencher combination are averages of several experiments. Figure 4.9 also shows two peaks measured with greater accuracy. The peak positions ($\pm U_0$) are reproducible and afford confidence in the peak positions measured for other systems. Peaks in the plots of relaxation cross-section versus hexapole voltage are ascribed to the relaxation of individual $|JKM\rangle$ states, or at least a small number of $|JKM\rangle$ states, focusing under those conditions. A discussion of the positions of these peaks is presented in §4.3.2.3.

Calculations of the variation of relaxation cross-section with hexapole voltage are discussed in §4.3.1.1 [Phillips, 1995]. Basing calculations on the apparatus and

measurements reported here, Phillips investigates the complete methyl halide series and also CF_3Cl. Plots of relaxation cross-section against hexapole voltage resemble those reported here. There is correspondence between a number of the peaks in these plots and the experimental peaks, however, several significant differences exist.

Cross-sections are calculated to decrease with voltage. This may arise from the exclusion of J'→J'' transitions from Phillips' model (§4.3.2.3). A more alarming deviation from experimental observation are dominating peaks below the transmission threshold. In several cases there is an increase in cross-section with decreasing voltage that tends toward infinity. There is no physical explanation for this behaviour and it can only be interpreted as a failure of the model. This explanation is supported by the failure of the model to reproduce realistic hexapole transmission curves.

In conclusion, it is evident from the available models that the process of collisional relaxation and subsequent defocusing in an electrostatic filter is not fully understood and further theoretical and experimental work is desirable.

Following this section is a discussion of calculations that lead to a rationalisation of the observed cross-section peak positions in plots versus hexapole voltage.

4.3.2.2 Transmission curve calculations

The inhomogeneous electric field within the hexapole filter deflects symmetric top molecules by a radial distance that is inversely proportional to the angle made between the dipole of that molecule and the field direction (§2.4). This angle, θ, is fixed by the rotational quantum numbers J, K and M, and the expected value of cos θ is given quantum mechanically as

$$\langle \cos\theta \rangle = \frac{MK}{J(J+1)} \equiv \rho \qquad (4.17)$$

A detailed discussion of the hexapole filter is presented in §2.4. The probability of a molecule in state $|JKM\rangle$ being transmitted through the filter may be calculated for specified dimensions of the filter, including entrance and exit aperture positions and radii (§2.4.5 and below). In the ideal situation, where all molecules traverse the field with identical velocity and the entrance and exit apertures are infinitesimally small, a transmission 'curve' resembles a line spectrum with each peak corresponding to the transmission of molecules whose dipoles are fixed precisely at an angle, θ, to the electric field direction. In reality these conditions are not met and so the 'spectra' are smeared out. Not only is there width to the beam velocity distribution, but there is a finite probability of finding a molecules' dipole at an angle anywhere between 0 and 180° to the field direction [Choi and Bernstein, 1986].

Transmission curves are calculated for the apparatus described here using computer programs developed by Professor Philip Brooks of Rice University, Houston, Texas. A description of these simulations and the calculational procedure is given here.

A beam velocity distribution of the form given in equation 2.7 is calculated. Simpson's rule is then applied to the distribution for normalisation. The fraction of incident molecules transmitted by the filter is determined at each velocity, value of cos θ, and hexapole voltage by evaluation of equation 2.53. This array of values is reduced by integrating over the velocity distribution, giving

$$A(U_o,\rho) = \int_o^\infty A(U_o,v,\rho) f_v(v) dv, \qquad (4.18)$$

the fraction of incident molecules characterised by the cosine angle, ρ, that are transmitted at hexapole voltage, U_o.

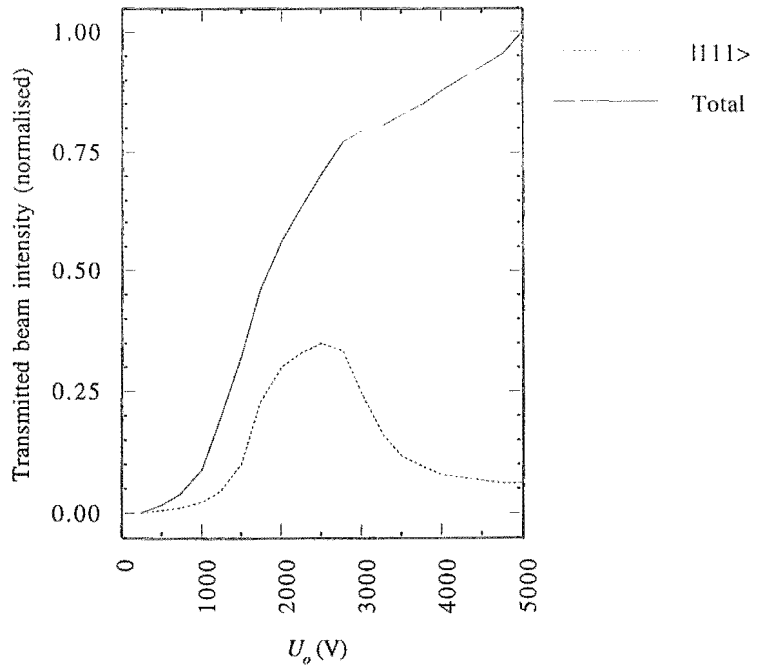

Figure 4.12 Simulated transmission curves for CH_3Br.

The transmission curve for an individual $|JKM\rangle$ state is determined by finding the expected value of ρ for that state and plotting the appropriate values of $A(U_o,\rho)$. This simulation of hexapole transmission does not evaluate the quantum mechanical expression for the *distribution* of ρ for each $|JKM\rangle$ state (equation 2.33). Including this expression in calculations allows a more accurate determination of transmission probability, however, computation time is prohibitive. For the purposes of this investigation, and the detail required from these calculations, inclusion of equation 2.33 is not necessary.

A total transmission curve, equivalent to that measured experimentally is calculated by integrating $A(U_o,\rho)$ over the initial rotational state population (equations 2.55 and 2.56). Examples of the output from this simulation are presented in Figure 4.12.

Nearly all of the parameters required for these calculations are known, either from the measurement of apparatus dimensions or from literature values of molecular constants. Experimental values for mean flow velocity and the translational and rotational

temperatures of a given molecular beam species are not known and must be identified by theory or a trial and error method.

Accurate values for translational temperature, $T_{\parallel}$, and rotational temperatures, T_J and T_K, are not important for this investigation. The translational temperature affects the width of calculated beam velocity distributions but does not significantly alter the mean velocity (§2.2.2). Total transmission curves lose structure if $T_{\parallel}$ is too large because of the relationship defined in equation 4.18. Calculations reported here assume a value of 1.8 K for the CH_3X (X = F, Cl and Br) beams. This temperature is equal to that measured for a beam of Ar by time-of-flight analysis with identical nozzle-skimmer arrangement [Cameron and Harland, 1991]. The true values of $T_{\parallel}$ for each of the three beam species will be larger and different, but not significantly. Conversion of random thermal motion to directed motion is very efficient for the nozzle stagnation pressures used here [Cameron and Harland, 1991].

Rotational temperatures, T_J and T_K, are required for calculating total transmission curves, specifically for the determination of the contribution made by each rotational state to the partition function. A procedure to identify the beam rotational temperature, T_r, from relaxation cross-sections is outlined in §4.3.1.3. For CH_3Cl the rotational temperature is found to be 130 K. This value is consistent with single beam studies of polyatomic jets where it is found that $T_r >> T_{\parallel}$ [Cameron and Harland, unpublished results]. However, calculated total transmission curves using this value for both T_J and T_K are smoother than those measured experimentally. This is interpreted as failure of the transmission simulation to accurately model the initial distribution of $|JK\rangle$ states entering the hexapole. Varying rotational temperature in calculations and comparing the total transmission curves with experimental results indicates $T_J = T_K = 10$ K to be a good choice for this simulation. It must be emphasised that the information sought from these simulations is the voltage at which transmission of individual $|JKM\rangle$ states is most likely.

Beam velocity significantly affects the peak positions for transmission of individual rotational states. The following method is adopted for determining mean flow velocities, u, for the methyl-halides investigated.

From a study of total transmission curves it is clear that the $|111\rangle$ rotational state is the second major feature above the transmission threshold. The voltages at which the second peak is observed in transmission experiments (Figures 4.9 to 4.11) are 3.25, 3.375 and 2.5 kV for CH_3X, X = F, Cl and Br respectively. Transmission of the $|111\rangle$ state is calculated for the three beams over a range of mean flow velocities to find the value where calculated peak positions match the experimental observations. Mean flow velocities of 686 m s^{-1}, 575 m s^{-1} and 358 m s^{-1} for CH_3X, X = F, Cl and Br respectively, are determined. The value of 575 m s^{-1} compares well with the value of 543 m s^{-1} measured in the machine by Cameron and Harland [Cameron and Harland, 1994]. This method is limited by the accuracy with which the experimentally observed peak is known, and by the accuracy of the transmission simulation. Figure 4.13 illustrates the effect of mean flow velocity on calculated peak transmission of the $|111\rangle$

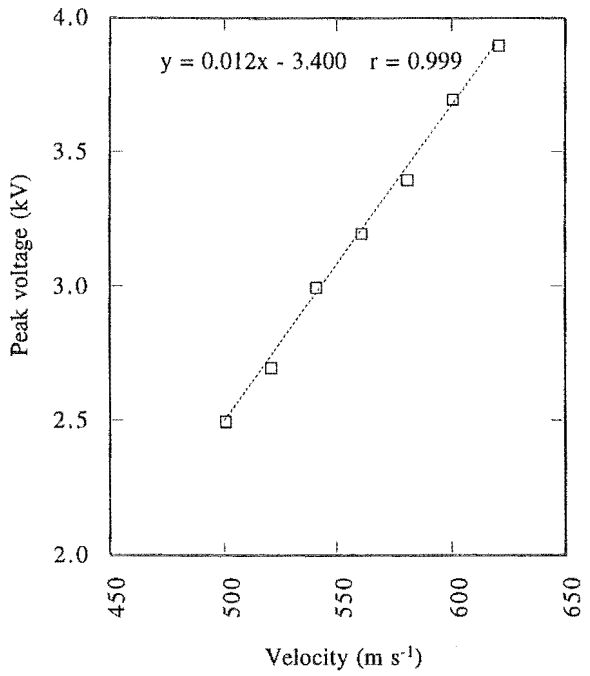

Figure 4.13 Calculated variation of CH_3Cl $|111\rangle$ state maximum transmission voltage with velocity.

state for CH_3Cl. A plot of the mean flow velocities for CH_3X species against the square root of the appropriate molecular mass, which is the expected dependence, yields a straight line by linear least-squares analysis with a correlation coefficient of 1.000. This is a good result for molecules that span a wide range of both calculated flow velocities and molecular masses.

Transmission curves are calculated for each beam for all rotational states, $J \leq 5$. The decision to truncate calculations at this point is a result of reasoning presented in §4.3.2. Table 4.7 lists the states that peak below $U_o = \pm 5$ kV for each beam.

State	CH_3Br	CH_3Cl	CH_3F
111	2.5	3.4	3.3
221	3.8	-	-
222	1.9	2.5	2.5
333	1.7	2.3	2.2
432	4.2	-	-
442	3.1	4.2	4.1
444	1.6	2.1	2.0
555	1.5	2.1	2.0

Table 4.7 Peak transmission voltages of $|JKM\rangle$ states (kV).

4.3.2.3 Discussion

Two conclusions may be reached after examining the results of the hexapole transmission simulations above:

- only low-lying J states *peak* at voltages investigated here (but see below)
- states where J = K = M form a progression of peaks from $|111\rangle$ at higher voltages to a limiting voltage where $J(J+1) \approx MK$.

Figures 4.9 to 4.11 clearly show a correspondence between cross-section maxima and the calculated maxima of transmitted rotational states.

A rationale for the above observation is as follows. The probability of defocusing upper Stark state molecules from the hexapole by a ΔM or ΔJ transition should be proportional to the resulting change in angle that the dipole makes with the electric field direction (eqn. 4.17). This is a reasonable assumption because the different angles, θ, for symmetric top molecules underlie the basis of hexapole state selection (§2.4). A $|111\rangle \rightarrow |110\rangle$ transition represents a change in angle of 30°. $\Delta M = -1$ transitions for J = K = M states where J = 5, 4, 3 and 2 correspond to changes in angle of 15, 16, 19 and 22°, respectively. Similarly large changes of angle result for the other states listed in Table 4.7. $\Delta J = -1$ transitions are not allowed for the J = K = M states because initially J = K and ΔK must be 0 by selection rules (§2.4). However, if a $\Delta J = +1$ transition were to occur for J = K = M states where J = 1-5 the changes in angle would be 20, 22, 22, 21 and 20°, respectively.

ΔM or $\Delta J = \pm 1$ transitions for states where both M and K are lower than J result in smaller changes of angle θ and would be expected to have lower cross-sections.

The measurements reported here are significant. A hexapole filter designed to transmit high intensities of upper Stark states with only moderate state separation is used to estimate state-specific relaxation cross-sections. The complex structure of cross-section versus hexapole voltage plots is qualitatively explained in terms of the change in the angle made between dipole and electric field following a ΔM or $\Delta J = \pm 1$ transition. Suggestions for further investigations are outlined in §6.

4.3.3 Elastic/inelastic collision cross-sections

Attenuation of the molecular beam by quencher gas in the scattering cell with the hexapole switched off is the result of elastic and inelastic collisions. The contribution of these collisions to the attenuation of beam intensity with the hexapole on is

deliberately removed to determine relaxation cross-sections (§4.1.3). However, a collision cross-section for these processes may be calculated by application of the Beer-Lambert law (equation 4.3) to beam intensity data, $I_{o,P}$. Table 4.8 presents results for a beam of CH_3Cl with non-polar quenchers.

Quencher	σ (Å^2)	$\pm$ (Å^2)	Measurements
He	108	6	9
Ne	92	5	9
Ar	133	8	9
Kr	176	12	9
Xe	207	12	9
N_2	166	10	9
SF_6	216	12	9
CO_2	160	6	9

Table 4.8 Elastic/inelastic collision cross-sections for a beam of CH_3Cl.

Separation of the elastic and inelastic processes is not possible with the present apparatus, and in any case, these results are a byproduct of the method for determining relaxation cross-sections. Despite this limitation the cross-sections may be interpreted with reference to the same van der Waals interaction potential described in §4.2.3. Figure 4.14 is a plot of $C \cdot v_r^{-0.4}$ against the separations corresponding to measured cross-sections. Good correlation between the calculated interaction potential and cross-sections is observed, and is rationalised in the following manner.

For a beam molecule traversing the cell, an angle, α, is made between the velocity vector and the circumference of the exit aperture. It is through this minimum angle that the molecule must be deflected before being considered lost to the detector. This is a simplification and the details are discussed below. Energy for the required change in momentum comes from the electric field established by an approaching quencher. A stronger interaction facilitates sufficient energy transfer for deflection through angle α at larger distances, with a higher cross-section as a direct consequence. The theory of

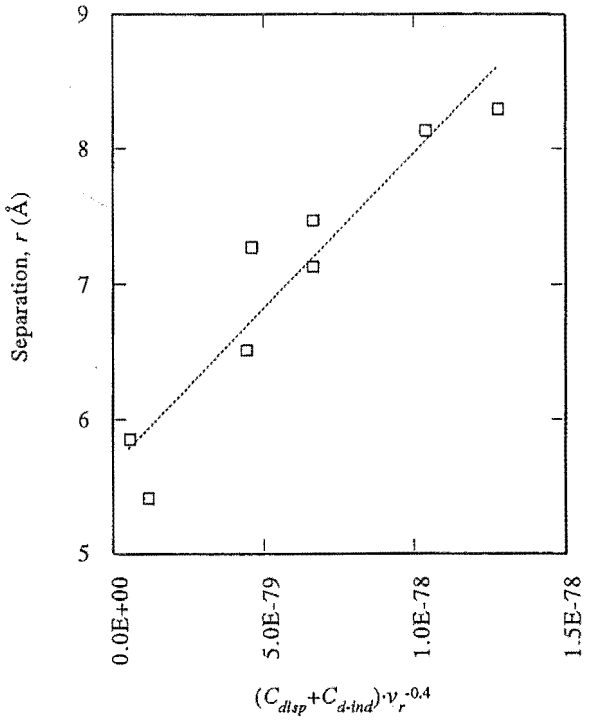

Figure 4.14 Correlation between interaction potential and CH_3Cl-quencher separation determined from elastic/inelastic cross-sections.

elastic and inelastic collision processes is well documented and supports this reasoning [Massey, 1969].

In general, the measured cross-section could be expected to increase with decreasing exit aperture radius toward some limiting value, or the *total* collision cross-section. Classical mechanics fails to predict this limit but because of the quantisation of energy there is a minimum non-zero transfer of momentum. The ability of an experimental apparatus to measure total collision cross-sections is characterised by its' angular resolution. Total collision cross-section experiments normally employ a scattering cell that is short relative to the beam source-detector distance and placed close to the beam source. The angle α is defined between the beam axis and detector entrance aperture. Typically this is 10' and changes little over the length of the cell. Higher resolution, or smaller angle α is necessary in order to measure accurate total collision cross-sections of heavier beam and quencher species. The minimum angle of deflection is reduced with increasing mass.

Angular resolution for the apparatus here is much lower and more difficult to determine than that described above. The detector is close to the end of the cell and angle α varies considerably through the cell length. For a molecule traversing the cell, the limiting aperture is the exit aperture until it approaches within 6 cm and then the detector aperture makes the greater angle through which deflection must occur. Assuming beam-quencher collision probability is equal along the beam axis then the average angular resolution of this apparatus is found to be 37'. However, a molecular beam diverges and on-axis intensity falls off as 1/r. Beam-quencher collision probability will be higher nearer the beam source. In the first quarter length of the scattering cell, angle α is 9', increasing to 13', 22', and 1°44' in successive lengths. The average angular resolution of this apparatus is therefore likely to be significantly better that 37'.

Some modification of the apparatus would be required if the determination of accurate total elastic/inelastic collision cross-sections of heavy beam-quencher combinations was desired.

Chapter 5

Electron Impact Ionisation Asymmetry

5.1 Introduction

Experiments to explore the possibility of orientation asymmetry of electron impact ionisation for the symmetric top molecules CH_3Cl, CH_3Br, CF_3Br and CCl_3H are discussed here. The choice of symmetric top molecules is necessitated by the state-selection and orientation methods employed. Further, insight into the initial step of electron transfer in alkali metal-alkyl halide reactions was one of the fundamental motivations for this work (§1).

Selection of methyl chloride is due to its high beam intensities and good hexapole focusing characteristics. Despite the calculated degree of orientation for CH_3Cl (§2.4.3) being somewhat lower than for CF_3Br and CCl_3H, higher nozzle stagnation pressures and its larger hexapole focusing effect result in excellent signal-to-noise ratios.

Two different ion detectors are employed in an effort to maximise signals for a range of both light (fast) and heavy (slow) molecules. The Amptektron thermal ion detector (§3..8.1) is suitable for CH_3Cl and Ar detection while for slower species, such as

CH_3Br, CF_3Br, and CCl_3H, a mass selective detector (§3.8.2) is necessary to eliminate background signal interferences. Additionally, the mass filter allows investigation of fragment ion formation as a function of molecular orientation. It is noted both here and in §3 that the mass filter and Amptektron units were subject to repeated failure. Data was collected from the most suitable detector operating at the time while every attempt was made to repair the faulty components.

During the course of investigation the hexapole rods were remounted closer together (inscribed radius, r_o, going from 7.35 mm to 5.88 mm). Twenty percent lower rod voltages to achieve the same field strengths reduce the possibility of discharge across the hexapole mounts. Data for different r_o values is compared and shown to be consistent with the resulting change in orientation distribution (see §2.4.5 and §2.4.6).

Following a description of the experimental configurations and the data analysis procedure, results are reported in four separate sections:

- initial asymmetry effect observed for total ion count (TIC) or molecular ion count of Ar, SF_6, CF_3Br, CCl_3H, CH_3Br and CH_3Cl at 200 eV;

and then the asymmetry effect as a function of

- electron energy (TIC) for CH_3Cl;
- fragmentation for CH_3Cl, CH_3Br, CF_3Br and CCl_3H; and
- hexapole voltage (TIC) for CH_3Cl.

Experiments to validate the observed asymmetry effects are detailed in §5.5 and a theoretical model of the effects is presented in §5.6.

5.2 Experimental configuration

The molecular beam apparatus constructed for these experiments is illustrated in Figure 5.1. A pulsed supersonic beam of symmetric top molecules is formed from the nozzle. The repetition rate is fixed at 10 Hz by the beam source driver (BSD) and each pulse of gas is ~1 ms wide (§3.4). This pulse evolves over time, because of the distribution of velocities in the beam, reaching the scattering chamber as a pulse ~1.5-2 ms wide at half maximum.

The beam enters a hexapole filter, where upper Stark state molecules are focused through an exit aperture into the scattering chamber, while lower Stark state molecules are defocused and lost from the beam (§2.4). Upper Stark state molecules make an adiabatic transition into a 20 V cm^{-1} homogeneous electric field maintained between parallel field plates (§3.9). The field defines a laboratory axis about which the state selected molecules orient. Upper Stark state molecules are oriented with dipoles directed against the field direction, that is, the positive end of the dipole is directed toward the positive field. An electron beam intersects the oriented molecule beam near the end of the homogeneous field region (§3.7). The polarity of the field is set to present either the positive-end of molecules to the approaching electrons or the negative-end of the molecules. Field direction may be reversed as described in §3.9 and §5.3.

Ions formed by electron impact ionisation in the field region are accelerated by the field and lost to the plates. However, the homogeneous field is switched from 20 to ±0.1 V cm^{-1} as the pulse of beam molecules traverses the field region enabling ions to drift toward the detection system (see below). Two ion detectors are used for this work: the Amptektron thermal ion detector (§3.8.1); and a quadrupole mass filter with an electrostatic ion lens (§3.8.2). Reasons for the use of two detectors are given in §3.8.2. Figure 5.1 shows the detector configurations for these experiments.

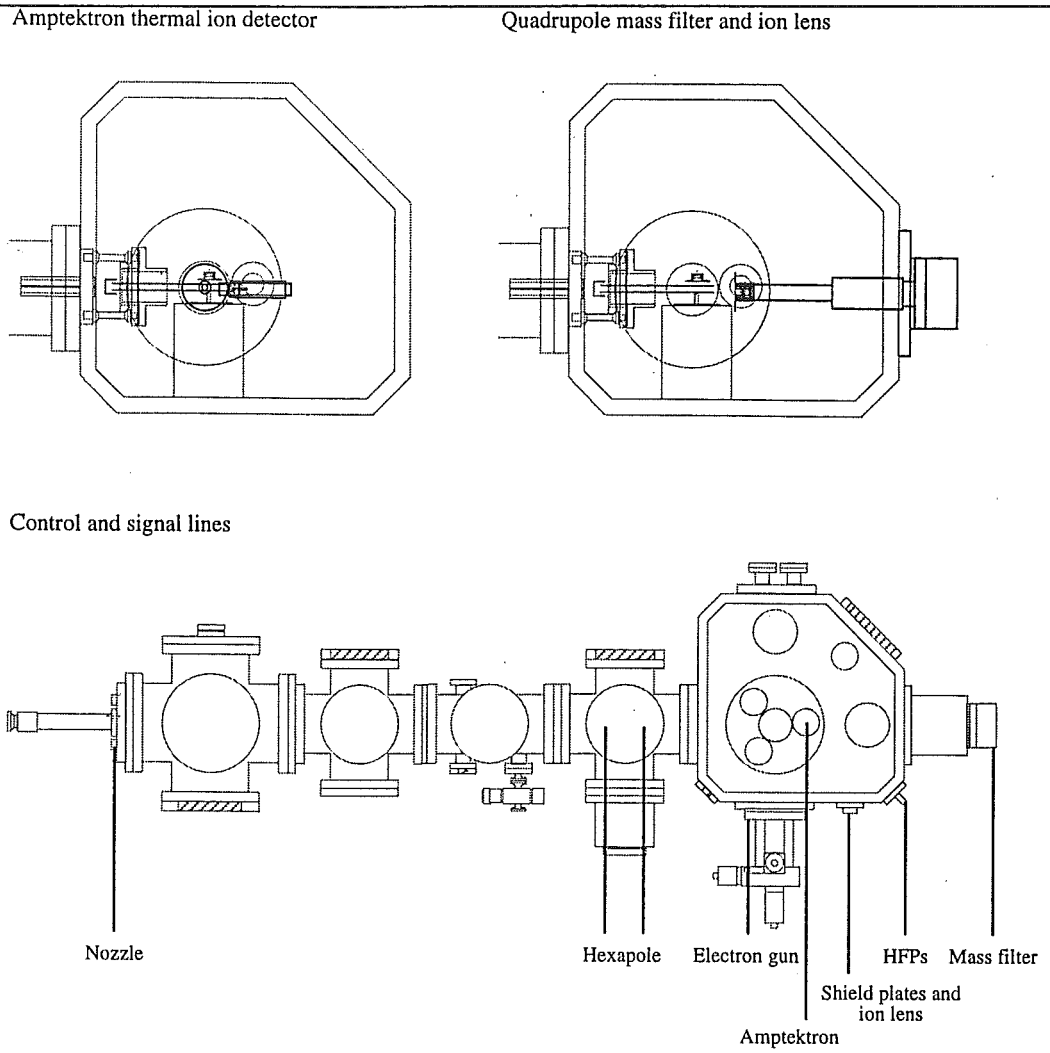

Figure 5.1 Experimental apparatus.

The timing of field switching and beam detection is illustrated in Figure 5.2. To summarise, the beam source driver (BSD) and homogeneous field plate pulsing unit (HFPPU) are triggered by the pulse counting control unit (PCCU). After a time, $delay_1$, when the maximum number of state-selected molecules are oriented, the field amplitude is switched to a value of ~0.1 V cm^{-1} over a period of ~0.1 ms, which is short compared with the residence time of molecules in the field region. Ions formed after this switching drift toward the detector in the space of 0.1 ms and are counted under gate 1 after a time, t_1, and under gate 2 at a time, t_2. The gate 1 signal is a combination of ionised background and oriented beam molecules while gate 2 is a combination of ionised background and state-selected (but not oriented) beam molecules. The field is

restored after a time, $delay_2$, until the HFPPU is triggered again by the PCCU and the sequence is repeated.

The widths of gate 1 and 2 are equal and chosen to maximise the collection of signal produced from the ionisation of oriented molecules during the time period corresponding to gate 1. The average time a molecule spends in the homogeneous field region is calculated from arrival time distributions and the field-ionisation region length (160 mm). For CH_3Cl the width, w, is set to 0.3 ms. Gate 1 is positioned a time, t_1-

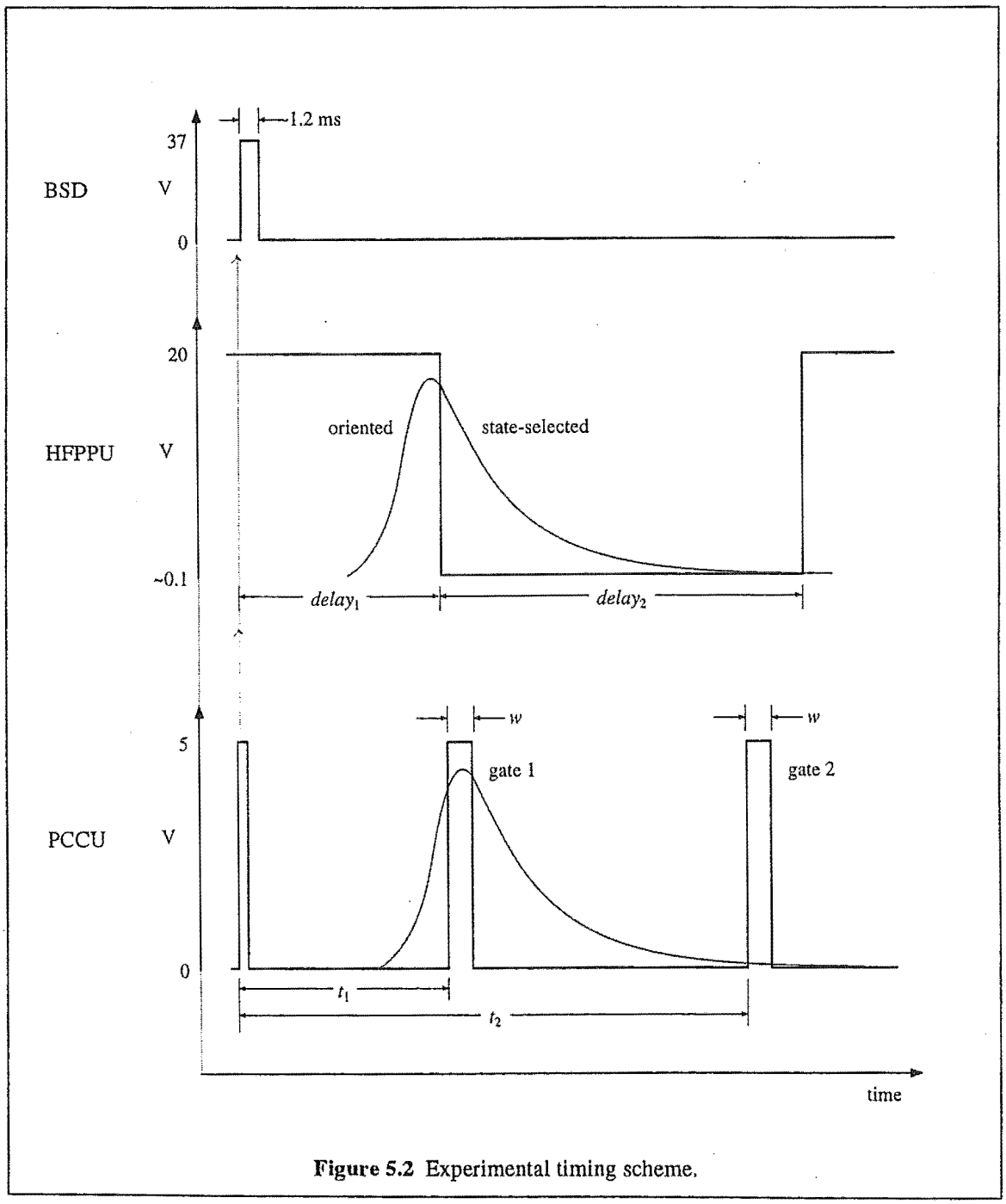

Figure 5.2 Experimental timing scheme.

$delay_1$, after the field is switched off, corresponding to the drift time of ions from the electron-molecule beam intersection to the detector. The ions are gently accelerated by field penetration from the detector and the drift time is in the order of ~0.1 ms. Gate 2 is placed as far along the arrival time distribution tail as is permitted by the PCCU, normally 9.9 ms after the nozzle is opened.

5.3 Data acquisition and analysis

Figure 5.1 shows the two detector configurations (for more detail refer to §3.8.1 and §3.8.2), hexapole control and signal processing lines. Electron energy and mass (for quadrupole experiments) are set manually.

The experimental sequence to determine an asymmetry effect for electron impact ionisation is independent of the detector used. For a given molecule, electron energy and hexapole voltage (and mass if applicable) the following measurements are made:

- Hexapole is switched on to voltage, $\pm U_o$. Field plates are biased so that the positive-ends of molecules are directed toward the electron beam. Signal from the PCCU is recorded as $\delta_{+,HV}$ = gate 1 - gate 2.
- Hexapole is switched off while field plates remain biased in a similar fashion. Signal is recorded as $\delta_{+,o}$ = gate 1 - gate 2.
- Field plates biasing is reversed so that the negative-ends of molecules are directed toward the electron beam. Hexapole voltage is set again to $\pm U_o$. Signal is recorded as $\delta_{-,HV}$ = gate 1 - gate 2.
- Hexapole is switched off while field plates remain biased in a similar fashion. Signal is recorded as $\delta_{-,o}$ = gate 1 - gate 2.

Each signal, δ, is the average of three consecutive measurements made for an interval t_c. The count rate (per second) for a signal, δ, is given by

$$\delta^* = \frac{\delta}{t_c w f}, \tag{5.1}$$

where w is the gate width and f the nozzle pulsing frequency. Typical values measured on the Amptektron for CH_3Cl with the hexapole off are 2800 s^{-1}. The time interval t_c is set to between 60 and 200 seconds in order to accumulate sufficient counts for reliable analysis.

Ideally the values of $\delta_{+,o}$ and $\delta_{-,o}$ are equal, corresponding to identical ion collection efficiencies for the two field directions. However, this is almost never the case due to the residual HFP fields of ± 0.1 V cm^{-1} and any stray fields resulting from contact potentials and surface contamination. The ratio

$$F = \frac{\delta_{-,o}}{\delta_{+,o}} \tag{5.2}$$

is defined and signals $\delta_{+,o}$ and $\delta_{+,HV}$ are multiplied by it to correct for the differing collection efficiencies:

$$\delta'_{+,o} = \delta_{+,o} F \tag{5.3}$$

$$\delta'_{+,HV} = \delta_{+,HV} F. \tag{5.4}$$

Reliability of an asymmetry result requires the ratio F to be close to unity especially when the signals, δ, are small. When F consistently deviates from unity by more than 0.4 the vacuum system is shut down and surfaces in and around the homogeneous field region are cleaned. Immediately after cleaning $F = 1$, deviating from this value as time goes on.

The signals arising from ionisation of oriented molecules for each field direction are given by:

$$D_{+}^{'} = \delta_{+,HV}^{'} - \delta_{+,o}^{'} \tag{5.5}$$

$$D_{-} = \delta_{-,HV} - \delta_{-,o}. \tag{5.6}$$

Two different representations of the asymmetry effect are defined:

- A steric ratio

$$R = \frac{D_{+}^{'}}{D_{-}} \tag{5.7}$$

where, for ionisation favouring the molecules' positive-end, $R > 1$, and favouring the negative-end, $R < 1$. In the case of no asymmetry effect $R = 1$; and

- A G-factor where

$$G = \frac{D_{-} - D_{+}^{'}}{D_{-} + D_{+}^{'}} \tag{5.8}$$

which lies between the bounds $-1 \leq G \leq 1$, and is positive when $R < 1$ and negative when $R > 1$.

The significance of a measured asymmetry effect is dependent on the magnitudes of $D_{+}^{'}$ and D_{-}. Every attempt is made to maximise these values by choosing longer counting times, t_c, and increasing the nozzle stagnation pressure. Hexapole voltage is selected to

give greatest enhancement of beam signal while avoiding an electrical discharge. A value of ±5.5 kV (for the hexapole of inscribed radius r_0 = 5.88 mm) increases the beam intensity of CH_3Cl 1.4 times. Other symmetric top molecules examined here have different hexapole transmission characteristics and these are indicated in the appropriate results sections §5.4.1 and §5.4.3. Signal levels vary greatly with electron energy, principally due to the changing electron beam flux but also variation in the electron impact ionisation cross-section. Asymmetry results are not reported for electron energies below 100 eV where count rates for CH_3Cl with the hexapole off are less than 200 s^{-1}. Increasing the counting time beyond 200 s is not feasible because of the time for which cryogenic pumping maintains background pressure at the required levels (usually 40-50 minutes).

Electron current at the Faraday cup is recorded by a Keithley picoammeter (model 486). This current is a useful measure of electron beam intensity when both field plates are set to ground potential. During asymmetry experiments the average current changes because of the pulsing electric field between the electron gun and Faraday cup. This current is kept constant for an experiment by adjusting the electron gun filament supply.

Nozzle stagnation pressure is measured with an MKS Baratron capacitance manometer and control unit (§3.3). Over the duration of a single experiment the nozzle stagnation pressure remains constant, due to the low leak rate through the nozzle and high sample reservoir capacity (three litres).

5.4 Results

5.4.1 Initial results for 200 eV electrons

Asymmetry effects are observed for the ionisation of CH_3Cl, CH_3Br, CF_3Br and CCl_3H at 200 eV and the initial observations are discussed here. Table 5.1 summarises the important experimental conditions and settings, while others such as the mass spectrometer ion lens and electron gun element voltages are detailed in §3.

	Ar	SF_6	CH_3Cl	CH_3Br	CF_3Br	CCl_3H
Nozzle						
stagnation pressure (torr)	1500	2125	1000-2300	1125	1700	190
open time (ms)	1.2	1.2	1.2	1.2	1.2	1.2
nozzle voltage (V)	37	37	37	37	37	37
skimmer distance (mm)	17.5	17.5	17.5	17.5	17.5	17.5
aperture radius (μm)	35	35	35	35	35	35
HFPPU						
$delay_1$ (ms)	3.4	4.5	3.4	5.1	4.4	4.6
$delay_2$, (ms)	7.0	7.0	7.0	7.0	7.0	7.0
V_{on}, (V)	20	20	20	20	20	20
V_{off}, (V)	~0.1	~0.1	~0.1	~0.1	~0.1	~0.1
PCCU						
t_1 (ms)	3.5	4.6	3.5	5.2	4.5	4.7
t_2 (ms)	9.7	9.9	9.9	9.7	9.7	9.7
w (ms)	0.3	0.5	0.3	0.5	0.5	0.5

Table 5.1 Important experimental conditions and settings for measurement of asymmetry effects at 200 eV.

Measurements of both total ion count (TIC) using the Amptektron thermal ion detector and specific ion count (SIC) from the quadrupole mass spectrometer are combined in Table 5.2. The appropriate hexapole voltage, inscribed radius, and calculated cosine of the average angle of orientation are noted alongside each set of values for later reference.

	Hexapole	$\langle\rho\rangle_{calc}$	G	R
Total ion count (Amptektron)				
CH_3Cl	±5.5 kV, r_0 = 5.88 mm	0.31	-0.101±0.081	1.23
	±10 kV, r_0 = 7.35 mm	0.29	-0.269±0.111	1.70
Ar	" "	-	0.041±0.206	0.96
SF_6	" "	-	~0	~1
Specific ion count (mass spectrometer)				
CH_3Cl (CH_3Cl^+)	±5.5 kV, r_0 = 5.88 mm	0.31	-0.476±0.117	2.80
CH_3Br (CH_3Br^+)	" "	0.28	-0.085±0.117	1.21
CF_3Br (CF_3^+)	" "	0.54	-0.219±0.219	1.80
CCl_3H (CCl_2H^+)	" "	0.48	-0.170±0.082	1.36
Ar (Ar^+)	" "	-	0.006	0.99

Table 5.2 Electron impact ionisation asymmetry results measured at 200 eV.

A first glance at the results in Table 5.2 reveals that all G-factors for symmetric top species are *negative* indicating that ionisation of those molecules is preferred on the positive-end of the dipole. Additionally, the spherical molecules Ar and SF_6 show no apparent asymmetry effect under identical experimental conditions. Beyond these two observations little can be seen without some explanation.

Firstly, consider the three sets of values given for CH_3Cl. Measurements of CH_3Cl (total ion count) using different hexapoles lie within one standard deviation of each other. Assuming that any asymmetry effect is at a maximum when $\langle\rho\rangle = 1$ then it could be expected that the mean G-value for r_0 = 5.88 mm be *higher* than that for r_0 = 7.35 mm. The fact that this is not observed is probably due to two factors: the

small change in degree of orientation resulting from the use of different hexapoles (about one degree); and the magnitude of both standard deviations. When measuring the signal of the mass selected CH_3Cl^+ ion the mean asymmetry effect is much higher. This is rationalised by considering the electron impact ionisation fragmentation of CH_3Cl. At 70 eV the fragment ion CH_3^+ ion is formed at 30% of the intensity observed for CH_3Cl^+. At higher energies the degree of fragmentation could be expected to be higher. If the formation of CH_3^+ ion is not enhanced by either CH_3-end or Cl-end impact then the difference between observed molecular ion and total ion asymmetry effects is explained. It is shown in §5.4.3 that this is indeed the case with fragmentation favoured by broadside electron-molecule interactions.

Errors for the measurement of CH_3Br asymmetry are large. Despite a hexapole enhancement of 1.3 times the *D*-values used to determine both the *G*-factor and *R* value are smaller than those for CH_3Cl. Methyl bromide has a low vapour pressure which limits the maximum nozzle stagnation pressure to 1125 torr, and its' higher mass (lower velocity) reduces detection efficiency (§3.8.1 and §2.7). Detection of CH_3Br ion products with the Amptektron device is not feasible because of these two factors.

The magnitude of the mean *G*-factor for CH_3Br is near to zero which may result from errors of measurement rather than any physical explanation. Both methyl bromide's dipole moment and calculated degree of orientation are similar to those of CH_3Cl. Further measurements are required to determine the asymmetry effect more precisely. The asymmetry of CH_3^+ fragment ion formation from CH_3Br is discussed in §5.4.3 though for the above reasons errors associated with those measurements are high.

Electron impact ionisation of both CF_3Br and CCl_3H lead to formation of fragment ions (CF_3^+ and CCl_2H^+ respectively) and not molecular ions. The process of fragmentation is detailed in §5.4.3, however, the main points are summarised here. An electron is ejected during the initial ionisation process. Energy is redistributed within the

molecular ion into the available modes of vibration and rotation. If the energy contained in one mode is enough to overcome the attractive force of the corresponding potential surface then dissociation occurs. The negative G-factors for CF_3Br and CCl_3H suggest that the initial interaction and electron ejection is at the positive end of both molecules. Fragmentation occurs because of the instabilities of the molecular ions.

A large G-factor standard deviation for CF_3Br results from its low detection efficiency. On the other hand, the low vapour pressure and detection efficiency of CCl_3H is compensated by its large hexapole focusing effect (1.9 times at ±5.5 kV). The relatively high calculated degree of orientation may also account for the magnitude of the observed effect.

5.4.2 Electron energy dependence

The incident electron energy dependence of the measured asymmetry effect for CH_3Cl is reported here. Important conditions and settings differ slightly from those in the previous section and are listed in Table 5.3. A different supersonic nozzle used for these experiments requires higher opening voltages and as a result the arrival time distribution is delayed by approximately 0.4 ms. Electron gun element voltages are optimised to give the most well defined and narrow of beams for each electron energy (§3.7). Signal is collected with the Amptektron thermal ion detector (§3.8.1).

Nozzle	
stagnation pressure	1300-2000 torr
open time	1.4 ms
open voltage	46 V
skimmer distance	17.5 mm
aperture radius	35 μm
HFPPU	
$delay_1$	3.8 ms
$delay_2$	7.0 ms
V_{on}	+20 V
V_{off}	~+0.1 V
PCCU	
t_1	3.9 ms
t_2	9.9 ms
w	0.3 ms
Hexapole (r_o = 5.88 mm)	±5.5 kV

Table 5.3 Important experimental conditions and settings for measurement of the CH_3Cl asymmetry effect as a function of electron energy.

Results for four electron energies are listed in Table 5.4. Limits are placed on the range of energies examinable for two reasons. The electron beam density is roughly independent of electron energy, however, beam flux is proportional to the energy or electron velocity. Lowering electron energy reduces the rate of ionisation because fewer electrons traverse the molecular beam per unit time. This effect is taken into account for the asymmetry analysis used here (§5.3). When the ionisation rate falls off to the extent that the D-values of eqns. 5.5 and 5.6 become small, then the resulting asymmetry G-factor and R ratio are no longer significant. An upper limit to electron energy is determined by the electron gun dimensions and available power supplies.

Electron energy (eV)	*G*	*R*
100	-0.106±0.012	1.24
150	-0.153±0.115	1.36
200	-0.101±0.081	1.23
240	-0.182±0.114	1.45

Table 5.4 CH_3Cl electron impact ionisation asymmetry results for different electron energies.

Over the range of electron energies listed in Table 5.4 there appears to be a small increase in asymmetry effect at higher energies. The energy dependence of an electron impact ionisation asymmetry effect is rationalised in terms of three phenomena. Figure 5.3 shows an uncalibrated plot of ionisation cross-section against energy for CH_3Cl measured with the quadrupole mass spectrometer configured with its' own ion source (§3.8.2).

At near-threshold energies the electron 'wavelength' is long compared with the size of CH_3Cl. The phase of the electron-molecule wavefunction is unaltered by a change in orientation. Ionisation should be independent of orientation where this is the case. This is quite different from a dual-particle interaction where the near-threshold orientation effect is at a maximum [Xing, 1994]. The particles' wavelength is short and the wavefunction for the interaction depends on the phase of the individual wavefunctions. As electron energy increases, electron wavelength decreases. At 70 eV the wavelength is very similar to the size of CH_3Cl. The combined wavefunction will depend on molecule-electron orientation and an asymmetry toward ionisation will exist. As electron energy increases and wavelength decreases the asymmetry effect might be expected to increase as suggested in Table 5.4, although other factors may well mitigate such an effect. Increasing energy further results in a decrease in total ionisation cross-section. The interaction time, as electron velocity increases, falls with a corresponding decrease in transition probability (§2.6). However, this is no reason for a lower asymmetry effect.

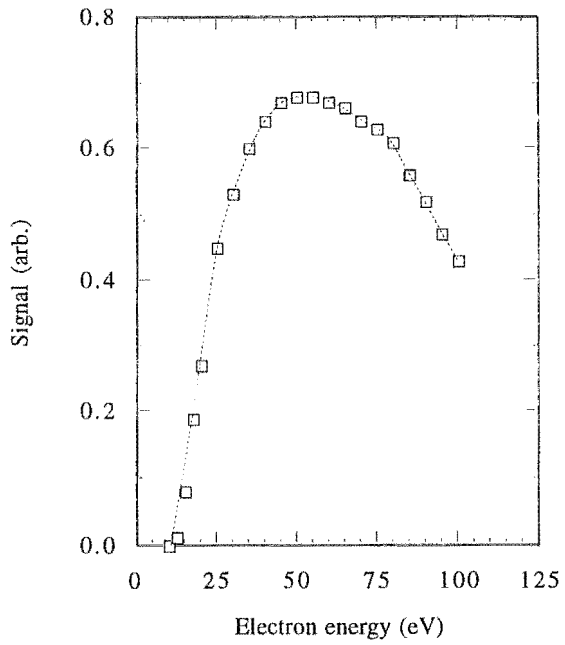

Figure 5.3 Ionisation efficiency curve for mass selected CH_3Cl^+.

There is the possibility of an asymmetry effect being limited at higher energies due to the interaction distance at which ionisation can occur. At higher energies the fraction of the electrons' translational energy required for ionisation is lower. The particle-like electron need only graze the molecule for this energy transfer. At larger distances the electron progressively samples more of the molecule during approach with a resulting averaging of the cross-sections for ionisation at the positive and negative ends of the molecule. However, the contribution of these encounters to successful ionisation is small because low transition probability at high electron energies necessitates a closer approach. This is reflected in a lower total ionisation cross-section.

Böwering, *et al.* report differences in 1 keV electron diffraction patterns off oriented CH_3Cl [Böwering, 1994]. This study suggests that orientation asymmetry for electron-molecule interactions does not vanish at high electron energy.

5.4.3 Fragment ions

Experimental conditions are listed in Table 5.1. Signal is collected with the quadrupole mass spectrometer. Additionally, the hexapole voltage for all measurements discussed here is set to ±5.5 kV (r_o = 5.88 mm) and electron energy is 200 eV.

Molecule	Ion	$\langle\rho\rangle_{calc}$	G	R
CH_3Cl	CH_3Cl^+	0.31	-0.476±0.117	2.80
	CH_3^+	"	0.017±0.033	0.96
CH_3Br	CH_3Br^+	0.28	-0.085±0.117	1.21
	CH_3^+	"	0.103±0.542	1.04
CF_3Br	CF_3^+	0.54	-0.219±0.219	1.80
CCl_3H	CCl_2H^+	0.48	-0.170±0.082	1.36

Table 5.5 Electron impact ionisation asymmetry results for molecular and fragment ions measured at 200 eV.

Perhaps the most compelling evidence for the existence of an asymmetry effect comes from the study of specific ion formation. Table 5.5 quite clearly shows that, certainly for CH_3Cl, the asymmetry effect disappears for the fragment CH_3^+ ion. Experimentally the only change is within the mass filter, well away from the orienting field and electron-molecular beam interaction region. For CH_3Br the difference is less startling, this is probably due to the low signal levels.

The probability of ionisation is proportional to the overlap of electron and appropriate molecular wavefunctions. Molecular wavefunctions can be thought of as the combination of atomic orbital wavefunctions. A study of ionisation potentials in relation to the fragmentation of NH_3 is useful at this stage. The ground state valence electron configuration of NH_3 is $[s]a^2[\pi]e^4[z]a_1^2$, where the letter in square brackets describes the molecular orbital and the letter to the right is the irreducible representation of the C_{3v} point group to which the orbital belongs. The first ionisation potential at

10.52 eV produces NH_3^+ (no fragmentation) by the removal of one of the [z]a_1 electrons localised around the nitrogen atom. The fragment NH_2^+ appears at 15.8 eV which must result from the second ionisation potential, or removal of a [π]e electron. Both [s] and [π] orbitals are localised about the N-H bonds [Massey, 1969].

Fragmentation of CH_3X species may be thought of similarly. Molecular ion formation occurs following ejection of an electron localised on the CH_3-end of the CH_3X molecule, maybe from an antibonding orbital. A second ionisation potential leading to fragmentation corresponds to ejection of an electron localised about the C-X bond [Maclagan, unpublished results]. Broadside approach of the electron will favour this fragmentation process while the heads and tails orientations should be similar with respect to fragmentation probability, as is observed here.

Arguments for the observed orientation asymmetry of CF_3^+ and CCl_2H^+ fragments follow easily. The orbital from which the electron is ejected lies on the positive end of both molecules, and the excited molecular ion dissociated after redistribution of the excitation energy.

5.4.4 Hexapole voltage dependence

Experimental conditions relevant to CH_3Cl are listed in Table 5.1 with the exception of nozzle stagnation pressures which range between 1600-2200 torr for measurements discussed here, and electron energy which is fixed at 200 eV. Signal is collected with the Amptektron thermal ion detector and the hexapole has an inscribed radius r_o = 7.35 mm.

Hexapole voltage (± kV)	$\langle\rho\rangle_{calc}$	G	R
6	0.37	-0.069±0.248	1.24
8	0.31	-0.199	1.50
9	0.29	-0.221±0.123	1.57
10	0.29	-0.269±0.111	1.70
11	0.29	-0.186±0.081	1.50

Table 5.6 CH_3Cl electron impact ionisation asymmetry results for different hexapole voltages.

There are two opposing influences on the variation of asymmetry effect with hexapole voltage. At lower voltages the degree of upper Stark state transmission is small. *D*-values (eqns. 5.5 and 5.6) which are used in the calculation of G and R (eqns. 5.8 and 5.7, respectively) become small and the deviations of G and R large, rendering the asymmetry results insignificant. The standard deviations in Table 5.6 quite obviously increase with decreasing hexapole voltage.

From an understanding of the hexapole state-selection technique (§2.4) it is known that lower hexapole voltages result in transmission of molecules which are progressively closer to being perfectly oriented. This is because the radial force exerted on the molecule is inversely proportional to the angle, θ, made between the dipole and electric field (eqn. 2.22). The calculated average orientation $\langle\rho\rangle_{calc}$ is listed for each hexapole voltage at which the asymmetry effect is reported (Table 5.6).

Following previous arguments the mean asymmetry effect should increase with decreasing hexapole voltage because of the improved degree of orientation. Results listed here are inconclusive, perhaps due to the errors associated with measurements at lower hexapole voltages. A second reason for the failure to observe the expected trend is simply the small change in $\langle\rho\rangle_{calc}$. Between 6 and 12 kV there is a shift in average orientation of just four degrees. It is the authors belief that variation of the asymmetry effect with hexapole voltage will only be observed for low voltages, where the change

in degree of orientation is substantial. Further investigation is required at low voltages, with attention to reducing the errors associated with D-value determination. Unfortunately, signal levels decrease rapidly towards low voltages and the signal-to-noise ratio falls below useable values. This may well preclude such measurements.

5.5 Reliability

The experimental apparatus used for this work has been subject to a number of tests designed to rule out the possibility that the observed asymmetry effects with respect to electron impact ionisation result from an experimental artefact. Some of these tests are discussed in previous sections but are included here for completeness.

5.5.1 Homogeneous field plate power supplies

The homogeneous field plate pulsing unit (HFPPU) contains both positive and negative pulsing supplies. For the results in §5.4 a positive supply is used, primarily because the fluctuation in measured ion signal is lower. To be confident in the HFPPU use of a negative supply must give asymmetry effects consistent with those reported for a positive supply.

Measurements of CH_3Cl (total ion count) asymmetry effects at 200 eV (hexapole ±5.5 kV, r_o = 5.88 mm) give the averages

$$G = -0.101 \pm 0.081 \qquad R = 1.23,$$

with a positive supply. Under the same conditions, but using a negative supply, the average asymmetry effect values are

$$G = -0.086 \pm 0.108 \qquad R = 1.21.$$

While the standard deviation is higher for the negative supply results the mean is still *negative* and lies well within one standard deviation of the positive supply mean.

To further prove the reliability of the HFPPU field reversal is carried out not by swapping which plate the supply is connected to but by using a supply of opposite polarity connected to the *same* plate. Two asymmetry measurements made in this way for CH_3Cl at 200 eV (hexapole ±5.5 kV) give

$$G = -0.071 \pm 0.030 \qquad R = 1.15.$$

Again, the asymmetry effect is negative and well within one standard deviation of results collected using a positive supply only. The HFPPU is therefore assumed to be reliable in operation and not responsible for any possible artefact.

5.5.2 Orienting field

Other studies find that where state-selected molecules are not exposed to an orienting field upon leaving the hexapole, any asymmetry effect disappears [Stolte, 1982; Böwering, 1994]. To carry out this test, while still pulsing the orienting field, the value of $delay_1$ is adjusted such that the field is switched off prior to the arrival of state-selected molecules in the homogeneous field region. The flight time of CH_3Cl in the field region is 0.3 ms so $delay_1$ is set to 2.5 ms while the first ions are measured after 3.5 ms. Only one result meets the selection criteria outlined in §5.3,

$$G = -0.004 \qquad R = 1.01.$$

Further measurements of this type are desirable, however, it is the authors opinion that this test successfully demonstrates that an orienting field is established by the HFPPU and that this field is switched off by the unit after a time, $delay_1$.

The asymmetry effect for electron impact ionisation of spherical species should be zero ($G = 0$ and $R = 1$). For the analysis here (§5.3) there must be some enhancement of signal level when the hexapole is turned on otherwise D-values (eqns. 5.5 and 5.6) are small and any asymmetry effect is rendered meaningless. Nevertheless where absolute signal levels are high D-values can and do rise above the minimum specified in §5.3. Results of asymmetry measurements for Ar and SF_6 are shown in Table 5.2. In the case of SF_6 D-values are ~-20 for δ signals of ~500. The G and R values of ~0 and ~1, respectively, are assigned.

5.5.3 Fragmentation

As noted in §5.4.3 perhaps the strongest evidence for ruling out an experimental artefact is the change in asymmetry effect when fragment ions are detected. Under the same experimental conditions, a G-factor for CH_3Cl^+ of -0.476±0.117 becomes 0.017±0.033 when CH_3^+ fragment ion signal is monitored. To a lesser extent (because of noise) the same occurs for CH_3Br.

The relative magnitude of the steric effects listed above are consistent with the mass spectral distribution of CH_3Cl and the steric effect measured with the mass insensitive detector. At 70 eV the fragment ion CH_3^+ ion is formed at 30% of the intensity observed for CH_3Cl^+. R-values are 2.80 and 0.96 for CH_3Cl^+ and CH_3^+, respectively. Weighting these appropriately, an average R-value of 1.54 is obtained. This compares favourably with the value of 1.23 measured with the mass insensitive detector.

The author believes that this combination of results cannot arise from any other source other than an asymmetry toward electron impact ionisation for the molecular ions CH_3Cl^+ and CH_3Br^+ but not for fragment ions CH_3^+. The differing collection efficiencies for either molecular or fragment ions when the field is switched to ~+0.1 V cm^{-1} or ~-0.1 V cm^{-1} are taken account of by the correction term, F (eqn. 5.2). In fact, for both molecular and fragment ions of CH_3Cl the average correction value is $F = 0.942$. This indicates that the trajectories of recoiling fragment and beam directed molecular ions are similar for a given residual field polarity.

Improved signal levels are always desirable but particularly so for these measurements. The reliability of results listed in Tables 5.2 and 5.4-5.6 are subject only to the accuracy with which they are determined. After considering the tests described in this section the reader should be confident that asymmetry toward electron impact ionisation exists and is quantifiable. Additional measurements suggested in each of the sections §5.4.1-5.4.4 are required for further understanding of the asymmetry effect.

5.6 Model

It has been stated in §1 and §2.6 that no simple predictive model exists describing all aspects of electron impact ionisation: threshold behaviour, cross-section energy dependence and fine structure, and fragmentation patterns (mass spectra). Results reported in §5.4 add to the understanding of alkali metal-alkyl halide electron transfer reactions and electron impact ionisation processes. A simple semi-empirical model that qualitatively reproduces the asymmetry effect and literature values of maximum (70 eV) ionisation cross-sections is described here [Brooks and Harland, 1995].

The approach of an electron toward a molecule establishes an electric field which is described by a Coulomb potential, ϕ_c. Where the Coulomb potential equals the electron

transition energy, or ionisation potential, E_o, the orbital electron involved in that transition absorbs from the field with an efficiency equal to the transition probability, P_i.

A cross-section, σ_c, is calculated from the electron-molecule separation where $\phi_c = E_o$. To find the maximum ionisation cross-section, σ_i, σ_c must be multiplied by the transition probability, P_i,

$$\sigma_i = \sigma_c P_i \tag{5.9}$$

The molecule is considered as a particle of point charge, q', determined by the dipole moment of the molecule *and* its orientation with respect to the approaching electron which in turn carries a point charge, q. Where the molecule is non-polar, $q' = 0$, however if the molecule has a permanent dipole moment, μ, and a separation of charge centres, l, then $q = \pm\mu/l$, depending on the dipole-electron orientation. Both cases assume that an induced dipole from the electron charge-molecular polarisability interaction is insignificant. In later comparison to experimental ionisation cross-sections the model is adjusted to incorporate molecular polarisability. The dipole length, l, for symmetric top molecules CY_3X is taken as the distance along the C-X axis between the centre of atom X and a Y atom plane perpendicular to the C-X axis.

For the three extreme spatial orientations the Coulomb potential is

- approach toward the positive-end of the dipole, $q' = +\mu/l$,

$$\phi_{c,\delta+} = \frac{q_{eff}}{4\pi\varepsilon_o r} = \frac{q + \mu / l}{4\pi\varepsilon_o r}; \tag{5.10}$$

- approach toward the negative-end of the dipole, $q' = -\mu/l$,

$$\phi_{c,\delta-} = \frac{q_{eff}}{4\pi\varepsilon_o r} = \frac{q - \mu / l}{4\pi\varepsilon_o r}; \text{ and} \tag{5.11}$$

- broadside approach, $q' = 0$,

$$\phi_{c,o} = \frac{q_{eff}}{4\pi\varepsilon_o r} = \frac{q}{4\pi\varepsilon_o r}. \tag{5.12}$$

At a given separation, r, it is obvious that the Coulomb potential will be the largest when the electron approaches the positive-end of the molecule, and in terms of the ionisation potential, E_o, will result in the largest cross-section, σ_c. Figure 5.4 is a plot of eqns. 5.10-5.12 for CH_3Cl, illustrating the differing separations at ionisation potential, E_o. For most cross-sections a maximum *impact parameter* is defined,

$$b_{max} = r, \text{ when } \phi_c = E_o, \tag{5.13}$$

and the cross-section is determined,

$$\sigma_c = \pi b_{max}^2 = \pi\left(\frac{q_{eff}}{4\pi\varepsilon_o}\right)^2, \tag{5.14}$$

or in units of square angstroms,

$$\sigma_c = 651.3\left(\frac{z_{eff}}{E_o}\right)^2, \tag{5.15}$$

where $z_{eff} = q_{eff} / q$, and substitutions for the appropriate quantities are made.

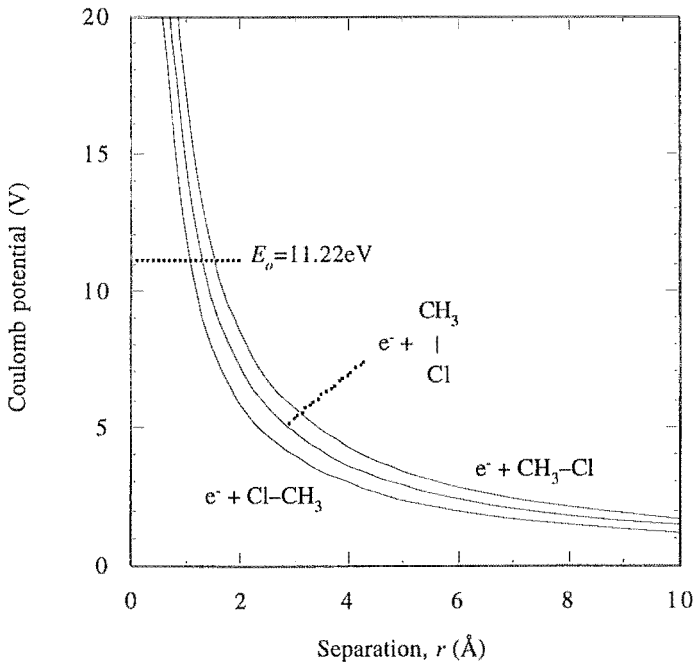

Figure 5.4 Coulomb potentials.

Using CH_3Cl as an example, the dipole moment is 1.87 Debye (6.24×10^{-30} C m) and effective dipole length, l, is 215 pm giving a value of $q' = \pm 2.90 \times 10^{-20}$ C or $\pm 0.18q$ where q is the electron charge. For the three extreme orientations, positive-end, negative-end and broadside approach, the cross-sections are calculated from eqn. 5.15 to be $\sigma_{c,\delta+} = 7.2$, $\sigma_{c,\delta-} = 3.5$ and $\sigma_{c,o} = 5.2$ Å^2, respectively. The positive and negative-end cross-sections give an asymmetry effect ratio of $R = \sigma_{c,\delta+} / \sigma_{c,\delta-} = 2.1$ which is similar in magnitude to the experimentally determined value of 2.80 for CH_3Cl^+ (Table 5.2). Of course, this simple model does not take into account the effect of electron energy on measured cross-sections. The maximum cross-section depends on the transition probability, P_i, which will be both energy and orientation dependent.

Table 5.7 summarises the calculated asymmetry ratios using eqn. 5.14 and comparison is made with experimental results from §5.4. Of those systems studied, CH_3Cl is predicted to have the largest steric effect, and this agrees with the findings in §5.4.

Molecule	μ (10^{-30} C m)	l (pm)	R_{calc}	R_{expt}
CH_3Cl	6.24	215	2.1	2.8
CH_3Br	6.04	230	1.9	-
CH_3I	5.40	251	1.7	-
CCl_3H	3.37	168	1.6	1.4
CBr_3H	3.30	175	1.6	-
CF_3Cl	1.67	220	1.2	-
CF_3Br	2.17	240	1.3	1.8
HCl	3.60	129	1.8	-
NO	0.62	136	1.1	-
CO	0.39	121	1.1	-

Table 5.7 Calculated and experimental asymmetry ratios, R.

Experimentally determined ionisation cross-sections at 70 eV, $\sigma_{i,r}$, are the result of electron-randomly oriented molecule interactions. A comparison between this model (eqn. 5.15) and experiment can be made, however, assuming that $\sigma_{i,r} \approx \sigma_{c,o}$ with $P_i = 1$, because in the region where $\phi = E_o$ the change in potential with separation for all dipole orientations is approximately constant. Figure 5.5 illustrates the correlation of $\sigma_{i,r}$ (experimental) and $\sigma_{c,o}$. Assuming the accuracy of the empirical data used in the correlation then any differences arise from the variation of P_i at 70 eV for each molecule or atom.

The transition probability, P_i, is proportional to $|\mu_{if}|^2$ where μ_{if} is the orbital overlap integral for the transition from state i (neutral) to state f (ionic),

$$\mu_{if} = \int \Psi_i^* \mu \Psi_f d\tau, \tag{5.16}$$

where μ is the electric dipole moment operator. $|\mu_{if}|^2$ in turn is related to molecular polarisability, α, [Atkins, 1994] by

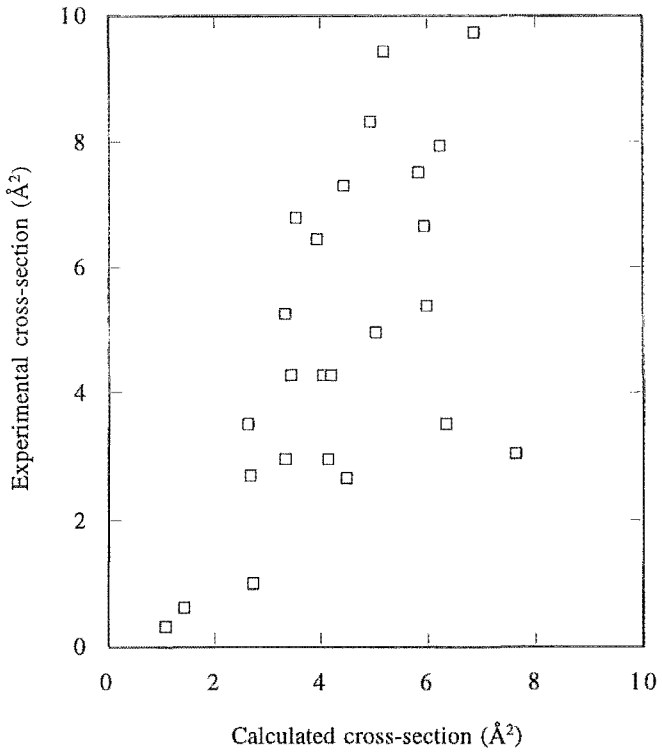

Figure 5.5 Correlation between experimental and calculated cross-sections.

$$\alpha = \frac{2}{3}\sum_f \frac{|\mu_{if}|^2}{E_f - E_i}. \tag{5.17}$$

Assuming that E_f - $E_i = E_o$ then

$$P_i \approx |\mu_{if}|^2 \approx \frac{3\alpha E_o}{2} = c\alpha' E_o, \tag{5.18}$$

and

$$\sigma_i = \sigma_c P_i \approx c\sigma_c \alpha' E_o, \tag{5.19}$$

where c is a constant and $\alpha' = \alpha / 4\pi\varepsilon_o$ the polarisability volume. Substituting eqn. 5.15 for σ_c gives

$$\sigma_i = c' z_{eff}^2 \alpha' / E_o \tag{5.20}$$

where c' is a constant. This model predicts the dependence of ionisation cross-section on polarisability first observed by Lampe, *et al.* [Lampe, 1957]. Figures 5.6 and 5.7 are plots of experimental cross-section against both α' and α' / E_o where it is assumed that z_{eff} is unity. The linear least squares fits for Figures 5.6 and 5.7 are

$$\sigma_i = 1.891\alpha' - 0.306, \text{ and} \tag{5.21}$$

$$\sigma_i = 17.58\alpha' / E_o + 0.851, \text{ respectively.} \tag{5.22}$$

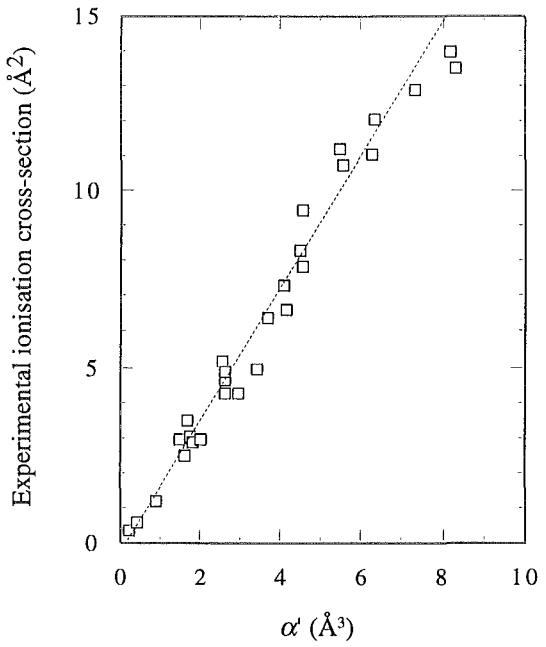

Figure 5.6 Experimental ionisation cross-sections plotted against α'.

Molecule	σ_c (Å²) (eqn. 5.15)	σ_i (Å²) (eqn. 5.21)	σ_i (Å²) (eqn. 5.22)	σ_i (Å²) (experimental)
Ar	2.62	2.92	2.61	3.52
N_2	2.68	3.14	2.76	2.88
CH_4	4.16	4.75	4.53	4.65
CH_3Cl	5.17	8.34	8.06	9.44

Table 5.8 Calculated and experimental ionisation cross-sections.

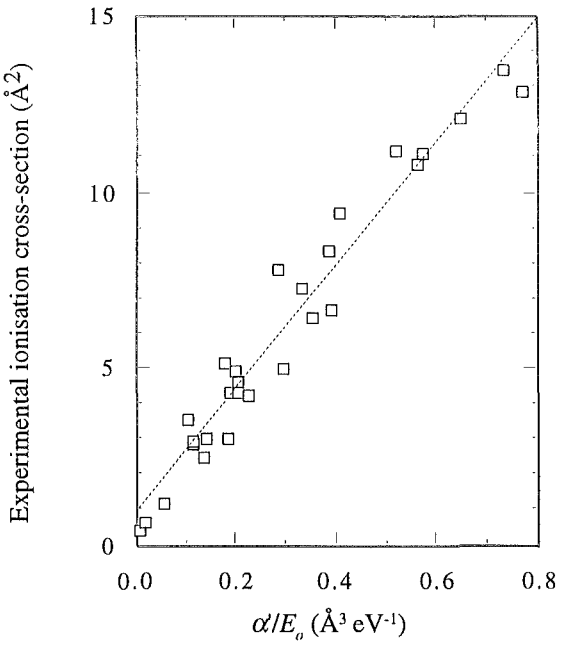

Figure 5.7 Experimental ionisation cross-sections plotted against α' / E_o.

Table 5.8 makes comparison between eqns. 5.15, 5.21, 5.22 and experimental 70 eV ionisation cross-sections for several species. Allowing for the models simplicity and estimated experimental errors, a good correlation is observed over a 20-fold variation in experimental ionisation cross-sections.

Chapter 6

Conclusions and Future Work

The upper Stark state relaxation cross-sections for molecular beams of CH_3Cl and for beams of 20% CCl_3H seeded in Ar have been measured for a range of polar and non-polar quencher species. These cross-sections represent the first ever measurement of symmetric top upper Stark state relaxation cross-sections. In the case of CH_3Cl, these range between 190 $Å^2$ for a He quencher and 443 $Å^2$ for quenching by CH_3Cl. The variation of the cross-section values with quencher species can be explained by the strength of the long range van der Waals interaction potential between colliding species.

For the CH_3Cl-CH_3Cl beam-quencher combination an increase in quencher pressure from 10^{-7} to 10^{-6} torr results in a beam attenuation of ~20%. The upper Stark states that are preferentially defocused from the beam are those oriented more closely about the electric field axis (§4.3.2). The success of an orientation study could therefore be affected significantly by a pressure increase of this magnitude. It is conceivable that this situation could arise - poor separation of the nozzle and filter chambers would result in a significant background of beam molecules within the filter. Careful planning of orientation studies is necessary to avoid this situation.

Further investigate of the CCl_3H molecule, for which preliminary results are reported, and other condensable species is underway. This requires significant modification of the molecular beam apparatus, including the installation of a new piezoelectric supersonic nozzle and removal of liquid nitrogen traps in the scattering cell region. Diffusion pumps are to be replaced with turbomolecular pumps, preventing contamination of the vacuum system by backstreaming oil.

The calculation of van der Waals interaction potential terms requires a knowledge of molecular beam velocity, and translational and rotational temperatures of both quencher and beam species. At present these values are calculated. A new supersonic nozzle with very short opening time will facilitate the measurement of beam velocity distributions and translational temperatures. Seeding of symmetric top molecules in inert gas carriers in conjunction with this nozzle will also allow further investigation of the velocity dependence of relaxation cross-sections. The experimental determination of rotational temperature, however, is beyond the current resources of this research programme, requiring a laser-based spectroscopic technique.

State-specific upper Stark state relaxation cross-sections have been measured for CH_3X (X = F, Cl and Br) species with an Ar quencher. In the case of CH_3Cl, cross-sections are also measured for N_2 as the quencher. Assignment of the cross-sections to individual $|JKM\rangle$ rotational states or a small range of $|JKM\rangle$ rotational states is facilitated by the simulation of hexapole filter upper Stark state transmission characteristics. Cross-sections for the quenching of the $|111\rangle$ rotational states of CH_3X, X = F, Cl and Br species by Ar are 125, 170 and 185 $Å^2$, respectively. The $|111\rangle$ rotational state relaxation cross-section for CH_3Cl and an N_2 quencher is 215 $Å^2$.

At present the hexapole filter is being lengthened by 0.5 m to improve its' state resolving power. This will enable single state relaxation cross-sections to be

determined for higher J rotational states with greater accuracy, e.g. the $|222\rangle$ state. A number of symmetric top molecules will be investigated including the oblate top CF_3H.

Elastic/inelastic collision cross-sections for CH_3Cl and a range of non-polar quencher species have been measured. These are a byproduct of the method for determining relaxation cross-sections. The variation of the elastic/inelastic cross-sections with quencher species correlates with the change in calculated van der Waals interaction potential strength. Lengthening the hexapole as described above and increasing the distance between the hexapole exit aperture and the detector will improve angular resolution of the scattering cell, facilitating the measurement of accurate total elastic/inelastic collision cross-sections for heavy beam and quencher species, e.g. CCl_3H.

Experiments in §5 have demonstrated, for the first time, that the efficiency and outcome of electron impact ionisation is influenced by molecular orientation. The ionisation efficiency is lowest for electron impact on the negative end of the dipole. This is found for the molecules CH_3Cl and CCl_3H. Preliminary results for CH_3Br and CF_3Br suggest this also. In addition, the mass spectrum is orientation dependent, for example, in the ionisation of CH_3Cl the ratio CH_3Cl^+:CH_3^+ depends on molecular orientation.

The variation of electron impact ionisation asymmetry for CH_3Cl with electron energy and hexapole voltage has also been investigated. There is a small increase in the asymmetry effect with electron energy which suggests that a new electron source spanning a wide range of electron energies would be desirable. The design of such a source is currently being evaluated. There is no significant variation of asymmetry effect for the range of hexapole voltages studied. Investigation at lower voltages, where the effect is *predicted* to increase, is unlikely to succeed because of the low upper Stark state transmission intensities at these voltages.

In the future the asymmetry effect of ion-oriented molecule reactions will be studied. Alkali metal ion emission sources have been constructed for this purpose.

References

Anderson, 1974	Anderson, J. B. *Molecular Beams and Low Density Gas Dynamics* Dekker (1974).
Altkorn, 1985	Altkorn, R. and Zare, R. Z. *Mol. Phys.* **55** (1985) 1.
Atkins, 1994	Atkins, P. W. *Physical Chemistry* (5th edition) Oxford University Press (1994).
Beenakker, 1962	Beenakker, J. J. M., Scoles, G., Knaap, H. F. P. and Jonkman, R. M. *Phys. Lett.* **2** (1962) 5.
Bennewitz, 1955	Bennewitz, H. G., Paul, W. and Schlier, Ch. *Z. Phys.* **141** (1955) 6.
Bennewitz, 1964	Bennewitz, H. G., Kramer, K. H., Paul, W. and Toennies, J. P. *Z. Phys.* **177** (1964) 84.
Böwering, 1994	Böwering, N., Volkmer, M., Meier, C., Lieschke, J. and Fink, M. *Z. Phys. D* **30** (1994) 177.
Brauner, 1989	Brauner, M., Briggs, J. S. and Klar, H. *J. Phys. B* **22** (1989) 2265.
Brooks, 1976	Brooks, P. R. *Science* **193** (1976) 11.
Brooks, 1995	Brooks, P. R. and Harland, P. W. in *Advances in Gas Phase Ion Chemistry* ed. Adams, N. G. and Babcock, L. M. **2** JAI Press, Inc. (1995).
Cameron, 1991	Cameron, B. R. and Harland, P. W. *J. Chem. Soc. Faraday Trans.* **87** (1991) 1069.
Cameron, 1993	Cameron, B. R. and Harland, P. W. *J. Chem. Soc. Faraday Trans.* **89** (1993) 3517.
Cameron, 1993b	Cameron, B. R. and Harland, P. W. *J. Chem. Soc. Faraday Trans.* **89** (1993) 1903.
Cameron, 1994	Cameron, B. R. and Harland, P. W. *Rev. Sci. Instrum.* **65** (1994) 108.
Choi, 1986	Choi, S. E. and Bernstein, R. B. *J. Chem. Phys.* **85** (1986) 150.
Drullinger, 1969	Drullinger, R. E. and Zare, R. N. *J. Chem. Phys.* **51** (1969) 5532.
Drullinger, 1973	Drullinger, R. E. and Zare, R. N. *J. Chem. Phys.* **59** (1973) 4225.
Ehrhardt, 1986	Ehrhardt, H., Jung, K., Knoth, G. and Schlemmer, P. *Z. Phys. D* **1** (1986) 3.
Estler, 1978	Estler, R. C. and Zare, R. N. *J. Am. Chem. Soc.* **100** (1978) 1323.

Friedrich, 1991 Friedrich, B., Pullman, D. P. and Herschbach, D. R. *J. Phys. Chem.* **95** (1991) 8118.

Friedrich, 1991b Friedrich, B. and Herschbach, D. R. *Z. Phys. D* **18** (1991) 153.

Goldstein, 1950 Goldstein, H. *Classical Mechanics* Addison-Wesley Publishing Company, Inc. (1950).

Hagstrum, 1953 Hagstrum, H. D. *Natl. Bur. Standards Circ. No.* **522** (1953) 193.

Harland, 1992 Harland, P. W., Carman Jr., H. S., Phillips, L. F. and Brooks, P. R. *J. Chem. Phys.* **96** (1992) 1557.

Hoffmeister, 1987 Hoffmeister, M., Schleysing, R. and Loesch, H.-J. *J. Phys. Chem.* **91** (1987) 5441.

Kaesdorf, 1985 Kaesdorf, S., Schönhense, G. and Heinzmann, U. *Phys. Rev. Lett.* **54** (1985) 885.

Karny, 1978 Karny, Z., Estler, R. C. and Zare, R. N. *J. Chem. Phys.* **69** (1978) 5199.

Kasai, 1993 Kasai, T., Matsunami, T., Fukawa, T., Ohoyama, H. and Kuwata, K. *Phys. Rev. Lett.* **70** (1993) 3864.

Kurz, 1979 Kurz, E. A. *American Laboratory* (1979).

Lampe, 1957 Lampe, F. W., Franklin, J. L. and Field, F. H. *J. Am. Chem. Soc.* **79** (1957) 6129.

Landau, 1959 Landau, L. D. and Lifshitz, E. M. *Quantum Mechanics* Pergamon Press (1959).

Loesch, 1990 Loesch, H.-J. and Remscheid, A. *J. Chem. Phys.* **93** (1990) 4779.

Loesch, 1991 Loesch, H.-J. and Remscheid, A. *J. Phys. Chem.* **95** (1991) 8194.

Loesch, 1992 Loesch, H.-J. and Möller, J. *J. Chem. Phys.* **97** (1992) 9016.

Loesch, 1993 Loesch, H.-J. and Möller, J. *J. Phys. Chem.* **97** (1993) 2158.

Loesch, 1993b Loesch, H.-J. and Stienkemeier, F. *J. Chem. Phys.* **98** (1993) 9570.

Loesch, 1994 Loesch, H.-J. and Stienkemeier, F. *J. Chem. Phys.* **100** (1994) 740.

Maltz, 1972 Maltz, C., Weistein, N. D. and Herschbach, D. R. *Mol. Phys.* **24** (1972) 133.

Marcelin, 1975 Marcelin, G. and Brooks, P. R. *J. Am. Chem. Soc.* **97** (1975) 1710.

Massey, 1934 Massey, H. S. W., and Mohr, C. B. O. *Proc. R. Soc.* **A144** (1934) 188.

Massey, 1969 Massey, H. S. W., Burhop, E. H. S. and Gilbody, H. B. *Electronic and Ion Impact Phenomena* **2-3** Oxford University Press (1971).

Maxwell, 1867 Maxwell, J. C. *Phil. Trans. Royal Soc.* **157** (1867) 49.

Meier, 1994 — Meier, C., Volkmer, M., Lieschke, J., Fink, M. and Böwering, N. *Z. Phys. D* **30** (1994) 183.

Ohoyama, 1993 — Ohoyama, H., Iguro, T., Kasai, T. and Kuwata, K. *Chem. Phys. Lett.* **209** (1993) 361.

Otvos, 1956 — Otvos, J. W. and Stevenson, D. P. *J. Am. Chem. Soc.* **78** (1956) 546.

Parker, 1981 — Parker, D. H., Chakravorty, K. K. and Bernstein, R. B. *J. Phys. Chem.* **85** (1981) 466.

Pauly, 1968 — Pauly, H. and Toennies, J. P. *Methods of Experimental Physics* **7A** Academic Press (1968).

Phillips, 1995 — Phillips, L. F. *J. Chem. Soc. Faraday Trans.* In press (1995).

Pullman, 1990 — Pullman, D. P., Friedrich, B. and Herschbach, D. R. *J. Chem. Phys.* **93** (1990) 3224.

Dean, 1951 — Dean, R. B. and Dixon, W. J. *Anal. Chem.* **23** (1951) 636.

Rothe, 1959 — Rothe, E. W. and Bernstein, R. B. *J. Chem. Phys.* **31** (1959) 1619.

Scoles, 1988 — Scoles, G. (ed) *Atomic and Molecular Beam Methods* **1** Oxford University Press, Inc. (1988).

Senftleben, 1930 — Senftleben, H. *Physik. Z* **31** (1930) 961.

Shirley, 1963 — Shirley, J. H. *J. Chem. Phys.* **38** (1963) 2896.

Sinha, 1974 — Sinha, M. P., Caldwell, C. D. and Zare, R. N. *J. Chem. Phys.* **61** (1974) 491.

Srivastava, 1988 — Srivastava, M. K. and Sharma, S. *Phys. Rev. A* **37** (1988) 628.

Stolte, 1982 — Stolte, S. *Ber. Bunsenges. Phys. Chem.* **86** (1982) 413.

Toennies, 1962 — Toennies, J. P. *Faraday Discuss. Chem. Soc.* **33** (1962) 96.

Townes, 1955 — Townes, C. H. and Schawlow, A. L. *Microwave Spectroscopy* McGraw-Hill Book Company, Inc. (1955).

Volkmer, 1992 — Volkmer, M., Meier, Ch., Mihill, A., Fink, M. and Böwering, N. *Phys. Rev. Lett.* **68** (1992) 2289.

Walker, 1967 — Walker, S. and Straw, H. *Spectroscopy: Ultra-violet, Visible, Infra-red and Raman Spectroscopy* **2** Chapman and Hall Ltd. (1967).

Xing, 1994 — Xing, G., Kasai, T. and Brooks, P. R. *J. Am. Chem. Soc.* **116** (1994) 7421.

Zare, 1988 — Zare, R. N. *Angular Momentum* John Wiley & Sons, Inc. (1988).

Appendices

The computer instructions for machine interfacing are written in Microsoft QuickBASIC because of the languages' simplicity, facilitating further modification of routines by researchers not familiar with the peculiarities of command syntax.

A1 Stepping motor routines

```
TYPE FunTable                                   ' type declaration for Cmd838
  funNo           AS INTEGER                    ' subroutine; a record of this type
  channel         AS INTEGER                    ' contains the instructions for the
  bufferOff       AS INTEGER                    ' PCL-838 card
  bufferSeg       AS INTEGER
  vi              AS INTEGER
  vf              AS INTEGER
  time            AS LONG
  steps           AS LONG
  datus           AS INTEGER
  returnValue     AS LONG
END TYPE

  CONST xCH2 = &H2                              ' constant declarations
  CONST CMDxActive = 10                         ' for the Cmd838 subroutine
  CONST CMDxOutput = 30
  CONST CMDxInput = 31
  CONST CMDxDelay = 42
  CONST CMDxBase = 53
  CONST CMDxReset = 54
  CONST CMDxCwStep = 60
  CONST CMDxCcwStep = 61
  CONST CMDxStepSpd = 62
  CONST CMDxCwSpeed = 67
  CONST CMDxCcwSpeed = 68
  CONST CMDxBusy = 72
  CONST CMDxFirmware = 73

result = Cmd838(CMDxBase, 0, &H2E0)             ' set up the PCL-838 card to
result = Cmd838(CMDxReset, 0, 0)                ' accept instructions on channel 2
result = Cmd838(CMDxActive, xCH2, 0)
result = Cmd838(CMDxStepSpd, xCH2, 1000)

SUB stepsm (direction%)                         ' subroutine to simplify access to the
  IF direction% = 1 THEN                        ' stepping motor subroutine Cmd838
    result = Cmd838(CMDxCwStep, xCH2, 0)
  ELSE
    result = Cmd838(CMDxCcwStep, xCH2, 0)
  END IF
END SUB

FUNCTION Cmd838 (cmdNo AS INTEGER, channel AS INTEGER, datus AS INTEGER)
  DIM InRegs AS RegType                         ' subroutine that interfaces to the
  DIM Table  AS FunTable                        ' PCL-838 stepping motor card

  Table.funNo = cmdNo
```

```
  Table.channel = channel
  Table.datus = datus

  InRegs.ax = &HD202
  InRegs.bx = VARPTR(Table)
  InRegs.cx = VARSEG(Table)
  CALL INTERRUPT(&H2F, InRegs, InRegs)
  datus = Table.datus
  Cmd838 = InRegs.ax                          ' returns a 0 for no error, or
END FUNCTION                                  ' an error code
```

A2 Ionisation gauge controller latching routine

```
FUNCTION hexP! (temp%)
  port = &H1BC
  OUT port + 3, 191
  portA = INP(port)
  portB = INP(port + 1)
  theMSD = (NOT portA AND 240) / (2 ^ 4)
  theLSD = NOT portA AND 15
  theEXP = NOT portB AND 15
  theP! = (theMSD + (theLSD / 10)) * (10 ^ (theEXP * -1))
  hexP! = theP!
END FUNCTION
```

A3 DSA control routines

```
DIM sig(1024)                                 ' array for incoming DSA signal
                                              ' establish serial communication with DSA
OPEN "COM2: 19200,N,8,1,RB5000,OP3000" FOR RANDOM AS 1

CALL send("FPON")                             ' enable DSA front panel to be accessed
CALL rc(text$)                                ' by experimentalist
CALL SETUP(ver$)                              ' sets up DSA data transfer mode

INPUT "", NSAM%                               ' ask user for number of scans to be
SAM% = 0                                      ' acquired
CALL send("HOLD")                             ' set the DSA to hold
CALL rc(text$)

DO WHILE SAM% < NSAM%                         ' data acquisition loop
  CALL send("SINGL")                          ' instruct the DSA to perform a single
  CALL rc(text$)                              ' scan

  DO WHILE text$ <> "H"                       ' query DSA until scan is finished
    CALL send("BUSY?")
    CALL rc(text$)
  LOOP

  SAM% = SAM% + 1
  CALL send("MEM?,TRA")                       ' instruct the DSA to transfer scan
  CALL rc(sigc$)

  FOR x = 1 TO 1024                           ' transfer ASCII data to numeric array
    sig(x) = sig(x) + ASC(MID$(sigc$, x, 1))
  NEXT x
LOOP

SUB rc (text$)                                ' subroutine to receive information
  text$ = ""                                  ' from the DSA
  LINE INPUT #1, text$
```

```
  IF RIGHT$(text$, 3) <> (" OK") THEN text$ = "": EXIT SUB
  text$ = LEFT$(text$, LEN(text$) - 3)
END SUB

SUB send (chars$)                              ' subroutine to send information to
  PRINT #1, chars$                             ' the DSA
END SUB

SUB SETUP (ver$)                               ' queries DSA for EPROM verson and
  CALL send("IDENT")                           ' sets DSA up to transfer data in
  CALL rc(ver$)                                ' binary mode
  CALL send("MODE,BIN")
  CALL rc(text$)
END SUB
```

A4 Pulse counting latching routines

```
port = &H1A0                                   ' specify PCL-8255/8253 card location
DIM CO(100), C2(100)
INPUT ""; TT: INPUT ""; NL                     ' get length of each count and number
FOR LO = 1 TO NL                               ' of cycles
  countD = 65535
                                               ' initialise counters
  OUT port + &H3, &H80: OUT port + &H0, &H0
  OUT port + &H1, &H0: OUT port + &H2, &H0
  OUT port + &HB, &H34: OUT port + &H8, &H0
  OUT port + &H8, &H0: OUT port + &HB, &H74
  OUT port + &H9, &H0: OUT port + &H9, &H0
  OUT port + &HB, &HB4: OUT port + &HA, &HFF
  OUT port + &HA, &HFF: OUT port + &H2, &H1
  OUT port + &H2, &H5: OUT port + &H2, &H1
  OUT port + &H2, &H5: OUT port + &H2, &H1
  OUT port + &H2, &H3
  lastC = countD
  T = TIMER
  DO WHILE TIMER < T + TT                      ' continuously latch counters
    OUT port + &HB, &H0: cal = INP(port + &H8)
    cah = INP(port + &H8): OUT port + &HB, &H40
    cbl = INP(port + &H9): cbh = INP(port + &H9)
    OUT port + &HB, &H80: ccl = INP(port + &HA)
    cch = INP(port + &HA)
    IF cch > lastC THEN countD = countD - 1
    lastC = cch
  LOOP                                         ' convert counter values to counts
  CO(LO) = (2 ^ 32 - 1) - ((cah * 256 + cal) + 65536 * (cbh * 256 + cbl))
  C2(LO) = (2 ^ 32 - 1) - ((cch * 256 + ccl) + 65536 * countD)
NEXT LO

                                               ' determine averages
CT = 0: BT = 0: df = 0: CTSD = 0: BTSD = 0: DFSD = 0
FOR LO = 1 TO NL
  CT = CT + CO(LO)
  BT = BT + C2(LO)
NEXT LO
CT = CT / NL: BT = BT / NL
                                               ' determine standard deviations
FOR LO = 1 TO NL
  CTSD = CTSD + ABS(CT - CO(LO))
  BTSD = BTSD + ABS(BT - C2(LO))
  DFSD = DFSD + ABS((CT - BT) - (CO(LO) - C2(LO)))
NEXT LO
CTSD = CTSD / NL: BTSD = BTSD / NL: DFSD = DFSD / NL
```

A5 Electrometer and MKS Baratron latching routines

```
SUB getE (curr)                              ' electrometer interface routine
  port = &H170                               ' location on ADDA-14 card to which the
  VOUT = 8.5                                 ' electrometer output is connected
  channel = 1
  RT% = 50
  numLoop = 5
  curr = 0
  FOR x = 1 TO numLoop                       ' take five measurements
    TOTAL = 0
    FOR C% = 1 TO RT%
      OUT port + 1, 0
      OUT port + 0, channel
      FOR I% = 1 TO 8: A = INP(port + 8): NEXT I%
      FOR I% = 1 TO 8: A = INP(port + 12): NEXT I%
      H6 = INP(port + 3)
      L8 = INP(port + 2)
      value = (H6 - 64 * (INT(H6 / 64))) * 256 + L8 - 8192
      TOTAL = TOTAL + value
    NEXT C%
    MEAN = (TOTAL / RT%)
    curr = curr + MEAN
  NEXT x
  curr = curr / numLoop                      ' determine the average value and
                                             ' scale using a predetermined slope and
                                             ' intercept
  curr = ((curr - .0187353) / .910905) / 1000
END SUB

SUB getP (torr)                              ' MKS Baratron interface routine
  port = &H170                               ' location on ADDA-14 card to which the
  VOUT = 8.5                                 ' MKS Baratron output is connected
  channel = 0
  RT% = 50
  numLoop = 5
  torr = 0
  FOR x = 1 TO numLoop                       ' take five measurements
    TOTAL = 0
    FOR C% = 1 TO RT%
      OUT port + 1, 0
      OUT port + 0, channel
      FOR I% = 1 TO 8: A = INP(port + 8): NEXT I%
      FOR I% = 1 TO 8: A = INP(port + 12): NEXT I%
      H6 = INP(port + 3)
      L8 = INP(port + 2)
      value = (H6 - 64 * (INT(H6 / 64))) * 256 + L8 - 8192
      TOTAL = TOTAL + value
    NEXT C%
    MEAN = (TOTAL / RT%)
    VOLTS = (MEAN / 8192) * VOUT
    PTORR = VOLTS * 1000
    torr = torr + PTORR                      ' determine average value and scale
  NEXT x                                     ' using a predetermined slope and
                                             ' intercept
  torr = ((torr / numLoop) - 18.3677) / .956102
END SUB
```

A6 Leak valve - ionisation gauge negative feedback routine

```
' stepping motor interface declarations and routines are defined in A1
' ionisation gauge controller latching routine is defined in A2

CONST lPress! = 1E-08                          ' limiting values for safety check
CONST hPress! = .00005

result = Cmd838(CMDxBase, 0, &H2E0)            ' set up the PCL-838 card to
result = Cmd838(CMDxReset, 0, 0)               ' accept instructions on channel 2
result = Cmd838(CMDxActive, xCH2, 0)

temp% = setP%(pVal!)                           ' this instruction is executed
                                               ' during pulse counting measurements
FUNCTION setP% (pVal!)                         ' pVal! is the desired pressure
  stepAdj% = 0
  pExp% = INT(LOG(pVal!) / LOG(10))            ' determine exponent of pVal!

                                               ' adjust leak valve until pressure is
                                               ' within 0.1 of the exponent of the
                                               ' desired pressure
  DO UNTIL ABS(hexP!(1) - pVal!) < (10 ^ (pExp% - 1))
    IF hexP!(1) < pVal! THEN sdir% = 1 ELSE sdir% = -1
    CALL stepsm(2 * sdir%)                     ' adjust leak valve is steps of 2
    stepAdj% = stepAdj% + (2 * sdir%)
    theP! = hexP!(1)                           ' remeasure pressure

    IF theP! < lPress! OR theP! > hPress! THEN
      PRINT "Pressure reading abnormal, please rectify...";
      A$ = INKEY$
      DO UNTIL A$ <> ""
        A$ = INKEY$
        FOR x = 440 TO 1300 STEP 30: SOUND x, 1: NEXT x
      LOOP                                     ' if fault isn't rectified then an
                                               ' error value is returned
      IF UCASE$(A$) = "A" THEN setP% = -32768: EXIT FUNCTION
      LOCATE 23, 3: COLOR 11: PRINT "Setting pressure now...";
      theP! = hexP!(1)                         ' remeasure pressure
    END IF
                                               ' this control structure slows down
                                               ' the addition or removal of quencher
                                               ' as the desired pressure is approached
    IF ABS(theP! - pVal!) < (pVal! / 3) THEN
      T = TIMER
      DO UNTIL TIMER > T + .8
      LOOP
    END IF
  LOOP
  setP% = stepAdj%                             ' return the number of leak valve steps
END FUNCTION
```

A7 Hexapole control routine

```
SUB sethv (voltage)
  value = INT((voltage / 30000) * 4095)        ' determine 12-bit equivalent
  PORT = &H1AC                                 ' location of PCL-8255 card
  OUT PORT + &H3, &H80                         ' set 8255 chip for output
  OUT PORT + &H0, &H0
  OUT PORT + &H1, &H0
  OUT PORT + &H2, &H0
  OUT PORT + 0, value MOD 256                  ' output the voltage
  OUT PORT + 1, INT(value / 256)
END SUB
```

A8 Attenuation experiment routines

The first set of instructions are for the measurement of beam attenuation at a fixed hexapole voltage. Following this are instructions for the measurement of beam attenuation at a range of hexapole voltages.

```
' stepping motor interface declarations and routines are defined in A1
' ionisation gauge controller latching routine is defined in A2
' pulse counting latching routines are defined in A4
' leak valve - ionisation gauge negative feedback routine is defined in A6
' hexapole control routine is defined in A7

CONST pSteps% = 200

result = Cmd838(CMDxBase, 0, &H2E0)          ' set up the PCL-838 card to
result = Cmd838(CMDxReset, 0, 0)             ' accept instructions on channel 2
result = Cmd838(CMDxActive, xCH2, 0)

                                             ' obtain parameters for experiment
PRINT "Run #                > "; : INPUT "", RN$
PRINT "Hexapole (V)         > "; : INPUT "", hex%
PRINT "Count time (s)       > "; : INPUT "", ctime%
PRINT "Number of scans      > "; : INPUT "", scans%
PRINT "Number of points     > "; : INPUT "", points%
PRINT "Pressure increment   > "; : INPUT "", pinc!
PRINT "Quencher ICS         > "; : INPUT "", qics!
CALL collect(RN$, hex%, ctime%, scans%, points%, pinc!, qics!)


SUB collect (RN$, hex%, ctime%, scans%, points%, pinc!, qics!)
  numSteps% = 0
  DIM P!(pSteps%), E!(pSteps%), sig1&(pSteps%), sig2&(pSteps%)
  P!(1) = hexP!(1)
  currP% = 0
  DO WHILE currP% < points%
    CALL sethv(0)                            ' hexapole off
    pVal! = 0: pVal! = P!(1) + currP% * pinc!
                                             ' set quencher pressure
    numSteps% = numSteps% + setP%(pVal!)
    currP% = currP% + 1

    T = TIMER                                ' allow pressure to stabilise
    DO UNTIL TIMER > T + 2
    LOOP

    P!(currP%) = hexP!(1)                    ' measure pressure
                                             ' measure beam intensity
    sig1&(currP%) = counter&(ctime%, scans%)

    CALL sethv(hex%)                         ' hexapole on
                                             ' measure beam intensity'
    sig2&(currP%) = counter&(ctime%, scans%)
  LOOP

  CALL sethv(0)                              ' turn off hexapole and close leak valve
  CALL stepsm(numSteps% * (-1))
END SUB
```

```
' stepping motor interface declarations and routines are defined in A1
' ionisation gauge controller latching routine is defined in A2
' pulse counting latching routines are defined in A4
' leak valve - ionisation gauge negative feedback routine is defined in A6
' hexapole control routine is defined in A7

CONST pSteps% = 200

result = Cmd838(CMDxBase, 0, &H2E0)          ' set up the PCL-838 card to
result = Cmd838(CMDxReset, 0, 0)             ' accept instructions on channel 2
result = Cmd838(CMDxActive, xCH2, 0)

                                             ' obtain parameters for experiment
PRINT "Run #                 > "; : INPUT "", RN$
PRINT "Start HV (V)          > "; : INPUT "", hexs%
PRINT "Finish HV (V)         > "; : INPUT "", hexf%
PRINT "# HV steps            > "; : INPUT "", hvsteps%
PRINT "Count time (s)        > "; : INPUT "", ctime%
PRINT "# Counting scans      > "; : INPUT "", scans%
PRINT "# Pressures           > "; : INPUT "", points%
PRINT "Pressure increment    > "; : INPUT "", pinc!
PRINT "Quencher ICS          > "; : INPUT "", qics!
CALL collect(RN$, hexs%, hexf%, hvsteps%, ctime%, scans%, points%, pinc!, qics!)


SUB collect (RN$, hexs%, hexf%, hvsteps%, ctime%, scans%, points%, pinc!, qics!)
  DIM p!(points%), sig&(points%, hvsteps% + 1)
  pNum% = 0
  hvNum% = 0
  hexInc% = INT((hexf% - hexs%) / hvsteps%)

  DO WHILE pNum% < points%                   ' loop for the number of required
                                             ' transmission curves
    pNum% = pNum% + 1
    pVal! = pinc! * pNum%
    temp% = setP%(pVal!)                     ' set quencher pressure
    IF temp% = -32768 THEN EXIT DO
    numSteps% = numSteps% + temp%

    T = TIMER                                ' wait for pressure to stabilise
    DO UNTIL TIMER > T + 2
    LOOP

    p!(pNum%) = hexP!(1)                     ' measure pressure
    FOR hvNum% = 0 TO hvsteps%               ' loop for the required voltages
      SELECT CASE hvNum%
        CASE 0
          CALL sethv(0)
        CASE hvsteps%
          CALL sethv(5000)
        CASE ELSE
          CALL sethv(hexs% + hvNum% * hexInc%)
      END SELECT
                                             ' measure beam intensity
      sig&(pNum%, hvNum%) = counter&(ctime%, scans%)
      temp% = setP%(p!(pNum%))               ' check pressure
      IF temp% = -32768 THEN EXIT DO
      numSteps% = numSteps% + temp%
    NEXT hvNum%
    CALL sethv(0)                            ' set hexapole off
                                             ' remeasure 0 kV signal for drift
                                             ' correction if necessary
    sig&(pNum%, hvsteps% + 1) = counter&(ctime%, scans%)
  LOOP

  CALL sethv(0)                              ' turn off hexapole and close leak valve
  IF temp% <> -32768 THEN CALL stepsm(numSteps% * (-1))
END SUB
```